Propulsion
New Perspectives and Applications

*Edited by Kazuo Matsuuchi
and Hiroaki Hasegawa*

Propulsion - New Perspectives and Applications

*Edited by Kazuo Matsuuchi
and Hiroaki Hasegawa*

IntechOpen

Supporting open minds since 2005

Notice
Statements and opinions expressed in the chapters are these of the individual contributors and not necessarily those of the editors or publisher. No responsibility is accepted for the accuracy of information contained in the published chapters. The publisher assumes no responsibility for any damage or injury to persons or property arising out of the use of any materials, instructions, methods or ideas contained in the book.

We are IntechOpen,
the world's leading publisher of
Open Access books
Built by scientists, for scientists

5,600+
Open access books available

137,000+
International authors and editors

170M+
Downloads

156
Countries delivered to

Our authors are among the
Top 1%
most cited scientists

12.2%
Contributors from top 500 universities

Interested in publishing with us?
Contact book.department@intechopen.com

Numbers displayed above are based on latest data collected.
For more information visit www.intechopen.com

Meet the editors

Dr. Kazuo Matsuuchi obtained his Ph.D. in Engineering from Osaka University, Japan, in 1976. In 1977, he served as a research assistant at the Institute of Structural Engineering, University of Tsukuba, Japan. He became a full professor at the same university in 1995. In 2012 he earned the title of Professor Emeritus and he is still active at the University of Tsukuba. Dr. Matsuuchi was a visiting professor at Khon Kaen University, Thailand, and a specially appointed professor at the Oguz Khan Engineering and Technology University of Turkmenistan.

In 1989, Dr. Hiroaki Hasegawa started as a research engineer working on research and development of ramjet and jet engines at the Japan Defense Agency. In 1998, he earned the title of senior research engineer at the same agency. He obtained a Ph.D. in Engineering from the University of Tsukuba, Japan, in 1999. Dr. Hasegawa was appointed a lecturer in the Department of Mechanical Engineering, Akita University, Japan, in 2002. He is currently a professor in the Department of Mechanical and Intelligent Engineering, Utsunomiya University, Japan.

Contents

Preface

Movement is a critical aspect in the lives of almost all creatures, including humans, birds, and insects. Plants that cannot move by themselves live with the help of movable living creatures. Without movement, creatures would not be able to sustain their species in the future. However, movement requires a certain type of force.

To move from one place to another, work must be performed by the action of a force, and typically, energy is consumed while performing the work.

First, we would like to describe the movement of human beings and materials. Originally, movement was only enabled by the legs and arms of humans; thus, the range of work or moving distance was not significantly large. As time passed, tools and devices for transportation were developed. In the early stages, small vehicles such as bicycles were developed; however, the origin of the force was still attributed to human effort. Later, the application of heat sources as the origin of the force to enable further travel and transport of heavier materials was considered. Steam engines were invented first and then gasoline engines were developed. A considerable amount of effort has been devoted to developing several types of engines, for example, in the category of jet engines. In addition, many types of heat sources have been investigated.

Jet engine types include turboshaft engines and fan engines such as turboprop, propfans, and unducted engines. Propellants as heat sources have grown in size with the conversion of heat energy to mechanical energy. Moreover, the desired travel distance has been increasing, from travel on Earth to travel in space. The large weights of heat sources prevent the realization of travel to the stars. A breakthrough in these difficulties has been eagerly awaited, and a new approach to the realization of travel is expected. Currently, the generation of propulsions is considered a serious issue for long-distance travel.

Propulsion plays an important role in a wide variety of applications. All creatures, such as humans, birds, insects, and fish, are closely related to the movement in their own lives. Additionally, their movement is closely related to the generation of forces for their sustenance. Therefore, the topic of propulsion is crucial when considering the evolution of creatures. However, this topic has a wide range of applications. Thus, it is difficult to cover all the applications of propulsion in such a small book. Accordingly, we have selected typical examples from among many important applications.

Chapter 1 presents a summary of the book, while Chapter 2 explains the advantages of hybrid rockets using solids and liquids. These rockets were developed for ascent vehicles for travel to Mars. This chapter also presents the design of a test setup for hybrid motor firing. Moreover, the proposed hybrid propulsion system is demonstrated to provide sustainable, safe, and low-cost systems for space missions. Chapter 3 presents the proposal of new technology. According to Einstein, inertia and gravitation represent two sides of a coin. An accurate understanding of the role of inertia in general relativity may lead to a breakthrough in advanced propulsion.

Therefore, a rest mass fluctuation can be used for propulsion when inertia is gravitationally induced. Recent work supported by National Innovative Advanced Concepts Phase 1 and Phase 2 NASA grants can be made to work. The most general statement of the principle of relativity is captured in Einstein's equivalence principle and the gravitational induction of inertia. Recent design innovations have significantly increased the thrust produced by these Mach-effect gravitational assist (MEGA) impulse engines. Chapter 4 explains the recent development of an engine using plasma called the Hall thruster. Rocket engines can be of two types depending on the fuel source, namely, chemical and electric rockets. Electrostatic thrusters are useful for launching small satellites in low Earth orbitals and are capable of firing for long time intervals. Space scientists are interested in developing thrusters based on electric propulsion technology from the perspective of cost reduction. This chapter provides a general overview of the technology of electric propulsion and its applications. Plasma-based electric propulsion technology has been used for space missions with regard to spacecraft station keeping, rephrasing, and orbit topping applications. Chapter 5 describes the special low noise engine thrust management at take-off and approach for supersonic civil airplanes. The assessment of noise levels at certification reference points is conducted by considering two engine noise sources, namely, the fan and exhaust jet. Finally, by considering a simple model of a thin plate, Chapter 6 discusses the generation of force caused by unsteady motion. In such unsteady motions, vortex generation plays an important role. This mechanism is considerably different from that of the forces produced by the momentum change based on the combustion of the propellant. Furthermore, "virtual momentum" is vital in understanding the mechanism of force generated by the movements, such as the travel of insects and birds through fluids.

As mentioned, in addition to human travel, insect and bird flying is the minimum movement required for living. For a deeper understanding of the mechanism of force generation, further research is required. Besides the analyses of motion in 2D, an analytical approach towards those of the motion in 3D will be expected to be carried out. Viscous effects on force generation are also a theme in this field. Moreover, we intend to further investigate the development of powerful engines with more efficient devices.

Kazuo Matsuuchi
Professor Emeritus,
University of Tsukuba,
Japan

Hiroaki Hasegawa
Professor,
Department of Mechanical and Intelligent Engineering,
Utsunomiya University,
Japan

Chapter 1

Introductory Chapter: Propulsion and Movement

Kazuo Matsuuchi

1. Introduction

Almost all animals move around frequently in their surrounding. Their aim is to travel in search of food or to propagate their species. Changing positions is important for survival and also in balancing and improving the environment. As plants cannot move by themselves, they depend on various things transported by animals. For example, the pollen transported by insects is the essential mechanism for plant reproduction. Transportation and movement are important factors for adapting to the change in various environments.

Movement and transport of different things is inevitable part of human life. Without movement or change of place, survival is difficult. Much efforts have been devoted to the development of the means for transportation of larger and heavier materials, and also over a long distance. To understand the movement of any object it is necessary to know the action of forces such as propulsion and drag ones.

In general, propulsions are closely related to the momentum change in the concerned system. We take the simplest case in which an object of mass m is moving with the velocity v. Newton's second law of motion is written as

$$F = \frac{\mathrm{d}(m\,v)}{\mathrm{d}t},$$ (1)

where F is the force acting on the mass. Integration of the above formula between t_1 to t_2 gives the averaged force, $\overline{F}$, given by

$$\overline{F} = \frac{m_2 v_2 - m_1 v_1}{t_2 - t_1},$$ (2)

where $m_1 v_1$ and $m_2 v_2$ are the momentum at $t = t_1$ and t_2, respectively. It is well known that the difference between the momentum at two instants produces some kind of forces. The evaluation of the difference determines its magnitude. To determine the magnitude of forces some calculations of the difference is necessary and it is the first step for understanding the origin.

However, there are many cases in which the usual momentum is difficult to estimate. Suppose, for example, a bird is flying in the sky. The fluid around the bird dominates in an infinite space, the integration for the calculations over the whole fluid does not give a finite value. To evaluate the momentum for the movements of insects, birds, or fish, another quantity called as the virtual momentum should be calculated instead of the usual momentum. This topic will be discussed in detail later.

Next we mention the application in engineering field. Let us take an example in aeronautical field. Recently, jet engines with extremely large thrust and high efficiency have been developed, while the extremely loud noise generated by the high

speed jet has suppressed largely, i.e., the development of the jet engine has become environment-friendly [1]. A typical example of the high-bypass engine designed on this principle is shown schematically in **Figure 1**. This type of engine produces stronger thrust by blowing out a larger mass rather than at a higher velocity for the change of momentum.

Such research and development are aimed at the improvement for easier movement in our surrounding. Rocket engines using chemical reaction have been developed to travel outside of earth. To travel to the space, other types of rocket engines, for example, the ion-engine has often been used. This type of engine utilizes ionized gases as the propellant. However, it is impossible to travel further in space, because of the problem of inevitable heavy weight of fuel. The journey to the stars is now being discussed [2]. In the discussion, Newton's classical dynamics might fail and will be replaced by that of the general theory of relativity.

Now we go back to the discussion of motion of insects, fish or birds in more detail. These creatures efficiently utilize the unsteadiness [3, 4]. Formation of a coherent structure called the leading edge vortex (LEV) is a typical structure in the generation of unsteady force. Many authors have published studies on this topic and hilighted its importance, experimentally and numerically. The magnitude of the unsteady force cannot be explained by a steady-state approach. In many cases the unsteadiness generates *larger* forces more efficiently than that in the steady state. Experiments have been conducted in three-dimensional space and numerical analyses have been carried out to understand the mechanism of generation of force. These studies explained several aspects of unsteady phenomenon. How does the behavior of vortices affect the generation of force? In particular, how does momentum change depend on the force? We are yet to devise a method to estimate the momentum of a unsteady vortex system that changes in a complex manner. Characteristics such as the magnitude, the rotation direction, and the position play the key role in determining the momentum. Unless we determine their properties, the evaluation of force cannot be made quantitatively.

When an object of a constant circulation Γ moves with a constant speed $\mathrm{d}x_0/\mathrm{d}t$, a fluid force acts perpendicular to the direction of motion. The magnitude is given by $\rho(\mathrm{d}x_0/\mathrm{d}t)\Gamma$ (Kutta-Joukowski theorem) [5]. It should be noted that the magnitude is the derivative of the *virtual momentum* $\rho x_0 \Gamma$ with respect to time. Here, ρ is the density of the fluid. This is the simplest application of a well-known law that governs the conservation of momentum. In other words, this is a typical example of the application of the second law of motion to cases including vortices. This simple example is an application to steady motion, however, the estimation of force even
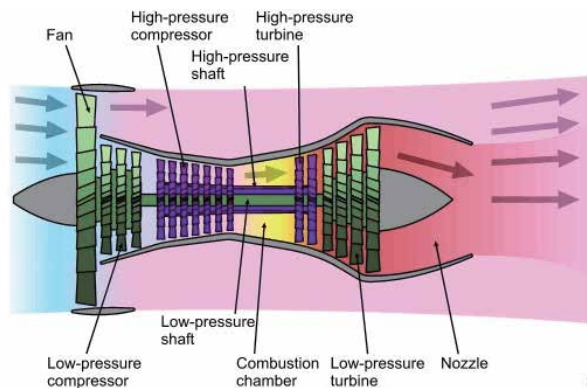
Figure 1.
An example of the cross-section of the jet engine of high-bypass ratio implemented in modern aircrafts [1].
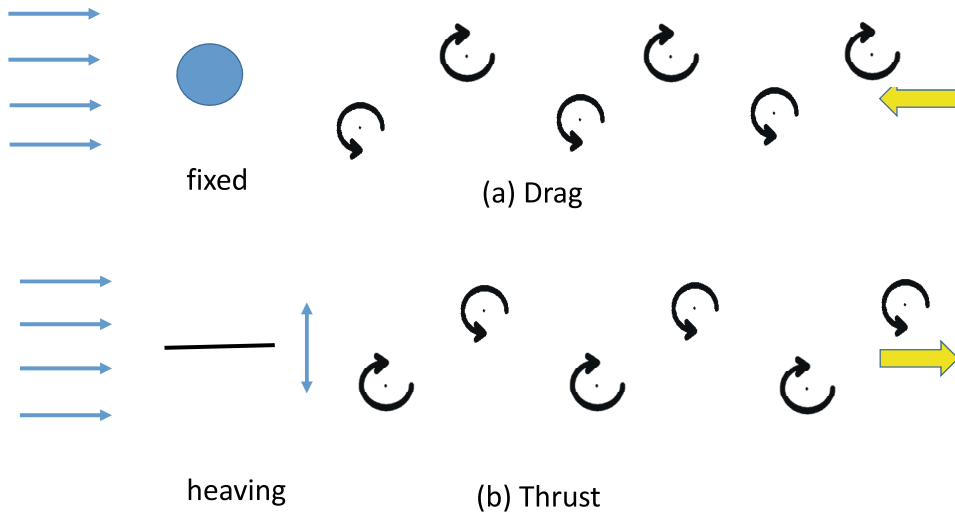
Figure 2.
Vortex street and an object in the stream. (a) An object fixed in the free stream; (b) a thin aerofoil heaving vertically. Two thick arrows denote the direction of momentum increase resulting from the induced velocities due to the vortices.

for such unsteady flow is easy by knowing the virtual momentum. As illustrated above, the virtual momentum is important for the generation of force even for unsteady flows. Among many examples, the application to a heaving motion of a thin plate is the simplest. The importance of the virtual momentum is evident from the discussions about a thin plate. Another importance is that the motion has an analytical solution in the limit as the heaving amplitude becomes smaller.

As an example, let us consider the relation between the force acting on a body fixed in a stream and free vortices flowing down behind it. It is known that a drag acts on a still body set in the stream. We can see two vortex rows, also known as the Kármán vortex street (see **Figure 2a**).

On the other hand, a similar vortex street can be seen behind flying birds and swimming fish. However, the direction of rotation of vortices is quite opposite to the above case. In the case of the Kármán street, there appears to be momentum defect in the street, while the momentum seems to increase behind the birds and fish. In the latter case, a thrust acts on the object to move forward due to the momentum rise. We illustrate the vortex streets appearing in heaving motion (see **Figure 2b**). In the figure the thick arrows represent the direction of the increased momentum. Two typical examples mentioned above are ideal examples for explaining the function of the virtual momentum.

Author details

Kazuo Matsuuchi
University of Tsukuba, Japan

*Address all correspondence to: hinoya1yu@yahoo.co.jp

IntechOpen

References

[1] IAQ International Academy of Quality 2016 https://en.wikipedia.org/wiki/Bypass_ratio [Accessed: 21 September 2021].

[2] S. Scoles. 2019 The good kind of crazy: The quest for exotic propulsion. *Scientific American* August, **321–2**, 58–65.

[3] Dickinson, M.. 2001 Solving the mystery of insects use a combination of aerodynamic effects to remain aloft. *Scientific American* June, 35–41.

[4] Trianthafyllou, M.S. & Trianthafyllou, G.S.. 1995 An efficient swimming machine. *Scientific American* March, 64–70.

[5] Lamb, H.. *Hydrodynamics*, sixth edn. 1932; Cambrige Univ.

Hybrid Propulsion System: Novel Propellant Design for Mars Ascent Vehicles

Ozan Kara and Arif Karabeyoglu

Abstract

This chapter briefly introduces hybrid rocket propulsion for general audience. Advantageous of hybrid rockets over solids and liquids are presented. This chapter also explains how to design a test setup for hybrid motor firings. Hybrid propulsion provides sustainable, safe and low cost systems for space missions. Therefore, this chapter proposes hybrid propulsion system for Mars Ascent Vehicles. Paraffin wax is the fuel of the rocket. Propulsion system uses CO_2/N_2O mixture as the oxidizer. The goal is to understand the ignition capability of the CO_2 as an in-situ oxidizer on Mars. CO_2 is known as major combustion product in the nature. However, it can only burn with metallic powders. Thus, metallic additives are added in the fuel grain. Results show that CO_2 increase slows down the chemical kinetics thus reduces the adiabatic flame temperature. Maximum flammability limit is achieved at 75% CO_2 by mass in the oxidizer mixture. Flame temperature is 1700 K at 75% CO_2. Ignition quenches below the 1700 K.

Keywords: hybrid rockets, CO_2 combustion, metallic additives, paraffin wax, mars ascent vehicle

1. Introduction

Mars is known to have the most suitable geological features and atmospheric conditions for the future human spaceflight. Based on the data from the orbiters and rovers sent through deep space, Mars has the most active volcanic mountains and the highest impact craters of all the worlds. Strong evidences via rover measurements moots that liquid water may have poured across the surface of Mars billions of years ago [1]. There is also evidence of methane leakage between rocks that could be an indication of microbial life. Furthermore, the location of Mars smooths the way of long-term human spaceflight. Mars is relatively close to Earth compared to other possible planets that may be explored such as Saturn and Jupiter. Venus is closer candidate however it has very harsh atmospheric conditions. High temperature, high density and corrosive nature of environment makes surface of the Venus challenging to survive.

Although Mars is the best candidate for human exploration, there are some challenges during two-way mission. Mars atmosphere has a density of 0.014 kg/m^3 and pressure of 610 Pa at the surface level. Low atmospheric density indicates that if Mars have had liquid water on its surface, it would have been evaporated immediately. In other words, the atmospheric pressure of Mars should be increased in

order to capture water molecules in atmosphere (at least 6.25 *kPa* means Armstrong limit). Armstrong limit is also critical for human body resistance. At this limit, breathable oxygen cannot be delivered to body more than a few minutes. Body fluids such as saliva, urine, tears, and alveoli in the lungs would boil away without a special pressurized body suit. Astronauts on Mars can live at this pressure level with a full-body pressure suit.

Human spaceflight to Red Planet takes at least 18 months with at least six months stay on the surface. Therefore, Martian air vehicles are needed both for surface operations and to return to the Earth. Thin atmosphere (due to low Reynolds number) indicates that only air vehicles such as micro helicopters or gliders can operate on Mars's atmosphere. However, these vehicles can only be used for observation purposes and are not feasible for transportation of large payloads. An advanced propulsion system is needed to fulfill mission requirements for long term two-way missions.

Current propulsion systems are quite expensive and technologically not feasible to fulfill two-way mission. In-situ Resources Utilization (ISRU) technologies are required for low cost and feasible propulsion systems. Both air breathing and rocket engines can be used as an ISRU based system. However, airbreathing engines need extremely large inlet areas due to the low atmospheric pressure of the Red Planet. Moreover, the condensed phase combustion products make the turbojet engine impractical. All these circumstances make rocket propulsion systems more practical for Martian operations [2].

Therefore, this chapter proposes a novel propulsion system for Mars Ascent Vehicles. Classical hybrid rocket motor configuration is tested as the propulsion system. The concept is supported by practical motor tests. Hybrid motor uses paraffin wax as the fuel binder and metallic powder as the additive. Aluminum and magnesium are mixed with paraffin as fuel additive. Experiments uses CO_2/N_2O mixture as the oxidizer agent. Combustion process as follows; Nitrous oxide reacts with paraffin and melts the metal oxide layer. Then carbon dioxide burn with metallic additive.

There are several factors to use *Paraffin/Metal/CO_2/N_2O* propellant combination. 96% of Mars atmosphere involves the CO_2 which is quite promising for in-situ missions. Carbon dioxide is known as a natural combustion product. It has also fire extinguisher feature. However, CO_2 can only burn with metallic powders. Therefore, *Metal/CO_2* combustion releases significant amount of energy which is quite practical for sustainable Martian operations. CO_2 is self-pressurizing agent that removes the need for an additional pressurizing system in the rocket.

Experimental results show that magnesium has better ignition capability than alumiinum. CO_2 combustion is achieved up to 75% by mass in the oxidizer mixture. Adiabatic flame temperature of the motor is the key parameter for sustainable combustion of the carbon dioxide. Motor ignition quenches below the 1700 K. This is considered as the maximum flammability limit of the CO_2 with paraffin based hybrid motor.

Furthermore, this chapter provides brief knowledge related to hybrid propulsion systems. Hybrids offer safe, reliable, non-hazardous and cost-effective system compared to both liquid and solid systems [3, 4]. Fundamentals of hybrids briefly explained. Common propellant types are stated for hybrid motors. Details of CO_2 based experiments are presented accompanied with fuel grain manufacturing, oxidizer mixing process and combustion characteristics.

2. Hybrid rocket propulsion fundamentals

This section provides fundamental information related to hybrid rocket propulsion. Hybrid rockets provide safety, reliability and environment friendly

manufacturing compared to other conventional rockets. It stores propellants in separate phases as in **Figure 1** [5]. Usually, the oxidizer is in liquid (or gaseous) phase and fuel is in solid phase.

The oxidizer is driven through a main valve into the solid fuel. An injector is used in order to control the oxidizer flow rate. Brass is the common material for the injector due to material properties. Brass is quite durable and resistant to high temperatures. The pressure of the oxidizer is regulated by pressurization system. Helium gas is mostly used as an pressurizing agent. There is an igniter which is placed near the injector manifold for initiating the ignition inside the motor. Igniter compounds moslty consist of potassium nitrate based solid fuels. However, larger rocket motors requires additional igniter motors as presented in [2]. Hybrid rocket motors mostly use circular port grain design. Circular port grains provide easy manufacturing and high regression rates [6]. Combustion occurs inside the grain port by the oxidizer flow and eventually exits through the nozzle. Nozzle throat diameter is designed in order to provide particular chamber pressure inside the motor. Graphite is mostly used for the nozzle manufacturing.

2.1 Hybrid propulsion advantageous

In the solid rocket motors, oxidizer and fuel are mixed as single solid phase. Combustion occurs by heating the solid fuel grain to reach the ignition temperature. Ignition of solid fuel cannot be stopped when it's started thus causes explosive danger. Thrust cannot be adjusted in solid motors that additional control systems are required for the rocket. Liquid motors keep oxidizer and fuel in separate tanks that combustion occurs by mixing propellant in a combustion chamber. Intimate mixture of propellant in a single chamber may cause explosion hazard. Propellant storage also requires exceptional cooling system in pumps, feed system and nozzle.

Hybrid rocket motors, however keeps oxidizer in liquid phase and fuel in solid phase [4]. Oxidizer delivery system (by using single oxidizer tank) reduce the complexity of plumbing compared to liquids. Thus, the ignition can be throttled by a main valve unlike solid motors. Hybrids have inert solid fuel grain thus; the grain manufacturing is safer than solid motors. Besides, it is easy to cast metallic additives in fuel grains to improve the combustion performance. Thus, operation feasibility at low temperatures, long oxidizer storage capability with non-hazardous manufacturing make the hybrids more practical for Mars missions.

2.2 Propellant evaluation in hybrid rockets

Classical hybrid rockets commonly use polymeric fuels such as HTPB (Hydroxyl-Terminated Polybutadiene), HTPE (Hydroxyl-terminated polyether) and PE (Polyethylene). In hybrid motors, a turbulent boundary layer is formed by
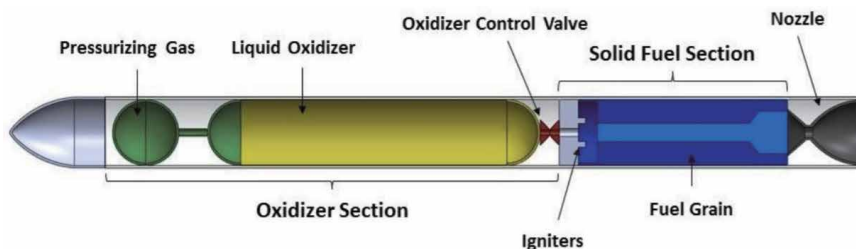
Figure 1.
Paraffin wax liquid entertainment mechanism.

oxidizer injection over the polymeric fuel surface [6]. Thus, the diffusion flame occurs during the ignition at the boundary layer. Diffusion flame is transported on the surface by oxidizer flow. Radiation and convection heat transfer play an important role during this process. Thereby, vaporized fuel on the grain surface reacts with atomized liquid oxidizer causes "blocking effect" at the wall. This blocking effect limits the burn rate of the motor [7].

Paraffin wax is another fuel commonly used in hybrid motors [4]. Paraffin enables 3 to 5 times higher regression rate at the same oxidizer mass flux compared to classical polymeric fuels [6]. Burning paraffin fuel produces a liquid layer over the fuel grain with low viscosity and low surface tension. The liquid melt layer consists of liquified paraffin fuel droplets. This layer merges with the oxidizer flow becomes hydrodynamically unstable in the fuel port. Unstable ignition creates an instability; it lift-offs paraffin fuel droplets from the grain surface that foster the mass transfer rate of fuels into the oxidizer gas flow. This is called as "liquid entrainment mass transfer mechanism" can be seen in **Figure 2** [7]. This additional mass transfer mechanism increases the regression rate of hybrid motor combustion.

Hybrid rockets commonly use N_2O_4 (dinitrogen tetraoxide), H_2O_2 (hydrogen peroxide), gaseous (GOX) or liquid oxygen (LOX) and N_2O (nitrous oxide) as the oxidizer [8]. Nitrogen tetraoxide is storable high-density oxidizer that is used in early launch vehicles. N_2O_4 provides moderate I_{sp} with performance additives. However, it's a high toxic chemical. Hydrogen peroxide is also storable and high-density agent. H_2O_2 is an aggressive chemical at high concentrations. It has leaning to self-decompose thus causes detonation hazard. Typical rocket applications use over 80% concentration levels of H_2O_2 that makes the distillation and handling quite critical for human skin. Liquid oxygen is the most common high-performance oxidizer in the rocket industry. LOX is highly stable due to diatomic oxygen bond and provides high specific impulse. It provides lower oxidizer to fuel ratio that reduces the fraction of oxidizer used in the propulsion system. It is also cost-effective compound. However, LOX is cryogenic material with boiling temperature of 90 K. Cryogenic nature of makes it challenging during surface operations on the Mars. Moreover, liquid oxygen is not self-pressurizing agent due to its low density needs an additional pressurization system via Helium or Nitrogen. This increases complexity and cost of a possible Martian rocket.

Nitrous oxide is another agent has been used mostly in small rocket systems. Nitrous has self-pressurizing capability at saturated liquid state [2]. Self-pressurization eliminates the need of pressurizing system to feed the oxidizer. Thus, it reduces the complexity, weight and cost of the propulsion system.
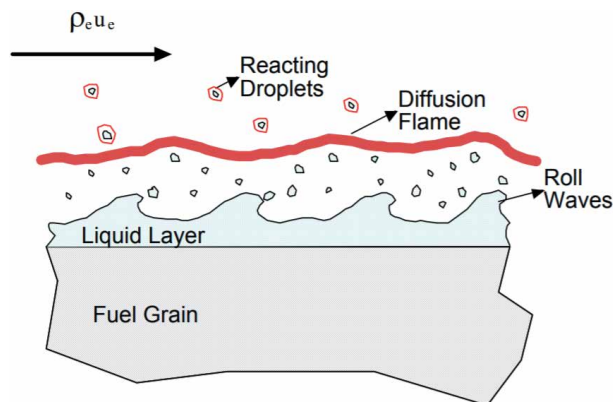
Figure 2.
Paraffin wax liquid entertainment mechanism.

Self-pressurization feature also makes nitrous an efficient candidate for Mars environment. N_2O is non-toxic and easy to handle compared to both N_2O_4, H_2O_2 and *LOX*. Nitrous oxide also creates a highly exothermic decomposition reaction during the combustion. Therefore, it provides stable and efficient ignition in the rocket systems. Nitrous oxide in liquid phase is quite safe and easy to store at room temperature. Highly storable feature makes launch operations quite easy compared to other oxidizer options. Also, its readily available in chemical industry. On the other hand, reduced specific impulse, low density at higher temperatures and strong dependence of the temperature are among several disadvantages of N_2O. It should be noted that nitrous has positive heat of formation. Thus, self-decomposition of "vapor phase" nitrous in feed lines, oxidizer tank and combustion chamber result disruptive damage [9].

2.3 CO_2 as a novel oxidizer

Carbon dioxide is known as a natural combustion product from hydrocarbons or explosions. However, there are certain fuels that remove the carbon–oxygen bond in the CO_2. That is to say metals have higher reactivity series compared to carbon thus removes the carbon oxygen bond. This reaction produces a substantial energy release. Various metals and metal hydrides have been studied in order to understand the combustion characteristics of carbon dioxide as explained in [2, 10–12]. In addition, additional information is presented related to the $Metal/CO_2$ combustion in Chapter 3. However, fundamental findings from [2, 10–12] are explained in this section.

Kara and Karabeyoglu [2] provides practical experiments by using CO_2 as the oxidizer in lab scale hybrid motors. CO_2 is mixed with the nitrous oxide to understand the combustion characteristics. Paraffin based fuel consist of 40 % aluminum powder by mass. Aluminum powder has 3 micron spherical shape. Al has two purity levels 98.75 % and 99.99 %. The purity level has no significant effect on carbon dioxide combustion. According to [2], succesfull combustion is achieved up to 45 % by mass in the oxidizer mixture. In his comprehensive study, Boiron [10] explains the in-situ resources utilization techniques for hybrid propulsion based Mars Ascent Vehicles. Boiron promotes high performance liquid oxygen/paraffin based hybrid rocket system. He proposes two concept missions; Mars Sample Return (36 kg payload mass) and Medium-scale (500 kg payload) Rocket. Borion explains background on in-situ propellant production techniques by using electrolysis methods. He discusses advantageous and disadvantageous of Paraffin/Aluminum/ O_2 / CO_2 propellant combination for Martian rockets. Finally, Boiron presents details Zirconia cell hardware and electrochemical mechanism. Other fundamental researches related to carbondioxide combustion are studied by Shafirovich Gokalp and Zubrin [11, 12]. Shafirovich and Gokalp presents the concept of a metal/carbon dioxide propellant for Mars Sample Return missions. They provide detail thermochemical analysis of CO_2 combustion with various of metals and metal hydrides in rockets. In addition, they provides lab scale combustion experiments with the magnesium. Shafirovich and Gokalp compares several designs for their ascent/decent vehicle such as hybrid engine, liquid monopropellant engine and bipropellant engine. Robert Zubrin who is one of the pioneer scientist in the field of Mars missions proposes diborane and silane for Mars Ascent Vehicles.

Although there are many theoretical studies on $Metal/CO_2$ combustion, it has not been tested in actual hybrid rocket motor. There is an experimental study on combustion characteristics of carbon dioxide with magnesium rocket engines [13]. Yue Lie uses magnesium fuel in powder form with multiple gas injection mechanisms into the combustion chamber at high pressures. Yue presented the

thermodynamic calculations for the combustion process of the multiphase flow environment in a lab scale rocket engine used in the experiments. However, this design seems impractical that gas phase oxidizer needs pressurizing system.

2.4 Metallic powder additives

Metallic powders serve as excellent fuel additives due to their significant volumetric and gravimetric heat release during the combustion process [8]. Purity, size and shape of metallic powders directly affect the combustion performance as they control the ignition delay and the formation of the condensed combustion product (CCP).

Wide range of additives have been studied for CO_2 combustion in rocket motors such as lithium (Li), boron (B), berillyum (Be), aluminum (Al), magnesium (Mg), magnesium hydride (MgH_2), diborane (B_2H_6) and silane (SiH_4). Lithium is highly reactive alkali metal however shows volumetric heat release is low (means low specific impulse) additives due to its low density. Boron is commonly used as a solid propellant additive. Despite it has high combustion energy per unit mass, it delivers poor combustion efficiencies. Major concern of boron is reveals high CCP in the nozzle. Magnesium hydride increase specific impulse however not practical for longer lifetime missions due to its poor dehydrogenation kinetic and hydrogen storage. Casting and lifetime are major issue for all other metal hydrides.

Figure 3 shows the theoratical specific impulse values with respect to oxidizer to fuel ratio. Calculations are made by [11] with 10 bars of chamber pressure.

Diborane is storable at 5 bars in Martian conditions. Diborane shows high mass fraction of CCP effects the specific impulse. Boron oxide formation in liquid form generates a significant risk for slag formation in nozzle throat. Decomposition is
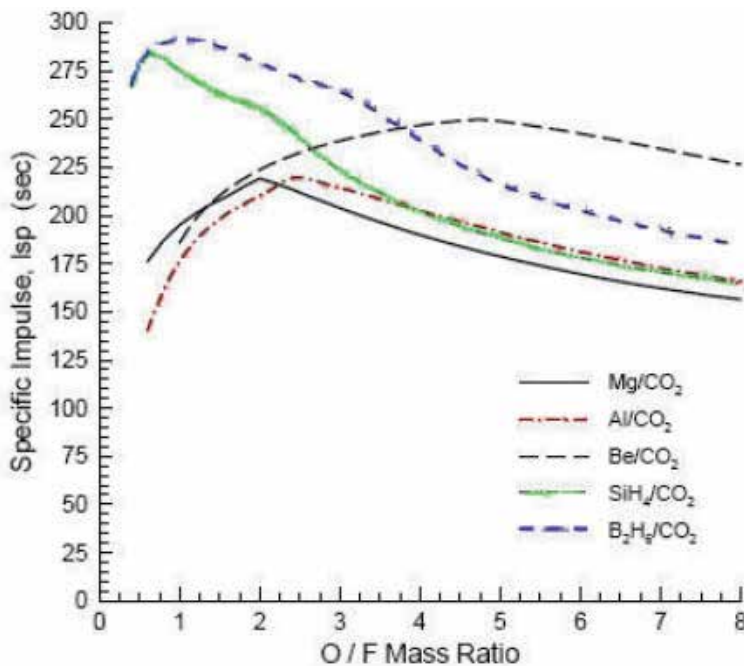
Figure 3.
O/F ratio versus specific impulse – Various of additives.

another factor for diborane. Silane has silicon oxide as the major CCP. It provides lower mass fraction of CCP than diborane. However, silane is quite toxic there is not enough reliable data for SiH_4/CO_2 combustion [10, 12].

Therefore, analysis shows that beryllium, aluminum and magnesium are most prominent candidates for carbon dioxide combustion due to performance and safety aspects. Beryllium is extremely toxic despite its high performance. All in all, magnesium and aluminum are left over as major additives casted in the paraffin wax.

2.5 Aluminum and magnesium combustion with the CO$_2$

Aluminum is low cost and widely used as micron/nano sized metallic powder form. Both spherical and flake shaped aluminum can be casted easily within paraffin wax. Aluminum provides high specific impulse with the CO_2. However, Al/CO_2 combustion produces severe slag formation results nozzle blockage due to oxide (Al_2O_3) formation. Magnesium is can also be found broadly in the market. Mg shows rapid ignition characteristics in carbon dioxide environment due to its low ignition temperature of 1000 K. In addition, metal oxide layer of a magnesium powder sphere is not strong as in aluminum that is easily breakable during combustion. Therefore, magnesium oxide (MgO) formation by Mg/CO_2 reaction is not as severe as in aluminum oxide. It shows less particle agglomeration and two-phase losses in the nozzle.

3. Propellant design for Mars ascent vehicles

This section refers the proper propellant combination for the Mars missions. Mars hoppers, ascent vehicles or any rocket systems can use the proposed propellant combination. Both aluminum and magnesium are proposed as main additive. Paraffin wax is the main binder. In addition, hybrid rocket system uses in-situ CO_2 as the major oxidizer. However, since the pure carbondioxide combustion poses several challenges due to reduces chemical kinetics, N_2O/CO_2 oxidizer mixture is selected for performance analysis.

3.1 Fuel grain manufacturing

Paraffin wax $(C_{32}H_{66})$ is the main binder of the solid fuel grain. Hydrophobic nature of the paraffin protects the metal additives from the water vapor. It is nontoxic thus produces water and carbon dioxide as combustion product. Paraffin has low glass transition temperature $(-180°C)$ that is quite feasible colder periods of Mars atmosphere. Also, inert feature of the paraffin wax is feasible for long duration Mars missions [2, 8].

3 micron sherical shaped aluminum is casted up to 40% by mass in the paraffin. In addition, flake shaped aluminum powder is also tested. Combination of 20% flake 40% spherical aluminum-based fuels have higher carbon dioxide concentration during the combustion. Surface area of flakes are larger than spheres thus initiate the combustion easier. Magnesium is also used in actual motor experiments. 44-micron magnesium powder has 99.99% purity level. Mg amount in paraffin is 60% by mass.

Mixing metallic powders up to 40% by mass is achieved by using Silverson L5M high shear mixer [14]. High shear mixer uses square shaped blades. Mixing metal additive with paraffin binder as follows,

- The required quantity of pure paraffin wax is heated and liquified through a beaker. Then, desired" Structural Additives" are added in the paraffin wax

- Paraffin based formulation mixed again with the High Shear Mixer for 2 minutes at 5000 rpm in order to provide a homogeneous mixture.

- The required quantity of metallic powder is added to the molten paraffin fuel

- Silverson L5M High Shear Mixer at 6000 rpm is used to mix powders uniformly in the molten paraffin wax at 120 °C for 5 minutes to ensure homogeneity

- Liquid binder/additive mixture is casted axially into a phenolic mold that is kept around 80 °C. Thus the fuel grain is allowed for cooling to room temperature. The cooling process takes around 5 hours.

- Finally, fuel grain is machined to the intended circular port and outer diameter.

The **Figure 4** shows the several fuel samples that are casted with the L5M High Shear Mixer. It is worth to note that, although high shear mixer allows homogenous mixture of paraffin and metal powders, increasing magnesium amount to 60% cannot be casted by using high shear mixer due to high viscosity. The structure of 60% magnesium 40% paraffin mixture is like mud that only be casted by hand-mixing in a phenolic mold.

3.2 The oxidizer selection

Hybrid Mars Motor experiments uses CO_2/N_2O oxidizer mixture in blowdown mode. Self-pressurizing capability of both oxidizers makes Martian operations quite practical. In addition, the mixture displays several advantageous such as (i) improved I_{sp} performance compared to pure CO_2, (ii) decreased two-phase losses due to reduced mass fraction of condensed phase products (CO_2 allows additional burning with the condensed phase species), (iii) low freezing point of the oxidizer mixture is ideal for Martian environment (iv) both agendst has self-pressurizing feature that not require any additional pressurizing system in the rocket, (v) low cost, less complicated and lighter compared to liquid bipropellant engines.

Figure 4.
Fuel samples and Silverson L5M high shear mixer [?].

Uniform mixture of N_2O and CO_2 is achieved due to similar fluidic characteristics of agents. **Table 1** summarizes physical characteristics due to NIST database [15].

Mixing two self-pressurizing saturated liquids requires careful process. Actual motor experiments uses 10 liters aluminum scuba tank with maximum operating pressure of 200 bars is the main oxidizer tank. The oxidizer compound that has higher mass fraction first filled in the scuba tank. Then the tank is vented to cool the oxidizer and reduce the tank pressure around 30 bars. The reduced tank pressure allows second oxidizer (source tank that has higher pressure) compound to add the scuba tank. Therefore, the second oxidizer compound is then added in main tank.

Oxidizer mixture density is the major parameter for the performance analysis of the ignition. Specific volume of the mixed oxidizer is found by using the specific volumes of the components and the mass fraction (χ) of N_2O in the mixture.

$$\overline{v}_{liquid} = v_{N_2O}\chi + v_{CO_2}(1 - \chi) \tag{1}$$

The overall oxidizer density is calculated, by assuming an ideal mixture, using simple formula,

$$\overline{\rho}_{liquid} = 1/\overline{v}_{liquid} \tag{2}$$

Liquid N_2O and CO_2 mixture operates in blow-down mode during experiments. The oxidizer mixture has two-phase flow characteristics in the feed system through the injector. The oxidizer flow is choked at the injector thus downstream pressure (motor chamber pressure) has no effect in the flow rate. A blow-down oxidizer mixture needs an advanced approach by using two phase physics. Because, self-pressurizing N_2O or CO_2 in saturated liquid state cannot be modeled by using fundamental ideal gas, compressible or incompressible flow assumptions. Two phase flow approaches by using Homogeneous Equilibrium Model (HEM) is needed for more precise calculations on flow rate and discharge coefficient.

3.2.1 Two phase flow background

Typical rocket applications require fluid dynamics calculations of the injector and propellant feed system. Most of the liquid propellants such as hydrogen peroxide (H_2O_2), ethanol (C_2H_5OH), RP-1 ($C_{12}H_{24}$) and nitrogen tetraoxide (N_2O_4) can be modeled accurately by using classical incompressible fluid dynamics features. In addition, gaseous propellants such as gaseous oxygen, hydrogen and methane use ideal gas law and compressible fluid assumptions. Liquid oxygen (LOX) can also be

T_{tank}, °C	P_{tank}, bar N_2O	P_{tank}, bar CO_2	ρ_{N_2O} kg/m³	ρ_{CO_2} kg/m³	v_{N_2O} m³/kg	v_{CO_2} m³/kg
0	31.21	34.85	909	927	0.0011037	0.0010782
5	35.40	39.69	884.28	897.26	0.0011354	0.0011160
10	39.99	45.01	856.48	863.64	0.0011735	0.0011613
15	45.03	50.87	824.11	823.33	0.0012185	0.0012177
20	50.55	57.29	785.27	772.28	0.0012737	0.0012930
25	56.60	64.35	737.61	705.05	0.0013460	0.0014075
30	63.25	72.10	678.29	614.56	0.0014533	0.0016855

Table 1.
Saturation properties of N_2O and CO_2.

modeled accurately. Although *LOX* is in a saturated state at cryogenic temperatures, it uses single-phase incompressible flow assumptions. Compressibility (Z) factor of liquid oxygen at 1 atm pressure is 0.004, and 0.97 for saturated cryogenic oxygen vapor. Both values are very close to ideal values 0.0 and 1.0 [16, 17].

Nitrous oxide however has a liquid Z factor of 0.13 and saturated vapor compressibility factor of 0.53 at the room temperature. Therefore, incompressible liquid or ideal gas assumptions become inaccurate for modeling nitrous oxide. N_2O is handled as a two-phase mixture for fluid flow modeling. Two-phase flow modeling means that fluid flows as a mixture of liquid phase and a vapor phase at the same time. A fluid quality factor is required for the fluid flow. Fluid quality is the ratio of the vapor mass fraction divided by the total fluid mass.

Injector modeling of self-pressurizing agents such as nitrous oxide is a complex process [17]. Because, fluid quality factor changes during tank evacuation; liquid phase boils into vapor phase. Therefore, internal tank pressure and fluid density changes during the evacuation. Tank pressure and fluid density directly effects the injector mass flow rate calculations. And changing the mass flow rate directly effects the combustion stability, motor pressure and thrust.

4. Hybrid motor design & propellant performance

This section presents the performance results for $C_{32}H_{66}/Mg/N_2O/CO_2$ and $C_{32}H_{66}/Al/N_2O/CO_2$ propellant combination. Theoretical specific impulse with respect to O/F (oxidizer to fuel) ratio is determined by NASA's Chemical Equilibrium Analysis (CEA) software [18]. Combustion energies of selected propellants are also explained. In addition, hybrid motor design is presented in this section. CAD drawing of the actual motor is presented accompanied with the real ignition process.

Carbon dioxide combustion slows down the chemical kinetics in the motor. This reduces the adiabatic flame temperature of the motor. The combustion boundary of experiments are depending on the adiabatic flame temperature limit. Therefore, the major goal of this section is to present the flame temperature change due to carbon dioxide addition in oxidizer mixture.

4.1 Thermochemical analysis of propellant combination

The **Figure 5** shows the O/F vs I_{sp} for magnesium based propellants. Magnesium is loaded as 60% by mass. CO_2 mass fraction is 70% by mass in the oxidizer mixture. Chamber pressure, combustion efficiency, and area ratio are taken as $38\ bars$, $0.98\ and\ 70$. Ambient pressure is selected as 0.006 bar which is Martian atmospheric pressure value.

Magnesium and carbon dioxide addition to propellant combination clearly reduces the O /F ratio. Carbon dioxide increase in nitrous to 70% shifts to O/F ratio throughout 1. Reduction in O/F has the advantage of lower oxidizer mass tank. This further reduces the required nitrous mass brought from the Earth in a possible Mars Ascent Vehicle design.

The **Figure 6** shows the O/F vs I_{sp} for aluminum based propellants. Al mass fraction is 40% in the paraffin. CO_2 mass fraction is 50% in the oxidizer mixture. Chamber pressure, combustion efficiency, and area ratio are taken as $38\ bars$, $0.90\ and\ 70$.

In **Figure 6**, although theoretical calculation assumes 90% combustion efficiency, practical Al/CO_2 based experiments show actual combustion efficiency of
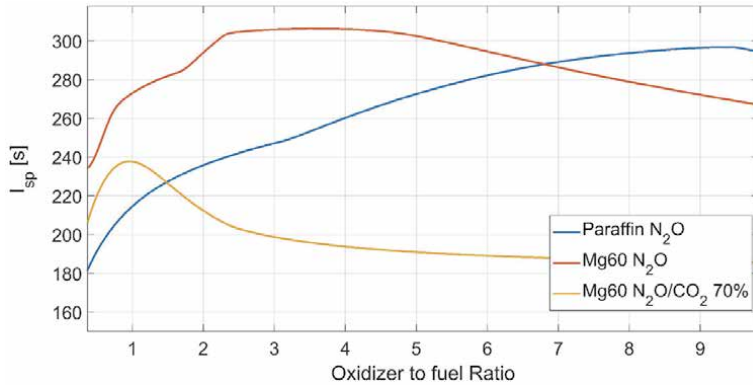
Figure 5.
O/F ratio versus specific impulse – Magnesium based.
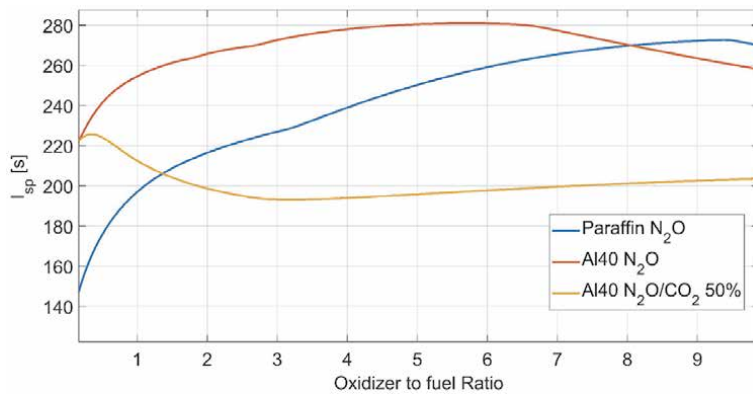
Figure 6.
O/F ratio versus specific impulse – Aluminum based.

70%. Therefore, theoretical I_{sp} of aluminum-based experiments is found as 125 seconds at O/F ratio of 0.5. This shows that magnesium provides better performance and efficiency for MAVs.

4.1.1 Released energies of propellants

Energy analysis is useful indicator of the propellant performance. The energy release due to the combustion is calculated by using heat of reactions (Q_R) of chemical compounds (products and reactants). The Eq. 3 is the formulation for the heat of reaction (combustion) in kJ/kg for the specific propellant. In this equation, $\tilde{Q}_c$ is the heat of formations of products minus reactants. n_m is the mole number and MW is the molecular weight of propellants (reactants).

$$Q_R = \frac{\tilde{Q}_c}{\sum (n_m MW)_{propellant}} \qquad (3)$$

$\tilde{Q}_c$ refers the difference between total heat of formations of products and reactants at 25°C.

$$\tilde{Q}_c = \sum_{products} \Delta \tilde{H}_{f@25°C} - \sum_{reactants} \Delta \tilde{H}_{f@25°C} \qquad (4)$$

17

Propellant Type	Mass fractions	Optimum O/F Ratio	$T_{flame,max}$ K	E_{prop} kJ/kg
$C_{32}H_{66}/Mg/N_2O$	Mg40	5	3385	5801
$C_{32}H_{66}/Al/N_2O$	Al40	5	3570	6962
$C_{32}H_{66}/Mg/N_2O/CO_2$	Mg60 $CO_2$70	0.8	2350	5795
$C_{32}H_{66}/Al/N_2O/CO_2$	Al60 $CO_2$70	0.7	2550	5639
$C_{32}H_{66}/N_2O$	-	8	3263	5307

**Table 2.**
Released Energy Values of Propellants.

Energy analysis of various propellants presented in **Table 2**. Energy releases per kg of propellants is presented due to adiabatic flame temperature at the optimum O/F ratio. **Table 2** shows the fuel additive and carbon dioxide mass fractions and released energy ($Q_R = E_{prop}$) per kg of propellant. Results are negative that means reactions are exothermic.

Table 2 indicates that aluminum provides 35 percent higher energy than the magnesium in N_2O ignition. Furthermore, released energy of 70 % CO_2 based propellant is almost same as *Paraffin/Nitrous* propellant. This means that, although carbon dioxide slows down the chemical kinetics, it provides same energy level as *Paraffin/Nitrous*. Al and Mg provides similar heat of reaction for 70% CO_2. Al and Mg with carbon dioxide provides higher heat of reaction than 70% CO_2 based propellants.

4.2 Rocket motor design

A classical hybrid rocket motor is designed for the experiments. **Figure 7** illustrates the motor layout. The hybrid rocket motor consists of stainless-steel precombustion chamber with 3 grams solid fuel-based pyro section. The pyro is powered with 24 V battery. Pyro releases 5 kW to heat up the motor in 5 seconds. Brass injector chokes the flow therefore downstream pressure has no effect in flow rate. Brass retainer plate is significant to tether the injector. Oxidizer flow rate changes between 40 and 250 grams per second. Graphite insulator in precombustion chamber incarcerates the heat of the pyro fuel. There is a pressure transducer to measure downstream pressure (motor chamber pressure).

Combustion chamber has the 2.5 mm thick phenolic layer for the grain insulation. Single port fuel grain is 180 mm in length. Inner port diameter is 24 mm.
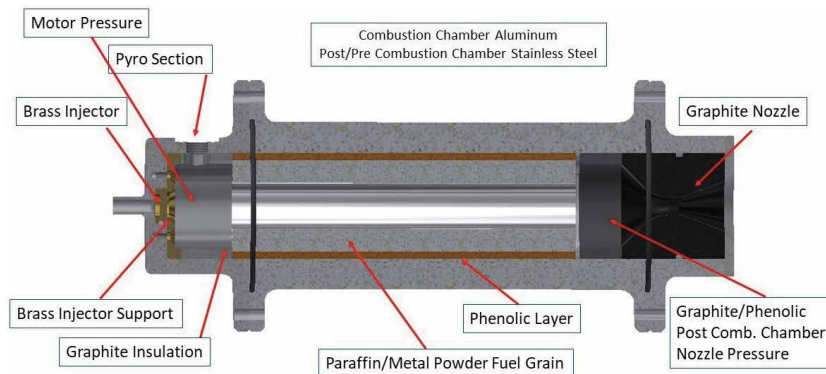
Figure 7.
Mars hybrid rocket motor lay-out.

And the outer grain diameter is 48 mm. Post combustion section has phenolic based layer to absorb the ignition. Nozzle (post combustion) pressure is also measured by the pressure transducer. Motor nozzle is made out from graphite. The throat diameter from 5 to 11 mm to regulate the combustion pressure.

4.2.1 Motor ignition process

The ignition of starts with 2.5 seconds of nitrous combustion (nitrous boost stage). This step exposes enough heat into the motor to take CO_2 combustion easy. Thus, carbon dioxide based combustion (main ignition stage) takes place with an energy boost. The **Figure 8** shows the actual experiment and the test bench.

4.2.2 The complete test setup

The **Figure 9** shows the complete test setup including nitrous boost stage, main ignition stage and purge lines. Nitrous boost stage uses the Aluminum 6061 based oxidizer tank with maximum operating pressure of 280 bars. Nitrous oxide is stored around 50 bars. Nitrous line consist of Mv (manual) and Av (automatic) valves for the operation. Purge line uses the same tank as Nitrous line. Purge tank stores 30
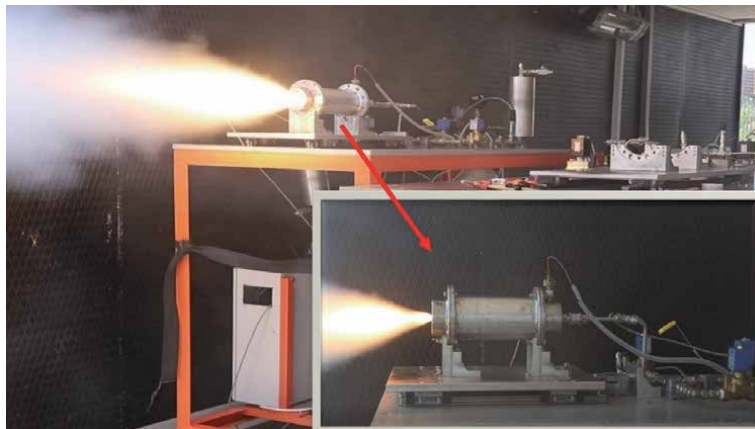
Figure 8.
Actual experiment images.

1. Av Tank Vent
2. Mv Tank Vent
3. Relief Valve
4. PT/TC Ports Tank
5. Mechanical gauge
6. Mv Iso
7. Mv Line Vent
8. Av Main
9. Mv Purge Vent
10. Mv Purge
11. Av Purge
12. Check Valve Line
13. Mv Vent Nitrous
14. PT Nitrous
15. Mv Fill/Main Nitrous
16. Av Main Nitrous
17. Check Valve Nitrous
18. Load Cell
19. Check Valve Motor
20. PT/TC Motor

Main Oxidizer Tank

Nitrous Boost Tank

Mars Hybrid Rocket Motor (MHRM)

Purge Tank

Figure 9.
The complete test setup.

bars nitrogen to cool down the motor after the ignition. Main oxidizer tank is a 10-liter aluminum tank, includes CO_2/N_2O mixture in "blowdown" mode. Main tank has relief with 90 bars cracking pressure. Tank also has vent valves. In addition, mechanical pressure gauge shows the oxidizer pressure as a backup of the National Instruments DAQ system [19].

Check valves are used in all feed lines as well as just before the motor entrance. Check valve prevents hydrocarbon fuel leakage through to nitrous lines. If the nitrous vapor phase interacts with the hydrocarbon, it suddenly decomposes into nitrogen and oxygen (releases +19.5 kcal/mole energy). Karabeyoglu [9] experienced decomposition hazard of nitrous due to deflagration wave as sudden pressure increase from 52 bars to 900 bars in 3 seconds. A K-type thermocouple is used to measure the temperatures. Pressure transducer has measuring efficiency $\pm$ 0.5% of the full measurement scale of 70 bars with repeatability that is better than $\pm$ 0.05%. Pressure/temperature are recorded by using a National Instruments Data Acquisition System and Lab View signal express software. The sampling rate of the DAQ system was set to 5120 Hz. Detail sensitivity features in error analysis is explained in appendix section of this thesis.

5. Combustion boundary of the CO_2

The motor chamber pressure (adiabatic flame temperature) is the key factor to achieve a successful combustion. Combustion quenches below a certain T_{flame} level. Thus, T_{flame} profile of Al tests is shown in **Figure 10**. Aluminum mass fraction in the paraffin wax is increased up to 60% (60% Aluminum and 40% Paraffin wax). In the fuel grain, 20% of this content is casted as 3 micron flaked shaped Al, and 40% is casted as spherical shaped aluminum. Flake shaped powder has larger surface area that forms better ignition characteristics. Thus, successful combustion limit is increased up to 55% CO_2. However, this limit is considered as "stochastic limit" since there are also ignition failures.

Adiabatic flame temperature has different profile in Mg based experiments. Thus the **Figure 11** shows T_{flame} variation due to CO_2 addition at hybrid motor experiments. Combustion quenches (fails) below a certain T_{flame}. The stable ignition occurs at 75% CO_2 level around 1700–1800 K. Ignition quenches below the 1700 K.
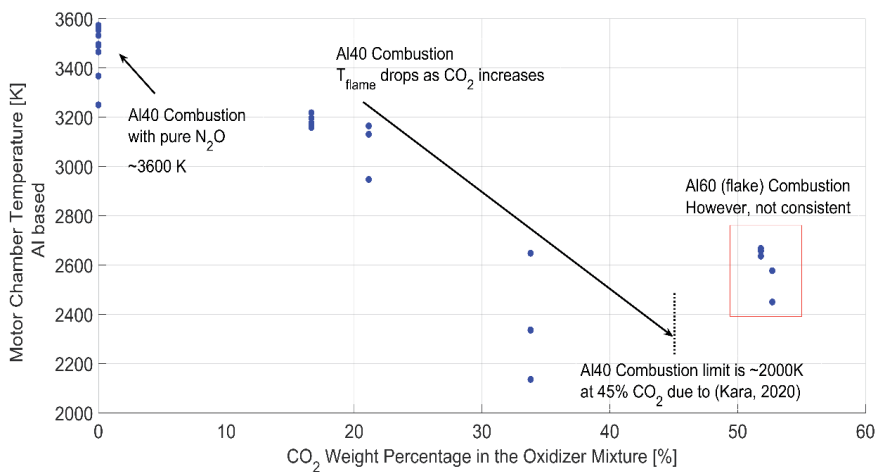
Figure 10.
Flammability limit of Al/CO₂ experiments.
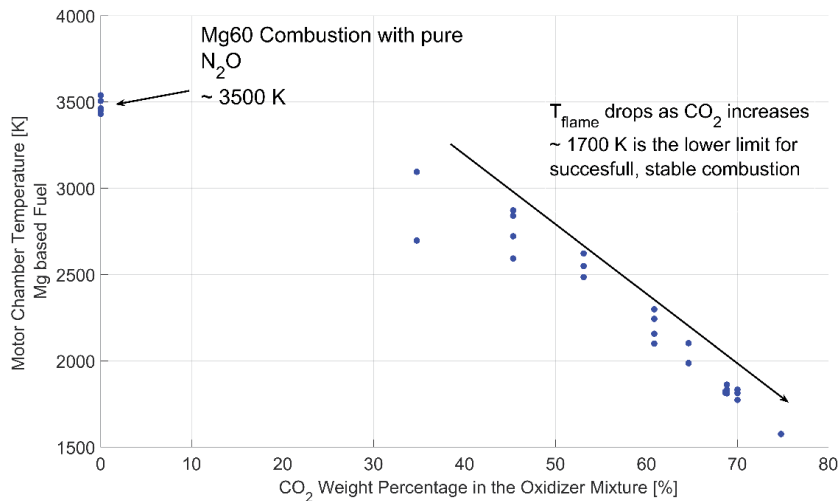
Figure 11.
Flammability limit of Mg/CO₂ experiments.

Figures 10 and **11** show Mg can easily ignites up to 75% carbon dioxide by mass in the oxidizer mixture. Mg has easier ignition capability than the aluminum. For example, flame temperatures of Mg and Al at 35% carbon dioxide are 3000 K and 2400 K. Although aluminum mass fraction increases to 60%, ignition fails around 55% CO_2 level.

Combustion boundary of the CO_2 due to the flame temperature is compared with the literature [20]. In this study, Reina et al. showed the flame temperatures both aluminum and magnesium in CO_2 environment between 1 and 10 bars. Various of powder sizes in micron level are studied. Literature survey by Reina explains that micron sized aluminum has around 1800 K ignition temperature with the carbon dioxide. However, Reina uses nano sized aluminum in their study. Thus, results showed that nanoAl has ignition temperature around 1000 K. Furthermore, ignition temperature is changing between 900-1000 K micro Magnesium based powder.

Therefore, results shows that ignition fail around 1600 K using the *Paraffin/Mg/N₂O/CO₂* propellant. Also, ignition temperature of Mg/CO_2 is found as 1000 K in the literature. This means that excessive 600 K (or more) can be used to vaporize the paraffin wax during the combustion. If the heat required to vaporize paraffin is excluded, the combustion quenches. The increased internal ballistics is needed to achieve higher amount of CO_2.

Combustion mechanism of Metal/CO_2 based propellants also discussed due to oxidizer mass flux of the rocket. Flux dependent results are significant for scale up rocket motor design. The ignition limit also stated as averaged mass flux versus adiabatic flame temperature. **Figure 12** shows that the combustion quenches at motor chamber pressure (adiabatic flame temperature) below the 1600 K. So, the yellow zone is practically impossible region due to ignition boundary. Red dots states the quenched ignitions. In addition, 1000 K is the theoretical combustion value of Mg/CO_2 due to [11, 12] Therefore, the blue zone is theoretically impossible zone for the combustion. Practically possible zone is shown as orange region. Paraffin/Mg based hybrid motor that operates in this region successfully ignites CO_2. There is a quenched ignition point at average mass flux of 375 kg/m^2s for 70 % CO_2. Details of this analysis are explained in PhD thesis version of this book chapter by Kara.
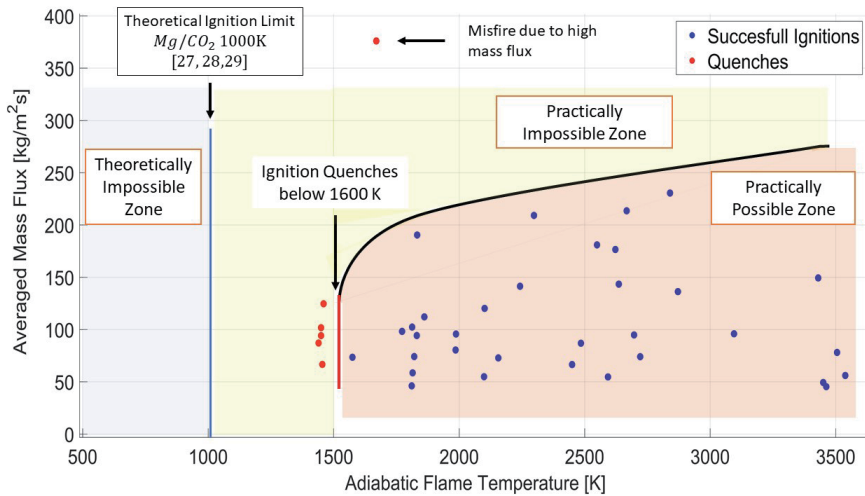
Figure 12.
Oxide formation after the motor experiment.

5.1 Issues during the combustion

Hybrid rocket experiments reveal a significant issue during the combustion. That is the slag formation due to condensed combustion products (CCPs). CCP means the oxide formation as the combustion product. Aluminum (or magnesium) combustion produces aluminum oxide (or magnesium) oxide that has no effect on the combustion performance. Because, combustion performance such as thrust and specific impulse are only formed by the gaseous products. After experiments, 8% of fuel residual is oxides. **Figure 13** shows the motor condition after the experiment. Oxide formation blocks. In addition, poor-quality fuels can be wrapped during the experiment thus blocks the nozzle and the injector.

It is worth to note that although oxide formation reduces the performance, it blocks the nozzle throat and increases the motor chamber pressure during experiment. Therefore, increasing motor chamber pressure causes high efficiency combustion.

5.2 CO_2 combustion: subsequent improvements

subsequent studies will focus on alternative methodologies to achieve higher carbon dioxide combustions. There are several methods that can be considered such

Figure 13.
Oxide formation after the motor experiment.

as (i) magnesium additive mass fraction increase in paraffin wax (up to 80%), (ii) aft injection methodologies to increase adiabatic flame temperature, (iii) Potassium nitrate addition into the fuel grain, and (iv) angled or swirl injection methods. All these methods are currently being used by hybrid propulsion community to improve internal ballistics during the combustions.

6. Hybrid propulsion for Mars ascent vehicles

Mars Ascent Vehicle design concepts are studied by many researchers. Carter [21] discussed technology requirements for propulsion systems such as displacement pumps and bladder lined composite tanks. One of the experimental works for a potential MAV is presented by Karp with paraffin-based fuel and Mixed Oxides of Nitrogen (MON-3) oxidizer [22]. Furthermore, Evans and Karabeyoglu also studied MON based oxidizer for MAV experiment with metallized SP7 fuel by using 30 microns sized aluminum powder [23]. SP7 paraffin-based solid fuel is developed by Space Propulsion Group, Inc., specifically for this program.

This chapter proposes a classical hybrid propulsion system by using $Paraffin/Mg/CO_2/N_2O$ propellant combination is totally feasible for MAVs. Propellant combination provides significant cost savings as well as ease of manufacturing. Self-pressurizing capability of oxidizers also make the system simple and safe. Reduction in oxidizer to fuel ratio is another advantage of the system that reveals lighter oxidizer tank.

A hybrid rocket motor with a 38 bars combustion pressure, 98% of combustion efficiency, 3 kg/s of oxidizer mass flow rate and nozzle area ratio of 70 provides 250 seconds of specific impulse at an oxidizer to fuel ratio (O/F) of 1.1. Also, the thrust level of this single motor is found as 13 kN. Therefore, a potential Mars Sounding Rocket with total fuel mass of 40 kg have total oxidizer mass of 44 kg. Total propellant mass corresponds 84 kg. 1 kg payload mass is assumed to transfer a sample from a point to another on the Mars. Structure mass of the rocket is estimated as 18 kg consist of motor interface, motor casing, measurement devices and the oxidizer feed system (plumbing and valves). Avionics and power system is 5 kg. Nosecone is 2 kg.

The oxidizer tank mass is depending on the density of the oxidizer at 50 bars. It is worth to note that saturated oxidizer mixture at 50 bars need the tank temperature of 15°C. Mars atmospheric temperatures changing between −70 and 20°C near the equator. Thus, a heater system with a simple thermostat can be used at night times to increase the temperature to 15°C. On the other hand, launch can be performed in Martian summer days such as July or August.

At the 50 bars, CO_2/N_2O mixture has a liquid phase density of 816 kg/m^3. 44 kg of oxidizer makes 54 liters of oxidizer tank for the liquid phase. Therefore, tank mass with 4 mm thickness is 8.7 kg.

The sounding rocket has 17 seconds burn time and the mass ratio $\left(n = \frac{M_{initial}}{M_{final}} \right)$ of 4.8. 2-DOF calculation shows that rocket have 47 km downrange distance with 24 km burn out altitude. The maximum altitude achieved is 2 km. However, 3-DOF calculation is needed in order to increase the launch precision. The proposed rocket system can be scaled up as Mars Ascent Vehicle. By using the same performance parameters, ΔV of MAV system is found as 3850 m/s. In addition, ΔV requirement of 500 km low Martian orbit is found as 3652.3 m/s. It is worth to note that drag force is neglected since the calculation needs the drag coefficient. Drag coefficient will be analyzed in future study as the MAV trajectory design.
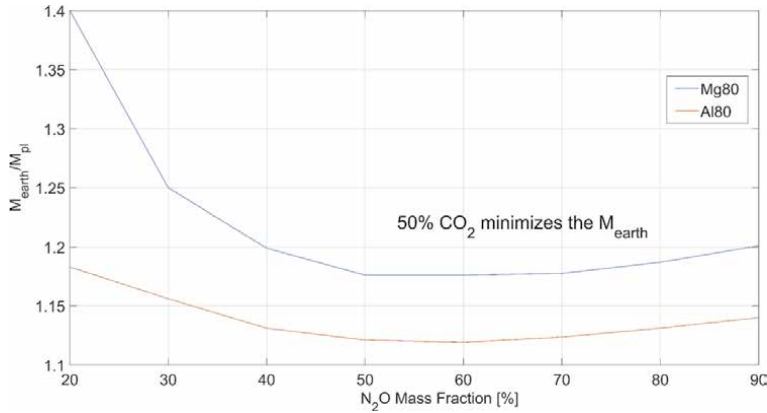
Figure 14.
Oxide formation after the motor experiment.

Potential MAV design needs at least two staged rocket design to fulfill 3652 m/s delta-V requirement. Because specific impulse of propellant selection is quite low for a single staged rocket. Thus, single staged rockets can be used for Mars ballistic hopper missions (such as Mars Sounding Rocket). In addition, oxidizer mass which is needed to brought from the Earth should be minimized for practical in-situ Mars sounding rocket. Considering a single staged hopper rocket with 1600 m/s reveals following minimization process. Eq. (5) is used for this minimization process.

$$\frac{M_{earth}}{M_{pl}} = \left[\frac{e^{\Delta V_{del}/Ispg_0} - 1}{1 - \epsilon e^{\Delta V_{del}/Ispg_0}}\right]\left[\epsilon + \left[\frac{1 - \epsilon}{1 + O/F}(1 + \alpha O/F)\right]\right] \tag{5}$$

ϵ is the structural mass fraction. α is the nitrous oxide mass fraction in the oxidizer mixture. Nitrous mass fraction is the key parameter refers the earth based mass. O/F ratio is taken from CEA.

Earth based mass is minimized due to the payload mass. **Figure 14** summarizes minimized M_{earth}/M_{pl} due to nitrous oxide mass fraction for magnesium powder cases.

Although practical experiments are performed due to the Mg60 based fuel grains, Mg80 shows minimum mass fraction. Minimum values are taken at optimum O/F ratios. In addition, **Figure 14** shows minimum values both for Al80 and Mg80. Aluminum provides 5% smaller fraction than the magnesium. However, Al80 ignition with CO_2. is not practical.

7. Conclusion

This book chapter aims the explain the fundamentals of the hybrid propulsion system. In addition, readers can also be understand the practical setup configuration in hybrid rockets. Experimental tests are performed in order to understand the combustion characteristics of the carbon dioxide. Paraffin wax based fuel is the main binder. Aluminum and magnesium are selected as fuel additive. CO_2/N_2O mixture provides sustainable combustion mechanism.

This work concludes that $Paraffin/Mg/CO_2/N_2O$ is the most feasible propellant for Martian rockets. Carbon dioxide addition to the propellant reduces the oxidizer to fuel ratio. This means that Mars rockets can use lighter oxidizer tank. In-situ CO_2

significantly reduces the mass needed to brought from the Earth. Self-pressurizing feature of the CO_2/N_2O reduces complexity and the cost of the rocket. In addition, Mg/CO_2 combustion provides really high motor efficiencies. Hybrid rockets that uses in-situ based *Paraffin/Mg/CO_2/N_2O* is the most prominent candidate due to several aspects such as low cost, safe launch operations, ease of manufacturing, and ease of design.

Acknowledgements

Notes

This study is the brief version of the PhD Thesis presented by Ozan Kara at KOC University, Istanbul, Turkey. In addition, an extended version of this also found in AIAA Journal of Propulsion and Power.

Nomenclature

c_p	Heat capacity
E_{prop}	Released Energy (after the combustion)
I_{sp}	Specific Impulse
$M_{initial}$	Initial Rocket Mass
M_{final}	Final (burnout) Rocket Mass
n	Mass Ratio: Ratio of initial to final rocket masses
O/F	Oxidizer to Fuel Ratio
T_{comb}	Adiabatic Flame Temperature (Combustion Temperature)
T_{ref}	Reference temperature
T_{tank}	Tank Temperature, Oxidizer
P_{tank}	Tank Pressure, Oxidizer
χ	Mass Fraction
v_{N_2O}	Specific Volume, Nitrous Oxide liquid phase
v_{CO_2}	Specific Volume, Carbon dioxide liquid phase
$\bar{v}_{liquid}$	Average Specific Volume, liquid pha
ρ_{N_2O}	Density, Nitrous Oxide liquid phase
ρ_{CO_2}	Density, Carbon dioxide liquid phase
$\bar{\rho}_{liquid}$	Average Density, Liquid Phase
ΔH_f	Sensible Enthalpy
ΔV	delta V

Abbreviations

CAD	Computer Aided Design
CCP	Condensed Combustion Product
CEA	Chemical Equilibrium Analysis
DAQ	Data Acqusition
HEM	Homogeneous Equilibrium Model

HTPB	Hydroxyl-Terminated Polybutadiene
HTPE	Hydroxyl-terminated polyether
MAV	Mars Ascent Vehicle
MON	Mixed Oxides of Nitrogen
NASA	The National Aeronautics and Space Administration
PE	Polyethylene

Author details

Ozan Kara[1,2*†] and Arif Karabeyoglu[2]

1 DeltaV Space Technologies Inc., Istanbul, Turkey

2 Department of Mechanical Engineering, KOC University, Istanbul, Turkey

*Address all correspondence to: okara13@ku.edu.tr

† These authors contributed equally.

IntechOpen

References

[1] NASA Mars Exploration Program News. Odyssey finds water ice in abundance under mars' surface. https://mars.nasa.gov/news/247/odyssey-finds-water-ice-in-abundance-under-mars-surface/, 2002.

[2] O. Kara, H. Karakas, and A. Karabeyoglu. Hybrid rockets with mixed N_2O/CO_2 oxidizers for mars ascent vehicles. *Acta Astronautica*, 175(0094-5765):254 – 267, 2020, https://doi.org/10.1016/j.actaastro.2020.05.060.

[3] M. Chiaverini and K. Kuo. *Fundamentals of Hybrid Rocket Combustion and Propulsion (Progress in Astronautics and Aeronautics)*. 1st Edition. AIAA, March 15, 2007.

[4] G. P. Sutton and O. Biblarz. *Rocket Propulsion Elements*. 9th Edition. Wiley, Hoboken, NJ, 2016.

[5] R. Gelain. *CFD Simulations of Self-Pressurized Nitrous Oxide Hybrid Rocket Motors*. Master Thesis, 2016–2017 Semester.

[6] D. Altman and H. Holzman. *Overview and History of Hybrid Rocket Propulsion*. 1st Edition. Fundamentals of Hybrid Rocket Combustion and Propulsion, AIAA, March 15, 2007

[7] A. Karabeyoglu, B. Cantwell, and J. Stevens. Evaluation of homologous series of normalalkanes as hybrid rocket fuels. In *41st AIAA/ASME/SAE/ASEE Join Propulsion Conference and Exhibit*, July 2005, https://doi.org/10.2514/6.2005-3908.

[8] A. Karabeyoglu and U. ArÄ±kan. Evaluation of fuel additives for hybrid rockets and sfrj systems. In *50th AIAA/ASME/ASEE Joint Propulsion Conference*, July 2014, https://doi.org/10.2514/6.2014-3647.

[9] A. Karabeyoglu, J. Dyer, J. Stevens, and B. Cantwell. Modeling of N_2O decomposition events. In *44th AIAA/ASME/SAE/ASEE Joint Propulsion Conference and Exhibit*, July 2008, https://doi.org/10.2514/6.2008-4933 .

[10] A. J. Boiron and B. Cantwell. Hybrid rocket propulsion and in-situ propellant production for future mars missions. In *49th AIAA/ASME/SAE/ASEE Joint Propulsion Conference*, July 2013, https://doi.org/10.2514/6.2013-3899 .

[11] I.GÃ kalp and E. Shafirovich. The concept of a rocket engine using CO_2/metal propellant for mars sample return mission. In *3rd International Conference*, 10-13 October 2000.

[12] Robert Zubrin. Diborane/CO_2 rockets for use in mars ascent vehicles. In *31st Joint Propulsion Conference and Exhibit*, July 1995, https://doi.org/10.2514/6.1995-2640 .

[13] Y. Li, C. Hu, X. Zhu, J. Hu, X.Hu, C. Li, and Y. Cai. Experimental study on combustion characteristics of powder magnesium and carbon dioxide in rocket engine. *Acta Astronautica*, 155: 334 – 349, 2019, https://doi.org/10.1016/j.actaastro.2018.11.006.

[14] Silverson L5M High Shear Mixer. www.silverson.com/us/products/laboratory-mixers/.

[15] NIST Chemistry Webbook. https://webbook.nist.gov/chemistry/ .

[16] J.Dyer, G. Zilliac, A. Karabeyoglu A. Sadhwani, E.Doran, Z. Dunnand, and K. Lohner. Modeling feed system flow physics for self-pressuring propellants. In *43rd AIAA/ASME/SAE/ASEE Join Propulsion Conference and Exhibit*, July 2007, https://doi.org/10.2514/6.2007-5702.

[17] Stephen A. Whitmore and Spencer N. Chandler. Engineering model for

self-pressurizing saturated N_2O propellant feed systems. *Journal of Propulsion and Power*, 26(4), 2010, https://doi.org/10.2514/1.47131.

[18] B.J. McBride, M. J. Zehe, and S. Gordon. The nasa cea (chemical equilibrium with applications. In *NASA Glenn Coefficients for Calculating Thermodynamic Properties of Individual Species*, NASA TP-2002-211556 2002.

[19] National Instruments DAQ system. https://www.ni.com/en-tr/shop/data-acquisition.html .

[20] A. Reina, G. Colombo, L. deLuca, F. Maggi, I. Lesniak, D. Lempert, and G. Manelis. Magnesium and aluminum ignition in co_2 atmosphere. 2009,XX Italian Association of Aeronautics and Astronautics (AIDAA) Congress.

[21] P H Carter, F Mitlitsky, A H Weisberg, J C Whitehead, and R W Humble. Design trade space for a mars ascent vehicle for a mars sample return mission. *Acta Astronautica*, 45(4-9):311, 318, 1999.

[22] A Karp, M Redmond, B Nakazono, D Vaughan, R Shotwell, G Story, D Jackson, and D Young. Technology development and design of a hybrid mars ascent vehicle concept. *IEEE Aerospace Conference*, pages Big Sky, MT, 2016.

[23] A Karabeyoglu and B Evans. Development and testing of sp7 fuel for mars ascent vehicle application. *53rd AIAA/SAE/ASEE Joint Propulsion Conference*, pages Atlanta, GA, 2017.

Keeping the Dream Alive: Is Propellant-less Propulsion Possible?

James F. Woodward

Abstract

"Breakthrough" advanced propulsion can only take place with a correct understanding of the role of inertia in general relativity. Einstein was convinced that inertia and gravitation were the obverse and reverse of the coin. The most general statement of the principle of relativity, captured in his Equivalence Principle and the gravitational induction of inertia. His ideas and how they have fared are reprised. A rest mass fluctuation that is expected when inertia is gravitationally induced is then mentioned that can be used for propulsion. Recent work supported by National Innovative Advanced Concepts Phase 1 and 2 NASA grants to determine whether thrusters based on gravitationally induced inertia can actually be made to work is presented. A recent design innovation has dramatically increased the thrust produced by these Mach Effect Gravity Assist (MEGA) impulse engines.

Keywords: origin of inertia, general relativity, gravitational induction of inertia, Mach effect mass fluctuations, Mach effect gravity assist (MEGA) impulse engines

1. Introduction

The dream of getting to the stars is at least as old as it has been understood that the stars are Sun-like objects at vast distances. A dream because of the vast distances; 4 light years being the distance to the nearest star. No technology that is widely accepted is presently known that will get us to the stars in some preferably small fraction of a human lifetime. The mainstays of current space access are chemical rockets for heavy lift and electric propulsion for in-space propulsion. They both require the transport of propellant that is accelerated as it is ejected from the spacecraft to produce thrust. Much less than getting to the nearest stars, even getting to the outer Solar System quickly requires prohibitive amounts of propellant. This problem has led to a number of speculative solution suggestions within well understood physics – none of them convincingly practicable.

Some years ago, I pointed out that were Einstein correct in claiming that inertia is an inductive gravitational phenomenon, as he asserted in his general relativity theory, then one could predict that masses of bodies with changing internal energies subjected to proper accelerations should transiently change their rest masses by much larger amounts than the simple E/c^2 contribution due to the changing internal energy, owing to its "amplification" by the interaction with local gravitational field due to distant matter that Einstein identified, following Mach, as the cause of inertia. These rest mass fluctuations are "Mach effects". Laid out in a series of

research papers over the years, and in 2012 this culminated in *Making Starships and Stargates: the Science of Interstellar Propulsion and Absurdly Benign Wormholes* [1]. Here I update the first five chapters of that work.

2. Inertia, gravity, propulsion and Mach effects

Before Einstein, it was assumed that significant gravitational effects are only produced by astrophysical scale objects. Planets. Stars. And larger mass concentrations. Gravity was not viewed as part of the solution of the propulsion problem. It was/is the propulsion problem. Aside from using the gravitational interaction with astrophysical objects as slingshot "gravity assist" encounters, this belief is still held essentially universally. Einstein's elaboration of the principle of relativity changed this. He called his theory of gravity "general relativity" (GR), not his theory of gravity. Why? Because GR is a theory of gravity *and* inertia, which are coupled by the *principle* of relativity expressed at the most elementary level by his Equivalence Principle (EP). The EP consists of the observation that you must look out the window of a rocket ship to determine whether you are accelerating (smoothly) at one gee in deep outer space, or at rest on a launch pad on Earth. Before the EP, the principle of relativity was restricted to inertial systems. First invented by Galileo, and then codified by Newton in his laws of motion, it says that if you are moving according to the first law, you must go to a window to determine whether you are moving with respect to other objects in different inertial frames of reference. Inertia in Newtonian mechanics is a (magical) property of material objects conferred on them by their existence in absolute space. And when such objects are given (proper) accelerations by the application of external forces, absolute space springs to life to produce the force that opposes the acceleration, acting through the object on the accelerating agent. This conception of inertia is still widely believed, notwithstanding Einstein's efforts to change it.

Einstein, with his theory of Special Relativity (SR), started the changes in the concept of inertia that are still with us today. The first was a paper in 1905 where he asked if the energy content of a body contributed to its inertial mass? [2]. The answer, of course, is the most famous equation in human history: $E = mc^2$. The vacuum speed of light, c, is the important factor in this equation. In SR, c, is a constant with the same numerical value for all observers everywhere/when, a speed that cannot be exceeded by any observer. The fact that c is a constant means that space and time are not physically distinct and independent as they are in Newtonian mechanics. The interdependence of space and time is captured in the Lorentz transformations that take one from one inertial frame of reference to another moving with respect to the first with some non-zero velocity. His next step, taken two years later, was the Equivalence Principle (EP). About the time that Einstein was discovering the EP, his former instructor, Hermann Minkowski, was reconstructing the absolute space and time of Newton into the modern conception of relativistic spacetime. Still absolute though, as inertia therein is still a magical property of space that confers inertial mass on its material contents and springs to life to provide the force that opposes proper accelerations of the massive contents. This conception of spacetime has long carried Minkowski's name. In a sense, it is the culmination of Newtonian physics – the last Newtonian word on space and time where gravity is treated as just another of the forces of nature akin to electricity and magnetism.

The conception of spacetime that Einstein was adumbrating in his speculation on the equivalence of inertia and gravity was motivated by Mach's observation that local inertial frames do not rotate with respect to the "fixed stars" [cosmologically distant matter]. Mach had suggested that distant matter acts through a long-range interaction

with local matter. This was fundamentally different conceptually from Minkowski's spacetime. Einstein put down his speculations on inertia and gravity in an invited paper for an annual review of medicine in 1912: Is There a Gravitational Effect Which is Analogous to Electrodynamic Induction? [3]. In particular, he was interested in the interaction of a test mass located at the center of a spherical shell of matter when they were relatively accelerated – a situation considered by a number of relativists since the early 20th century, though recently in the context of "frame dragging". Inductive of effects of the sort Einstein was interested in are not present in scalar theories of gravity like Newton's; they only appear in vector and tensor theories like electrodynamics and GR. So, Einstein was reduced to fudging with his relationship between energy and mass to get the result he wanted. Namely, that the gravitational potential energy of the test particle contributes to its mass. And if the mass shell were sufficiently massive, producing a Newtonian potential inside the shell equal to the square of the vacuum speed of light, the entire mass of the test particle could be accounted for. Noting Mach in this connection, he opined, "The degree to which this conception is justified will become known when we will be fortunate enough to have come into possession of a serviceable dynamics of gravitation."

Einstein went on to consider the gravitational force produced by relative acceleration of his test particle and mass shell, finding that the gravitational potential energy of their interaction produces a force that tends to drag the test particle with the motion of the shell proportional to the gravitational potential energy divided by c^2. He did not note that were the potential roughly equal to c^2, the test particle would move rigidly with the accelerating shell. And were the particle held stationary by an external force, the accelerating shell would produce the inertial reaction force felt by the agent holding the test particle in place.

The serviceable dynamics of gravitation that Einstein sought turned out to be GR, the correct field equations being found by him in November of 1915. Prediction of the anomalous advance of Mercury's perihelion, together with Eddington's confirmation of Einstein's prediction of deflection of light passing close to the Sun in the 1919 solar eclipse catapulted Einstein and his theory to international popular acclaim. Shortly after the initial publication of GR, Einstein mooted his ideas about "Mach's principle", the assertion that inertia was due to the gravitational action of mostly matter at cosmological distances. This led to an exchange with Willem deSitter – who showed that Einstein's field equations were consistent with several solutions thereof that were obviously inconsistent with Mach's principle – that convinced Einstein to abandon the principle. It is now widely thought that this meant that Einstein had abandoned the idea that inertia was gravitational in origin. This is not correct. While he had abandoned the most extreme version of the principle, which requires an "action-at-a-distance" field theory, Tullio Levi-Civita had reminded him that inertia is an integral part of GR, and like gravity, satisfies the EP. Einstein retreated from full-blown Mach's principle to what he called "the relativity of inertia". Still a Machian conception of inertia.

Einstein advanced his ideas first in an address at Leiden in 1920 where he analogized his evolving view of spacetime to the "aether" of the turn of the century theory of electrodynamics. And then he extended his view in remarks in a series of lectures at Princeton in 1921 [4]. There he calculated the action of some nearby, "spectator" matter on a test particle of unit mass (at the origin of coordinates) in the weak field limit of GR. He found for the equations of motion of the test particle (his Eqs. 118):

$$\left(\frac{d}{dl}\right)\left[(l+\bar{\sigma})\mathbf{v}\right] = \nabla\bar{\sigma} + \frac{\partial\mathbf{A}}{\partial l} + \nabla\times(\mathbf{A}\times\mathbf{v}), \qquad (1)$$

$$\bar{\sigma} = \left(\kappa / 8\pi\right)\int(\sigma / \mathbf{r})\mathbf{dV}_{o}, \qquad (2)$$

$$\mathbf{A} = \left(\kappa / 2\pi\right)\int\left(\sigma\mathbf{dx} / \mathbf{dl}\right)\mathbf{r}^{-1}\mathbf{dV}_{o}. \qquad (3)$$

The second and third of these equations are the expressions for the scalar ($\bar{\sigma}$) and vector (**A**) potentials of the gravitational action of the spectator masses with density σ on the test particle. *l* is coordinate time and v is coordinate velocity of the test particle. The first equation is just Newton's second law. After writing down these equations, Einstein noted approvingly that,

> *The equations of motion, (118), show now, in fact, that*

> *The inert mass [of the test particle of unit mass] is proportional to 1 + σ, and therefore increases when ponderable masses approach the test body.*

> *There is an inductive action of accelerated masses, of the same sign, upon the test body. This is the term dA/dl.*

> *Although these effects are inaccessible to experiment, because κ [Newton's constant of universal gravitation] is so small, nevertheless they certainly exist according to the general theory of relativity. We must see in them strong support for Mach's ideas as to the relativity of all inertial interactions. If we think these ideas consistently through to the end we must expect the whole g$_{\mu\nu}$-field, to be determined by the matter of the universe, and not mainly by the boundary conditions at infinity.*

The way J.A. Wheeler would later, repeatedly put this was, "mass there *rules* inertia here". (He used this remark as the frontispiece for his book with his former student Ignacio Ciufolini, *Gravitation and Inertia* in 1995 [5]).

The above quote was not Einstein's last explicit word on gravity, inertia, and spacetime. In 1924, he again addressed these topics in a paper, "Concerning the Aether" [6]. In it he quickly asserted that by "aether" he did not mean the material aether of turn of the century electromagnetism. Rather, he meant a real, substantial, but not material entity that *is* spacetime, and that spacetime *is* the gravitational field of material sources. No material sources, no spacetime. This was his way of getting rid of the Minkowski and other metrics that de Sitter had shown to be anti-Machian. As he put it toward the end of his article:

> *The general theory of relativity rectified a mischief of classical dynamics. According to the latter, inertia and gravity appear as quite different, mutually independent phenomena, even though they both depend on the same quantity, mass. The theory of relativity resolved this problem by establishing the behavior of the electrically neutral point-mass by the law of the geodetic line, according to which inertial and gravitational effects are no longer considered as separate. In doing so, it attached characteristics to the aether [spacetime] which vary from point to point, determining the metric and the dynamical behavior [sic.] of material points, and determined, in their turn, by physical factors, namely the distribution of mass/energy.*

> *That the aether of general relativity differs from those of classical mechanics and special relativity in that it is not "absolute" but determined, in its locally variable characteristics, by ponderable matter. This determination is a complete one if the universe is finite and closed.*

Arguably, Einstein is the most profound physical thinker yet produced by our species. His physical intuition garnered him the *only* rank zero classification in Lev Landau's ranking of physicists where Galileo, Newton, Faraday and Maxwell were only first rank. One may reasonably ask, if Einstein was convinced that GR, correctly interpreted, encompassed the gravitational induction of inertia, why today is it widely believed in the community of relativists and beyond that inertia is **not** gravitationally induced? That inertia is no better understood than it was in the absolute systems of Newton and Minkowski? Carl Brans. And his "spectator matter" argument.

Brans did his doctoral work at Princeton in the late 1950s. His doctoral supervisor was the noted experimentalist, Robert Dicke. After passing his qualifying exam, Dicke tasked Brans with investigating the question of as the origin of inertia in GR as Dennis Sciama had made "Mach's principle" a central question in GR several years earlier. When Brans read Einstein's remarks on Machian inertia in Einstein's 1921 comments mentioned above, he noted a problem. As Brans later wrote in 1977 [7]:

> Over the years, many and varied expressions of Mach's principle have been proposed, making it one of the most elusive concepts in physics. However, it seems clear that Einstein intended to show that locally measured inertial-mass values are gravitationally coupled to the mass distribution in the universe in his theory. For convenience I repeat the first order geodesic equations given by Einstein to support his argument:
>
> [Brans inserted here Einstein's equations displayed above.]
>
> … Einstein's claim is that "The inertial mass is proportional to $\left(l + \bar{\sigma} \right)$, and therefore increases when ponderable masses approach the test body.

Brans pointed out that having the masses of local objects, the test particle in this case, depend on their gravitational potential energies acquired by interaction with spectator matter must be wrong. Were it true, then the electric charge to mass ratios of elementary particles for example would depend on the presence of nearby matter. Were this true, gravity could be discriminated from accelerations without having to check for the presence of spectator matter by going to the window in a small lab and looking out – a violation of the Equivalence Principle. From this, Brans inferred that

> … global, i.e., nontidal, gravitational fields are completely invisible in such local standard measurements of inertial mass, contrary to Einstein's claim… Einstein ought to have normalized his local space-time measurements to inertial frames, in which the metric has been transformed approximately to the standard Minkowski values, and for which distant-matter contributions are not present [Emphasis added.]

This is the "coordinate condition" required by Brans' work: that the coordinates be compatible with the assumed approximate Minkowski metric applicable in small regions of spacetime. Since the absence of gravity is presupposed for Minkowski spacetime, this amounts to the assumption that the Newtonian potential due to exterior matter in such small regions of spacetime is effectively everywhere/when equal to zero. That is, the locally measured value of the total Newtonian gravitational potential is universally zero. This certainly makes the localization of gravitational potential energy impossible in GR, a now widely accepted fact. And where

there is effectively no gravity, there can be no gravitational induction of inertia. Accordingly, it would seem that the spectator matter argument makes Machian gravitationally induced inertia incompatible with general relativity.

One might think that assuming the locally measured invariance of the Newtonian gravitational potential, since it allegedly requires that it effectively be zero, deprives the potential of its physical meaning, for if it is everywhere/when measured to be the same, how can it have the variations in spacetime – gradients and time derivatives – that characterize local gravitational phenomena? Physically speaking, the answer to this question is informed by the consideration of the vacuum behavior of light. In SR, the vacuum speed of light is constant. It is measured everywhere/when to have exactly the same value by *all* observers. As such, it never has non-vanishing derivatives of any sort. In GR, this changes. The vacuum speed of light remains a *locally* measured invariant. But the vacuum speed of light measured by observers who are not *local* does not have the locally measured invariant value. The vacuum speed of light in the vicinity of a black hole with its strong gravity field, as measured by a distant observer where the local gravity is weak, is slower than the distant observers measurement of the value at his/her location. This is *not* the consequence of some material-like medium being present in the vicinity of the black hole. It is the consequence of *time* running more slowly in strong local gravity fields when measured by distant observers far from strong local sources of gravity. This *fact* about the vacuum speed of light in GR used to be called the *coordinate* speed of light. Since it is not an invariant, global or local, its derivatives do *not* vanish.

Brans' argument led to the adoption of the coordinate condition mentioned above where gravity is effectively absent in sufficiently small regions of spacetime. But the argument actually does not require the adoption of this coordinate condition. If, however, the Newtonian gravitational potential is to have any value other than effectively zero, then it must be a locally measured invariant so that charge to mass ratios of elementary particles do not depend on local gravitational conditions to avoid violations of the EP as Brans showed. But to accommodate real local gravitational phenomena, we must assume that, like the vacuum speed of light, the Newtonian potential has varying *coordinate* values that are not invariant.

Since the gravitational induction of inertia depends on the presence and motions of "matter" (everything that gravitates) chiefly at cosmological distances, the obvious question is: is the needed stuff out there doing what it must do to produce inertial effects? Einstein was clever enough to know that the knowledge of cosmology in the 1920s and beyond was insufficient to make such a determination backed up with observational evidence. Friedmann and Lemaitre made initial explorations of cosmology in the '20s, discovering that sensible solutions of Einstein's equations dictated expanding universes for simple models with homogeneity and isotropy of sources of the field. Their work was elaborated by Robertson and Walker shortly thereafter, leading to so-called FLRW cosmology. Modern cosmology is far better informed by observations and concomitantly more detailed and complicated – though no one has a clue as to what "dark energy" is, it certainly exists. For our purposes, however, the features of cosmology needed to address the gravitational induction of inertia are already present in FLRW cosmology, for recent observations do not call into question the assumptions of homogeneity and isotropy. And a simple argument made by Dennis Sciama in 1953 [8] makes possible knowledge of the motions of cosmological sources important to inertia induction.

Sciama developed his early ideas on the origin of inertia in terms of a vector theory of gravity modeled on Maxwell's equations for electrodynamics. Like Einstein in 1921, he obtained a term in his gravelectric force equation that involves

the time derivative of the vector potential of the gravitational field. The vector potential, **A**, depends on the integration over the matter currents in the observable universe, that is, ρ*v*, where ρ is the matter density in an integration volume element and *v* its velocity relative to the point where **A** is evaluated. Sciama noted that all of the various motions that stuff out there in the universe engage in, on average over sufficiently large distances go to zero. So, to calculate **A**, all we need do is imagine that, say, a test particle is moving with velocity *v* with respect to some cosmic rest frame. The principle of relativity allows us to view the test particle as at rest with the universe moving rigidly past it with velocity -*v*. All of the "peculiar" motions of the stuff out there is irrelevant as they average to zero. This means that the velocity can be removed from the integration over the matter currents, leaving an integration over the matter density. That integration returns the total Newtonian gravitational potential, customarily written as ϕ. As Einstein observed in 1912, up to a factor of order unity, if this potential is equal to the square of the vacuum speed of light, then the entire inertia of the test particle can be attributed to its gravitational interaction with the rest of the universe. And inertial reaction forces are gravitational forces – arising from the $d\mathbf{A}/dt$ term in Einstein's equation of motion above since $d\mathbf{A}/dt = (\phi/c^2)\, d\mathbf{v}/dt = a$ provided that $\phi/c^2 = 1$ always and everywhere.

Is ϕ actually equal to c^2? At least up to a factor of order unity, the answer to this question is yes. For example, Sultana and Kasanas did a calculation assuming all of the features of modern general relativistic cosmology several years ago and got the "right" answer [9]. But there is an even more compelling reason to accept that Mach and Einstein were right about gravitationally induced inertia. *As a matter of observation*, spacetime is spatially flat. In terms of the FLRW cosmological models with their homogeneity and isotropy, cosmic scale spatial flatness is just a curiosity attached to arguably the simplest FLRW model characterized by the exact balance of gravitational potential energy and "kinetic" energy, that is, non-gravitational energy characterized by $E = mc^2$ where m is the inertial mass of the matter in the cosmology. The general FLRW metric can be written introducing a "curvature index" k with values plus or minus 1 and zero. Plus 1 gives the metric for positive curvature spacetime where kinetic energy exceeds potential energy and is "closed". Minus 1 gives the metric where the roles of the energies are reversed and is "open". Closed universes expand and contract whereas open ones expand forever. For k = 0 the energies are exactly the same and spacetime is spatially flat. It expands forever, but with decelerating speed, just stopping at cosmic temporal infinity. In this spacetime we have for material particles:

$$m_g\phi = m_i c^2 \tag{4}$$

where the subscripts g and i identify gravitational and inertial masses of the material particle. This is true everywhere/when in the cosmos. Another peculiar property of the k = 0 solution is that the condition of spatial flatness does not change as cosmic expansion takes place. So, if we apply the EP to cancel the masses in Eq. (4), we find that $\phi = c^2$ obtains universally. The remarkable properties of the spatially flat, k = 0 FLRW cosmology were first formally identified as a problem by Dicke in lectures in 1969, and then in an article written with James Peebles in 1979. He called this the "flatness paradox" because spacetime in even casual observations is obviously spatially flat, but the k = 0 cosmology is "unstable". Small fluctuations in the matter density should drive spacetime quickly into either k = plus or minus 1 behavior – which is not the steady decelerating expansion asymptotically to infinite extent of the k = 0 solution. Why, Dicke asked, is our aged cosmos spatially flat? Alan Guth was in the audience of the 1969 lectures and eventually proposed "inflation" to solve the flatness and other problems.

By 1979 intense discussion of Mach's principle and the gravitational induction of inertia had almost entirely abated. Hoyle and Narlikar had published an action at a distance version of GR. It did not attract much interest. John Wheeler continued to say "mass there *rules* inertia here". His later book *Gravitation and Inertia* with I. Ciufolini [5] makes plain that he was an advocate of a limited version of Einstein's "relativity of inertia", that is, the gravitational induction of the inertial properties of spacetime, but not the gravitational induction of the inertial properties of matter per se. But Brans' spectator matter argument had banished Einstein's version of the gravitational induction of inertia. Was Einstein simply wrong about the gravitational induction of inertia? No. The k = 0 FLRW cosmology does more that allow one to assert that $\phi = c^2$ when the inertial and gravitational masses are canceled in our test particle equation above as they are the same according to the EP. And the fact that this cosmology evolves preserving this condition – notwithstanding Dicke's paradox – means that FLRW k = 0 cosmology automatically makes ϕ a locally measured invariant like c ensuring that the coefficient of the acceleration in the $d\mathbf{A}/dt$ term in the equation of motion is always 1. This is not true in k ≠ 0 cosmologies where the potential and kinetic energies are not equal. So, the answer to Dicke's flatness paradox is not inflation. Inflation may explain *how* flatness comes about. But it is that k = 0 cosmology obtains *because it is required by Newton's third law, the equality and opposition of applied and inertial reaction forces that singles out k = 0 as the correct cosmology.* In other cosmologies ϕ is not equal to c^2 and action does not equal reaction. This makes Brans' spectator matter argument – which locks in the necessity of ϕ being a locally measured invariant equal to c^2 – one of the most consequential developments in general relativity of the past century.

Why bother about what the correct origin of inertia is? After all, if ϕ is a locally measured invariant it is everywhere the same and it seems that it can have no effects beyond pushing back when we try to accelerate massive objects. We live in an enormous gravitational field that we can only detect when we try to change our states of inertial motion. That is, when proper accelerations of material objects are involved. So, to couple to the gigantic gravitational field in which we live, we must accelerate stuff. The question then is, does accelerating stuff do anything other than excite an inertial reaction force? To answer that question we need the gravitational field equation for the inertial force. Since we are looking for relatively large, lowest order effects, we do not need the full formalism of GR. The Newtonian approximation is good enough. But it must be modified to Lorentz invariant form to be realistic. As it happens, George Luchak wrote out the relativistic Newtonian approximation field equations in 1951 when doing an investigation of Patrick Blackett's conjecture on the origin of stellar magnetic fields being the mass currents arising from stellar rotation [10]. The field equation he found was:

$$\nabla \bullet \mathbf{F} + \frac{1}{c}\frac{\partial q}{\partial t} = -4\pi\rho \qquad (5)$$

With

$$\nabla q + \frac{1}{c}\frac{\partial \mathbf{F}}{\partial t} = 0 \qquad (6)$$

and

$$\nabla \times \mathbf{F} = 0. \qquad (7)$$

q is the rate at which the field does work on its local source density. Since the field is irrotational [∇ x **F** = 0], **F** can be written as the gradient of a scalar potential ϕ. *q* is $\partial E_o / \partial t$ where E_o is the proper source energy density, so the second term in Eq. (5) is just the second time derivative of the proper energy density. The time-dependent term in this equation is where rest mass fluctuations are to be sought. The proper energy density E_o is just the proper matter density ρ_o times c^2. But the gravitational induction of inertia lets us write c^2 as ϕ, so $E_o = \rho_o \phi$. Using this relationship and several pages of algebra (see chapter 3 of [1]) yields:

$$\nabla^2 \phi - \frac{1}{c^2}\frac{\partial^2 \phi}{\partial t^2} = 4\pi G \rho_o + \frac{\phi}{\rho_o c^4}\frac{\partial^2 E_o}{\partial t^2} - \left(\frac{\phi}{\rho_o c^4}\right)^2 \left(\frac{\partial E_o}{\partial t}\right)^2 - \frac{1}{c^4}\left(\frac{\partial \phi}{\partial t}\right)^2 \qquad (8)$$

The left-hand side of this equation is the d'Alembertian of the potential ϕ, a wave equation for ϕ with sources on the right-hand side. Since the time-dependent terms on the right-hand side of Eq. (8) originate on the field side of the equation, they do not carry the coefficient $4\pi G$. To be treated as massive sources (and multiplied by $4\pi G$ like ρ_o in the first term on the right-hand side of Eq. (8)) they must be multiplied by the factor ($1/4\pi G$). The time-dependent source terms thus become:

$$\delta m_o = \frac{1}{4\pi G}\left[\frac{\phi}{\rho_o c^4}\frac{\partial^2 E_o}{\partial t^2} - \left(\frac{\phi}{\rho_o c^4}\right)^2 \left(\frac{\partial E_o}{\partial t}\right)^2 - \frac{1}{c^4}\left(\frac{\partial \phi}{\partial t}\right)^2\right] \qquad (9)$$

The first of the terms on the right-hand side of this equation is the largest in most circumstances – and the term on which MEGA impulse engines depend. The second term can be triggered by the first term in special circumstances, but is almost always negligible (see chapter 9 of [1]). The third term is inconsequential.

3. MEGA impulse engines

To excite these rest-mass fluctuations all we need do is make the internal energy density of a massive object change while it is undergoing a proper acceleration. An energy density fluctuation of the sort required is easily produced by charging/discharging a capacitor. The required proper acceleration of the capacitor can be produced with an electro-mechanical actuator – in particular, a device comprised of lead-zirconium-titanate, PZT, elements that expand/contract when a voltage is applied to them. The actuator must be affixed to a "reaction" mass in order for its motions to communicate accelerations to the capacitor undergoing internal energy changes to produce the MEGA mass fluctuations wanted. Since PZT actuator components are also capacitors, the actuators can play the role of both actuator and capacitor simultaneously. One then only needs a stack of PZT disks affixed to a reaction mass to generate mass fluctuations. To make this device into a MEGA impulse engine all we need do is provide for a second mechanical acceleration at the frequency of the mass fluctuations that acts so that this acceleration of the PZT stack is in one direction when the stack is less massive and the opposite direction when it is more massive. This, in effect, makes the PZT stack the propellant of the engine, and the mass fluctuation that arises from the coupling to the cosmic gravitational potential allows one to indefinitely recycle the propellant, Not exactly propellantless propulsion. But you do not have to keep throwing new PZT stacks overboard to produce propulsion. A device of this sort is displayed in **Figure 1**.
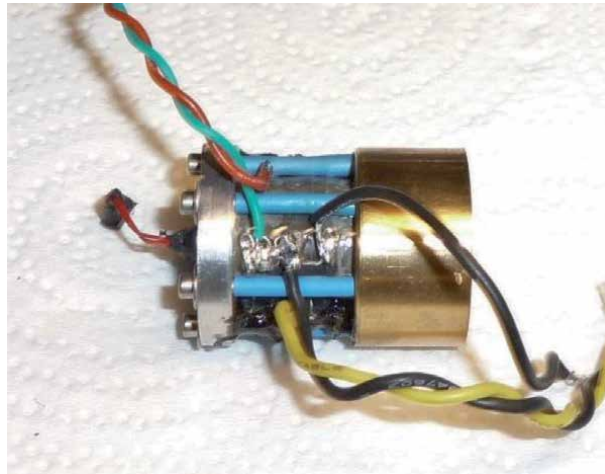
Figure 1.
A stack of 8 PZT crystals 19 mm in diameter by 2 mm thick is clamped between a brass reaction mass and an aluminum cap with 6 4–40 cap screws. A thermistor is embedded in the cap to monitor the temperature of the device and two thin crystals are embedded in the stack near the cap.

The first laboratory test devices of these engines were made in 1999. To make mounting of the devices on a torsion balance possible, a bracket was attached to the back of the reaction mass, as shown in **Figure 2**. A simple L shaped piece of aluminum, initially this bracket was bolted directly onto the reaction mass. The devices hardly worked at all. When a thin rubber pad was placed between the bracket and reaction mass (the black tabs seen in **Figure 2**) the devices sprang to life. It did not take long to figure out that the pad was not damping the vibration of the device. Rather, it was decoupling the device from the mounting bracket at the high (tens of KHz) frequencies of operation, allowing it to vibrate more vigorously as the vibrational energy was not being as strongly sinked into the mounting bracket and beyond. An important change was made in the devices made from 2011 on from the first devices made in 1999. Instead of using Edo Corp material EC-65, Steiner-Martins material SM-111 was substituted. The motivation for this change was the dissipation factor for the SM-111 material is about an order of magnitude smaller than that for EC-65, leading to a much-reduced heating rate in the SM-111 material. An unintended consequence of this material change was that instead of driving the devices with a voltage waveform with both first and second harmonics to get the

Figure 2.
*A device of the type shown in **Figure 1** with an aluminum "L" braket attached for suspension on a torsion balance. Note the black rubber tabs peeking out at the interface of the bracket and the reaction mass.*

desired mechanical response, the new devices can be driven with a single frequency sine wave (with a special step-up/isolation transformer) and the SM-111 material generates the higher harmonics needed to produce thrust when operated near an electro-mechanical resonance of the device.

A quantitative discussion of thrusts generated in these devices when excited with a suitable sine wave voltage is given in [1], pages 174 to 178. In general terms, δm_o is:

$$\delta m_o \approx \frac{1}{4\pi G}\left[\frac{\phi}{\rho_o c^4}\frac{\partial^2 E_o}{\partial t^2}\right] = \frac{\phi}{4\pi G\rho_o c^4}\frac{\partial P}{\partial t} \tag{10}$$

where P us the instantaneous power, that is, in an ideal capacitor, the product of the instantaneous voltage and current across the capacitor. This is the product of two sinusoids of the same frequency and returns a sinusoid of the double frequency, that is, at the second harmonic frequency. If the capacitor is ideal, there is no energy dissipated as the voltage signal is applied and δm_o has no DC offset – and δm_o time-averages to zero. To extract a steady thrust from this mass fluctuation we must provide for a force and mechanical excursion of the capacitor at the second harmonic frequency of the excitation voltage frequency. The second harmonic excursion produces an acceleration with the same frequency, and this acceleration multiplied times δm_o gives the force produced in the capacitor. This is a product of two sinusoids of the same frequency resulting in an AC component with a frequency of 4 times the base frequency plus a DC component that depends on the relative phase of δm_o and the second harmonic acceleration. The DC part of this product is the Mach effect force that can be used for propulsion.

Devices of the sort shown in **Figure 2** were used in work on the Mach effect project until Hal Fearn wrote successful applications first for a Phase 1 (2017) and then Phase 2 (2018) NASA Innovative Advanced Concepts (NIAC) grants from NIAC to support this work. (See [11] for the final report of the Phase 2 grant.) During the Phase 1 and early part of the Phase 2 grants, work focused on a voltage scaling test and issues of vibration and calibration. Typical thrust signals were in the tenths of a micronewton to a micronewton or so, detected with a sensitive torsion balance built with the help of Thomas Mahood a decade earlier shown in **Figure 3**. The device being tested is located in a Faraday cage mounted on a
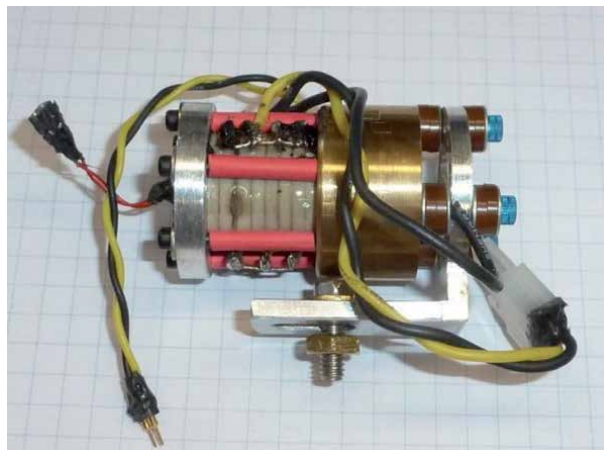

Figure 3.
The torsion balance used in this work for small thrusts on its 500 pound granite vibration isolation table. The vacuum chamber is clear plastic, making careful examination of the operating conditions with a Polytech laser vibrometer easy.

special vibration isolation yoke attached to the near end of the balance beam. One of the aims of the funded work on these grants was to increase the magnitude of the thrusts produced by the tested devices. Other issues just mentioned diverted attention from the increased thrust goal until late 2019 and early 2020. When attention was focused on thrust improvement, the decision was taken to make incremental improvements to the existing devices, rather than go to a radically different design. The obvious design feature to address was the rubber pads that had made the devices work at all. A plan of varying several other design features that might be optimized was also initiated. Shortly after this plan was initiated, COVID-19 struck. Weekly Zoom meetings of the team continued, but at CSUF lab access was restricted to HF, and JFW was restricted to building apparatus to be tested by HF in the lab.

If one understands the role of the rubber pads to be the high frequency decoupling of the device from its support structure, rather than damping the high frequency vibrations, several modifications are straight forward. First, instead of just using a pad between the reaction mass and L bracket, since the pad acts as a spring, pads should be put on both sides of the L bracket. Second, materials other than rubber are surely better candidates. For example, nylon, phenolic, PEEK and Vespel. And these materials can be fabricated with carbon fibers to increase their strength and improve their thermal conductivity. Third, the thickness of the material can be adjusted. An example of one of the devices used in this test campaign is shown in **Figure 4**. The washers on the mounting screws are PEEK in this case. There were, of course, variations in the performance of the various materials and configurations. But all the dielectric washer systems suffered from heating problems that were not resolved even with carbon fiber filling. The thermal problem led to the exploration of metal washers, Belleville washers in particular. Commercial Belleville washers with dimensions similar to the washers in **Figure 4** and the correct stiffness were not available. Washers available in this size had to be glued together to get the correct properties. They solved the thermal problems with the dielectric washers.

In late spring, Paul March and Michelle Broyles began investigating alternate ways of using Belleville washers. They envisioned clamping the reaction mass with a flange at the interface with the PZT stack with big, clunky Belleville washers. This was not the way to go. The flange would not be exactly at a node of all of the vibrations in the device, and clamping it with heavy Belleville washers would doubtless

Figure 4.
A standard device with double thickness PEEK washes on the mounting screws.

at least screw up the pattern of higher harmonic vibrations on which thrust production depends. But a small flange at least near a node of the principal vibration as a mounting point was an appealing idea as the L bracket mounting design was clearly less than optimal. But instead of clamping with clunky Belleville washers, three equally spaced holes were drilled in the flange and lined with Teflon. A support structure with three steel dowels to pass through the holes in the flange was built. When tested, it worked.

This mounting system had a precursor. Several months earlier the L bracket had been replaced by a "sledge" as the part of the L that attached to the Faraday cage. A sledge that was free to move on a small mounting plate bolted to the cage provided with steel dowels on which the sledge rode. That too had worked. But its importance had not been fully appreciated at the time. The flange and dowel mounting scheme made the device itself into a sledge. A number of technical details had to be addressed. The chief detail, however, was that Teflon sleeved holes in the flange were far from frictionless; and frictionless-ness was clearly the ideal if unfettered motion of the device was the goal. With an essentially frictionless mounting system we could approach the ideal of an in space propulsion test. José Rodal remarked that what we needed were miniature linear ball bushings instead of Teflon sleeves. But they were likely prohibitively expensive. All of the team members on the call had experience with linear ball bushings and immediately apprehended the significance of José's observation. Paul and Chip Akins were on it instantly. Before José concluded his remarks about linear ball bushings, they had independently tracked down a source of suitable bushings. They were not prohibitively expensive. The next most important detail was how to extract a very low frequency to stationary force from a device vibrating on dowels with frictionless bearings? Chip and Michelle had the answer: very soft springs that would not transmit the high frequency vibrations to the support frame and would not mess up higher harmonics in the device by applying undue pressure on the "ears" of the flange carrying the bushings. Michelle and Paul eventually tracked down suitable springs.

Tests were done to find the best detailed design for the reaction mass and parts of the supporting frame. The reaction mass design eventually adopted has a flange 3.5 mm thick so that the 5 mm long bushings protrude to center the springs on the dowels that position the device on the dowels. The reaction mass diameter and length were chosen to be 22 mm, making the center of mass of the device lie in the plane of the flange. The PZT stack and aluminum preload cap are those of the L bracket design. A bare assembled device is shown in **Figure 5**. The complete assembly has a mass of 150 gm. It is shown mounted in its supporting aluminum frame in **Figure 6**. The thermistor, strain gauge and power leads are all stress relieved by attachment to the frame. Two of the six springs that position the device on the 2 mm diameter dowels are visible at the top of the picture.

In principle, if the linear ball bushings are functioning correctly, no pseudo force arising from a slip–stick mechanism in the device per se can be transmitted to the support structure owing to the conservation of momentum and the frictionless-ness of the bearings. So, one does not really need the torsion balance with its vibration isolation yoke that ensures slip–stick effects are not transmitted to the bearings of the balance where they might register a false positive "force". Since our vacuum chamber is made of clear plastic, investigating vibration in the parts of the balance with a Polytech laser vibrometer is straight-forward. So, to be doubly certain that real forces are generated in these devices, at first Hal Fearn adapted mounting hardware to place the new style devices on the torsion balance, notwithstanding that the balance acts as a low pass filter for forces with any time dependence. This is shown in **Figure 7**. In addition to recording the voltage and current applied to the device,

Figure 5.
A bare device of the sledge design. The cap is 4.5 mm thick and 28.6 mm in diameter. High strength steel 4–40 cap screws provide the stack preload. Electrical conections are positioned to minimize drag on the motion of the parts.
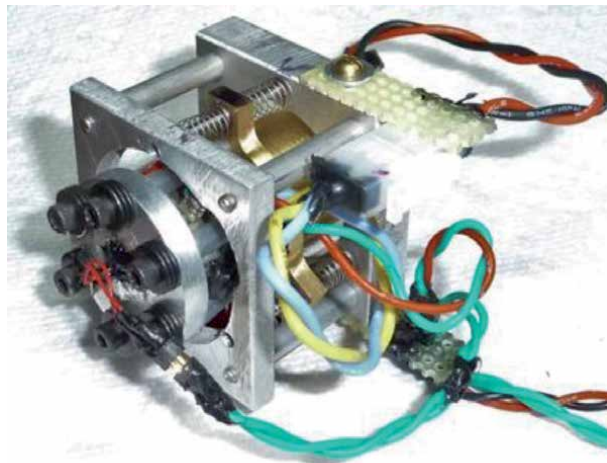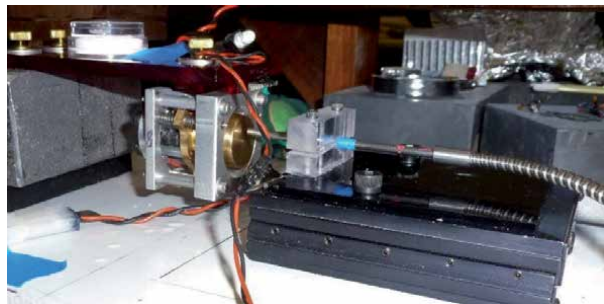

Figure 6.
The device in its supporting frame.

the mechanical activity with the embedded strain gauge, and the temperature with the thermistor in the cap, movies of the device were recorded with a Logitech Brio webcam as the forces produced visible motion of the device on the dowels.

After a few weeks, the Philtech position sensor used with the torsion balance to record its position (and thus force producing any deflection from rest) was removed from the vacuum chamber and repurposed to measuring the position of the sledge mount device on the rods supporting it as shown in **Figure 8**.

The four data signals – voltage, current, strain gauge, and temperature – were captured (along with the movie of the device) by three Picoscope oscilloscopes and displayed on a monitor. One Picoscope was dedicated to the production of a strip chart recoding of the voltage (blue trace) and position (red trace with scale factor 250 microns per volt) and temperature (green trace calculated to a degrees Celsiu8s scale) displayed in the upper left part of the monitor screen. The Picoscope data file of this
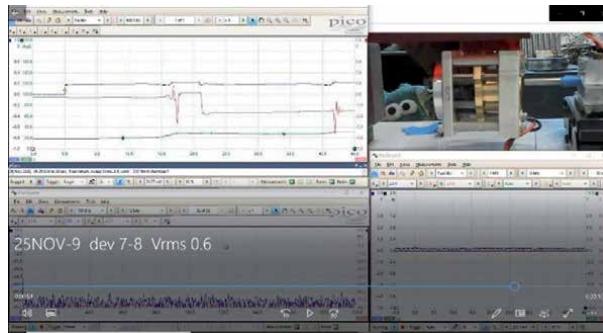
Figure 7.
A sledge mounted device on hardware on the torsion balance in the clear plastic vacuum chamber.
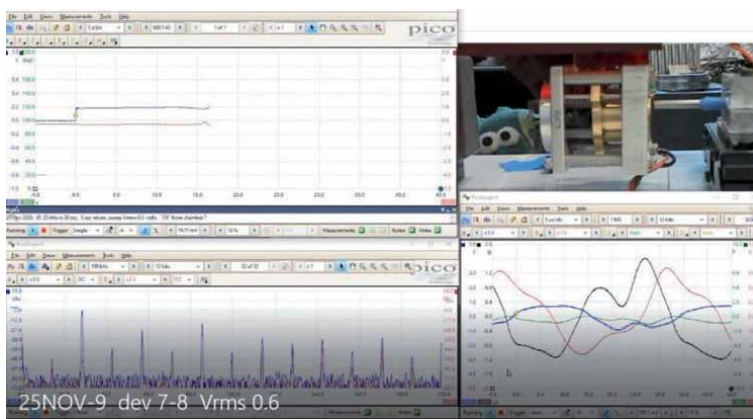

Figure 8.
The device mounted on a cantilever (with bubble level to adjust the levelof the cantilever). The Philtech optical probe is clamped to a micrometer stage for positioning and calibration. It records the distace from the probe to the free end of the reaction mass a millimeter or so away.

display was saved for each run on completion of the run. The second Picoscope was dedicated to the real time capture of the voltage (blue, 100 volts per volt), current (black, one amp per volt), and strain gauge (red, not absolutely calibrated) waveforms during a run. The total power (i X V, green, 20 watts full scale) was computed and displayed in real time. This display is in the lower right of the monitor screen. The third Picoscope, a very fast 2 channel device, was dedicated to the real time display of the FFT power spectra of the voltage (blue) and strain gauge (red) signals located in the lower left part of the monitor screen. The webcam movie was displayed in the upper right of the screen. A picture of the monitor display for a completed run is shown in **Figure 9**. Since our power amplifier was not equipped to track and lock on to signal behavior at or very near resonance, and the thrust resonances for these devices are temperature dependent and – by design – very high Q, frequency sweeps were used to detect the thrust events expected. A typical run would consist of a 20 KHz sweep in 20 seconds (so the frequencies of events could be read off from the time of their occurrence) followed by a 5 second sweep back to the start frequency followed by another 20 second sweep. **Figure 10** shows the monitor screen at the peak amplitudes of the waveforms at resonance transit for the run displayed in **Figure 9**. Note the presence of higher harmonics in the waveforms and power spectra, especially the second harmonic component in the current waveform. If the second harmonic is absent or out of phase, there is no thrust. Just before and after the resonance event,

Figure 9.
The monitor display for a completed run. From the position data the velocity and acceleration of the device on the dowels can be computed.

Figure 10.
The monitor screen at transit of the first thrust resonance in the run displayed in **Figure 9.** *Note the higher harmonics in the waveforms and power spectra, especially the second harmonic in the current waveform.*
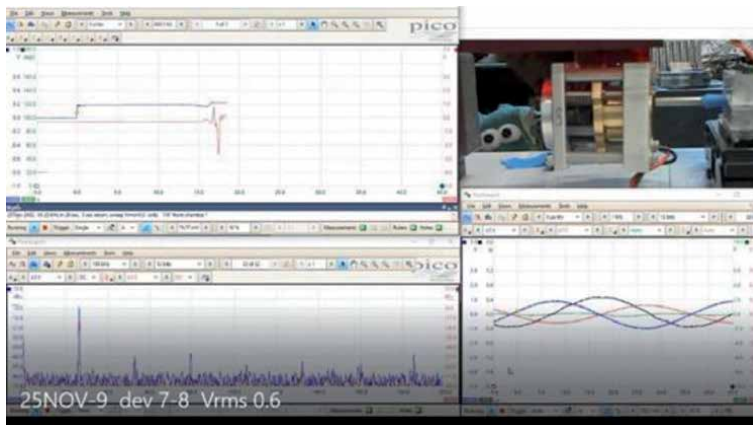
Figure 11.
The monitor screen immediately after the thrust resonance.

the signals look like those in **Figure 11**. The second and higher harmonics are gone. But the strain gauge waveform shows that strong first harmonic vibration is still present. That vibration ensures that the device moves frictionlessly on the support

dowels. The thrust impulse is sufficiently large to initiate the displacement recorded in the strip chart display (red trace) in **Figure 9**. The positioning springs on the dowels convey the thrust to the support frame while arresting the motion of the device and returning it to its rest position. Evidently, these devices work as expected.

4. Conclusion

Many people over the now many years this project has been underway have contributed to its progress in a variety of ways. In my grad student days, those most helpful were Malvin Ruderman, Wolfgang Yourgrau, Allen Breck, Alwyn van der Merwe, James Barcus and Laurence Horwitz. At CSU Fullerton I have enjoyed the tolerance and support of the History and Physics Departments' faculties, especially Ronald Crowley, Dorothy Woolum, Allan Sweedler, Keith Wanser, Mark Shapiro, and Stephen Goode in the Mathematics Department. A number of the formal publications related to this topic (see the technical references in ref. [1] here) were published in *Foundations of Physics*, in part because lists of a half-dozen suggested referees were solicited. I invariably recommended people familiar with both gravity and Wheeler-Feynman action at a distance theory, world class physicists all. And accompanied the lists with the suggestion that the manuscripts be sent to all of my suggested referees. Their comments proved helpful. John Cramer's mention of this work in his *Analog* Alternate View column in the mid-'90s brought this project to the attention of a wider audience. Thomas Mahood through his Master's program and beyond helped in many ways to advance the project. About this time Jim Peoples, Graham O'Neill, Paul March and Sonny White, all then at Lockheed-Martin took interest in the project. As did Frank Meade and Kirk Goodall, and Gary Hudson of the Space Studies Institute (which still supports this work). Others include Nembo Buldrini, Greg Meholic, Marc Millis, Martin Tajmar, Tony Robertson, Paul Murad, John Cole, George Hathaway, and Dennis Bushnell. Peter Milonni and Olivier Costa dé Beauregard made helpful suggestions. Jack Sarfatti, Paul Zielinsky and Nick Herbert contributed by sharpening the arguments related to Einstein's views on the gravitational induction of inertia, as has Lance Williams. Anthony Longman was in no small way responsible for bringing the project to the positive attention of the management of NIAC, Jay Falker, Jason Derleth and Ron Turner. David Mathes, and then Gary Hudson wrote the first and then second unsuccessful NIAC grant proposals. A few years later Heidi (now Hal) Fearn wrote the successful Phase 1 and 2 proposals. Since joining the project in 2012, Hal has been chiefly responsible for advancing the project in many ways. New and improved instrumentation. Data acquisition and analysis. Writing of reports and papers. Giving presentations of on-going work. Organizing workshops and seeing to the publication of their proceedings. Other than Hal, the members of the NIAC grant teams included Marshall Eubanks and José Rodal for Phase 1. In Phase 2 they were joined by Chip Akins, John Brandenburg, Michelle Broyles, Max Comess, David Jenkins, Dan Kennefick, Paul March, and Jon Woodland. The NIAC grants made several advances – notably, thrust increase of two to three orders of magnitude – that otherwise would not have happened possible. To make sure the thrust increase is real, the SSI has engaged George Hathaway to do a replication now in progress. And NIAC has engaged Mike McDonald at NRL to do a replication next year. So, soon we will know if this propulsion scheme really works. Several physicians, Ann Mohrbacher, Ching Fei Chang, Jerold Shinbane, and others at the University of Southern California, have kept me alive these past 15 years.

Acknowledgements

Author details

James F. Woodward
Space Studies Institute and Department of Physics, California State University Fullerton, USA

*Address all correspondence to: jwoodward@fullerton.edu

IntechOpen

References

[1] Woodward JF. *Making Starships and Stargates: the Science of Interstellar Transport and Absurdly Benign Wormholes*. New York: Springer; 2013

[2] Einstein A. Does the inertia of a body depend on its energy content? Annalen der Physik. 1905;**323**(13):639-641

[3] Einstein A. Is There a Gravitational Effect Which Is Analogous to Electrodynamic Induction? Vierteljahrsschrift für gerichliche Medizin und öffentliches Sanitätswesen. 1912;**44**:37-40

[4] Einstein, A., (1921) in: *The Meaning of Relativity*, Princeton Univ. Press, Princeton (1955), 5th ed.

[5] Ciufolini I, Wheeler JA. *Gravitation and Inertia*, Princeton Univ. Princeton: Press; 1995

[6] Einstein, A., "Concerning the Aether," *Verhandlungen der Schweizerischen Naturforschenden Gesellschaft* **105:2**, 85-93 (1924).

[7] Brans CH. Absence of Inertial Induction in General Relativity. Phys. Rev. Lett. 1977;**39**:856-856

[8] Sciama, D., "On the Origin of Inertia," *M.N.R.A.S.*, **34**, 34-42 (1953).

[9] Sultana J, Kasanas D. The Problem of Inertia in Friedmann Universes. Int. J. Modern Phys. D. 2011;**20**(7):1205-1214

[10] Luchak G. A fundamental theory of the magnetism of rotating bodies. Can. J. Phys. 1951;**29**:470-479

[11] NIAC Phase 2 final report. Available at: https://www.nasa.gov/sites/default/files/atoms/files/niac_2018_phii_woodward_macheffects_2_tagged.pdf.

Introduction to Plasma Based Propulsion System: Hall Thrusters

Sukhmander Singh, Sanjeev Kumar, Shravan Kumar Meena and Sujit Kumar Saini

Abstract

Technically, there are two types of propulsion systems namely chemical and electric depending on the sources of the fuel. Electrostatic thrusters are used for launching small satellites in low earth orbit which are capable to provide thrust for long time intervals. These thrusters consume less fuel compared to chemical propulsion systems. Therefore for the cost reduction interests, space scientists are interested to develop thrusters based on electric propulsion technology. This chapter is intended to serve as a general overview of the technology of electric propulsion (EP) and its applications. Plasma based electric propulsion technology used for space missions with regard to the spacecraft station keeping, rephrasing and orbit topping applications. Typical thrusters have a lifespan of 10,000 h and produce thrust of 0.1–1 N. These devices have $\vec{E} \times \vec{B}$ configurations which is used to confine electrons, increasing the electron residence time and allowing more ionization in the channel. Almost 2500 satellites have been launched into orbit till 2020. For example, the ESA SMART-1 mission (Small Mission for Advanced Research in Technology) used a Hall thruster to escape Earth orbit and reach the moon with a small satellite that weighed 367 kg. These satellites carrying small Hall thrusters for orbital corrections in space as thrust is needed to compensate for various ambient forces including atmospheric drag and radiation pressure. The chapter outlines the electric propulsion thruster systems and technologies and their shortcomings. Moreover, the current status of potential research to improve the electric propulsion systems for small satellite has been discussed.

Keywords: electric propulsion, Hall thruster, impulse, exhaust velocity

1. Introduction

When a satellite is placed on a geosynchronous orbit, the attractions of both the Moon and the Sun disrupt the orbit that must be adjusted. Thrusters are used for space missions with regard to the spacecraft station keeping, rephrasing and orbit topping applications. In addition, these kind of devices have implication in partially ionized plasmas (tokamaks), in ionosphere (base of the solar photosphere), in protoplanetary discs, circum nuclear discs in active galactic nuclei and neutron stars. Let us denote $\dot{m}_p$ is the mass flow rate, the exhaust velocity $\vec{U}_{ex}$ and g is the acceleration due to gravity. The performance of thrusters is usually determined by thrust T, which is the total force undergone by the rocket. Thrust also has same unit as a force in newton, which shows the movement of the propulsion system. Thrust, is generated

by the burning of fuel or electrostatic forces. The thrust $T = \dot{m}_p \vec{U}_{ex}$, if the mass flow rate is constant. The specific impulse I_{sp} is used to compare the efficiencies of different type of propulsion systems [1]. The specific impulse is expressed as $I_{sp} = \frac{T}{\dot{m}_p g}$. In general, the higher the specific impulse the less fuel that is required. Therefore the specific impulse simplifies to $I_{sp} = \frac{\vec{U}_{ex}}{g}$. The specific impulse has the dimension of time and is a measure for the effective lifetime of the thruster. The high value of the specific impulse reduces the mission time.

2. The Tsiolkovsky's equation

The rocket equation is used in propulsion systems to find out the different parameters. Therefore high specific impulse related to better efficiency for a propellant. If we denote $\Delta \vec{v} = \vec{v}_f - \vec{v}_i$ as the change of velocity of the rocket, then, the rocket's equation was derived by scientist Tsiolkovsky (1857–1935) and given as

$$\frac{m_f}{m_i} = e^{\frac{-\Delta \vec{v}}{g I_{sp}}} \tag{1}$$

Here m_f is the final mass and m_i is the initial mass of the rocket respectively. Taking natural logarithm on both sides, we get

$$\Delta \vec{v} = g I_{sp} \ln \left(\frac{m_i}{m_f} \right) \tag{2}$$

With this relation, the change in velocity of the rocket can be found out in terms of specific impulse or force. This equation is called Tsiolkovsky's equation. In term of exhaust velocity it turns out to be

$$\Delta \vec{v} = \vec{U}_{ex} \ln \left(\frac{m_f + m_p}{m_f} \right) \tag{3}$$

Here, the mass of propellant $m_p = m_i - m_f$ and m_f is the dry mass of the rocket. It can be seen from Eq. (3) that the higher $d\vec{v}$ requires more propellant. Therefore to achieve higher $d\vec{v}$, the exhaust velocity $\vec{U}_{ex}$ of the propellant needs to be of the order of $d\vec{v}$. To achieve higher $\Delta \vec{v}$, the electric propulsion play a key role in the current time. Various space mission including GEO communication satellite requires a ΔV of approximately 0.6 km/s for a 10-year period.

2.1 Relation between thrust efficiency and input power

If we denote the Thrust efficiency η and the input power P_t then these are related by

$$T = \frac{2\eta P_t}{I_{sp} g} \tag{4}$$

3. Main classes of electric thrusters

Many types of plasma thrusters have been developed over the last 70 years. Mitsubishi electric corporation developed Kaufman ion thrusters for the Japanese

Names of Thrusters	Typical uses	Working mechanism	Electric power (kW)	Specific impulse I_{sp} (s)	T (N)
Hydrazine	Flight space vehicles	Electrothermal: the electric energy is used to heat the propellant that is expanded through a nozzle [3].	0.3 to 2	500 to 600	10^{-3} to 0.2
Hydrogen	For ground testing work		1 to 100	900 to2000	0.1 to 5
Hall effect thrusters	Flight space vehicles	Electrostatic thruster: the electric energy is used to accelerate propellant ions [3].	0.5 to 5	500 to 3000	10^{-2} to 0.4
Gridded ion engines	Flight space vehicles		0.3 to 5	1000 to 4000	10^{-3} to 0.2
Pulsed Plasma Thruster	Attitude control for small sattelites	to form a plasma and expel it out of the nozzle under a magnetic field [3].	.070	80	860 μN
Lithium	For ground testing facilities	Electromagnetic thruster: electromagnetic systems ionize and accelerate the propellant under the combined action of magnetic and electric fields [3].	200 to 1000	2000 to 5000	2 to 15
Hydrogen	For ground testing facilities		1000	5000	15
Variable Specific Impulse Magnetoplasma	Under development	It ionizes the propellant with radio waves to form a plasma, then accelerate it under a magnetic field [3].			

Table 1.
Classification of some electric thrusters.

engineering test satellite in 1994, which had produced 20 mN of thrust (specific impulse of about 2400 s) [2, 3]. Another ion thruster (for commercial station keeping Applications) called Hughes- 13-cm Xenon Ion Propulsion System was launched into orbit in 1997 on the Hughes PAS-5 satellite [4]. The Hughes thrusters produced 18 mN of thrust at specific impulse of 2500 s (efficiency of about 50%).

Based on the acceleration of gases for propulsion, electrical thrusters have been classified into three main categories namely electro thermal, electrostatic and electromagnetic thrusters. In chemical thruster, the exhaust velocity depends to thermal heating, which cannot reach very high magnitude. In a chemical thruster, the propellant is burned and the hot gas is expelled from the thruster with the help of a nozzle but in plasma thrusters the plasma expels without an explosion taking place [2, 3, 5–18]. The performances of different types of electric thrusters have been discussed in **Table 1**.

4. Electrostatic Hall thrusters

In Electrostatic thrusters only ions are accelerated by applying direct electric field at the exit side of the thruster to produce thrust. Hall thrusters were originally invented in United States and Russia 70 years ago. After that they have been widely researched in Europe, Japan, and the China. Hall thrusters have emerged as an integral part of propulsion technology. Unlike chemicals and electric rockets (solid rocket motors, liquid rocket engines and hypergolic engines), the propulsion thrust in a Hall thruster is achieved by a propellant (usually Xenon). Typical chemical thruster specific impulses range around 200–500 sec, though electric thrusters can have specific impulses up to 3000 sec or greater [1, 5–7, 19]. The pressure inside the channel is on the order of 0.1 Pa. Now a days, most of the countries are using the

Hall thruster technology in their space mission. Unlike chemicals and electric rockets, the propulsive thrust in a Hall thruster is achieved by an ionized inert gas (Xenon) which has high atomic number and low ionization potential. For this Xenon is mostly used. In a Hall thruster, the propellant is ionized and then accelerated by electrostatic forces.

Figure 1 shows the internal parts of a plasma Hall thruster. Generally, the discharge channel is cylindrical shape made up with metallic material. The magnetic field of the order of 150 Gauss is applied to produce closed drift of electrons inside the channel. The applied magnetic field, which is strong enough so that the electrons get magnetized, i.e. they are able to gyrate within the discharge channel, but the ions remain unaffected due to their Larmor radius much larger than the dimension of the thruster. The magnetic structure of a conventional HET is constituted of a magnetic circuit with two pole pieces, cores and two magnetic screens, one internal coil and four external coils to achieve a maximum of radial magnetic field in the channel exit.

Thus the electrons remain effectively trapped in azimuthally $\vec{E} \times \vec{B}$ drifts around the annular channel and slowly diffuse towards the anode. This azimuthal drift current of the electrons is referred to as the Hall current. The propellant enters from the left side of the channel via anode and gets ionized through hollow cathode of the device. Hall thrusters can be classified into two categories. One of them is a stationary plasma thruster (has an extended acceleration zone) and second is a thruster with anode layer (has a more narrow acceleration zone). The electric field of strength $\sim$1000 V/m gets generated inside the discharge channel along the axial direction of the device [5]. ISRO (India) used Hall effect ion propulsion thrusters in GSAT-4 back in 2010, carried by GSLV Mk2 D3. It had four Xenon powered thrusters for North–South station keeping. Two of them were Russian and the other two were indigenous.

5. Typical parameters of Hall thrusters

In **Table 2**, typical values of some of the pertinent properties are listed at the thruster exit for the SPT-100.
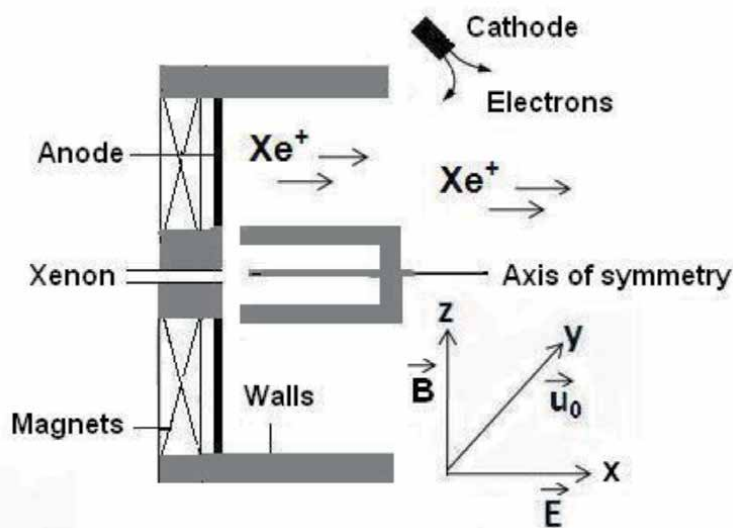
Figure 1.
Schematic diagram of a typical hall plasma thruster.

Property	Typical value	Property	Typical value
Inner diameter	60 mm	Neutral velocity	300m/ s
Outer diameter	100 mm	Electron temperature	5-10 eV
Plasma density	$10^{17}/m^3$	Ion temperature	1-5 eV
Neutral density	$10^{18}/m^3$	Neutral temperature	0.9 eV
Ion velocity	10^4m/s	Debye length	10^{-5} m
Collision mean free	1 m		

Table 2.
Typical values of parameters used in hall thruster.

6. Components of Hall thrusters

There are several ingredients that are responsible for the proper running of a Hall thruster. Below we discuss some important ingredients.

6.1 Propellant

Most of thrusters use xenon as a propellant because of its higher mass (131.3 amu), lower first ionization potential, less toxicity, ionization cross section of 2.3×10^{-6}cm^2. Unfortunately, Xenon is very expensive (compared to Krypton high value of first ionization potential) because of its mere availability at the earth's atmosphere [20].

6.2 Anode and cathode

Latest thrusters have hollow anodes through which the propellant is pumped into a closed channel. The propellant Xenon is stored in a tank on the spacecraft and reaches the anode. Hollow cathodes are used in Hall thruster to provide electrons (with the help of DC electron-discharge plasma generator) to neutralize the body of the spacecraft (to manage spacecraft charging) as well to sustain the plasma discharge and. The hollow cathode are made up with refractory metal tube and lanthanum hexaboride [1–20]. The cathode operates at 30 V to 40 V negative of the anode in a mercury thruster depending on the design consideration.

7. Literature review

Various phenomena have been investigated theoretically, numerically (PIC simulation) and experimentally in Hall thrusters. The physical phenomena currently studied in Hall thrusters are the plasma oscillations of different frequency ranges, propagation and neutralization of the ion beam, electron transport, plasma interaction with a dielectric wall and the plasma sheath. Some of them are discussed below.

7.1 Studies on lifetime

Low frequency oscillation and performance are modified strongly, when the magnetic field configuration is changed. The smaller curvature of the magnetic field configuration suppresses the amplitude of low frequency oscillation and enhances the performance of Hall thruster. There have been many studies on the lifetime of the Hall thrusters, including endurance test and erosion measurements, which

limits the lifetime of the Hall thruster. The erosion depends on wall material, operating condition, channel geometry, magnetic field design and anode configuration. Garrigues et al. [21] have given an emphasis on the thrusters lifetime and reported that configuration with a zero magnetic field and a smaller region with large magnetic field tend to decrease wall erosion and low frequency current oscillations. Dorf et al. [22] reported that thruster operation is more stable with the coated anode. Barral and Miedzik [23] investigated the role of inductor-capacitor and resistor-inductor-capacitor networks in the stabilization of the plasma discharge. Tahara et al. [24] have studied the effects of channel wall material on Hall thruster performance. Ahedo and Escobar [25] have studied the influence of design and operation parameters on Hall thruster performances.

7.2 Studies on plasma plume

The structure of the plasma plume exhaust from the thruster is of great interest since its huge exhaust-beam divergence may cause communication interference of satellites and electrostatic charging problems. Askhabov *et al*. [26] found that the plasma jet has a half angle of 45° and the electron temperature monotonically decays along the jet and drops by an order of magnitude at 10 m. The plasma potential was found to be substantially increased with the distance from the thruster exit. This is an important result in view of the effective acceleration potential drop [27]. Fruchtman theoretically [28] shown that the control of the electric-field profile in the Hall thruster through the positioning of an additional electrode along the channel is to enhance the efficiency. Keidar and Boyd [29] have studied the effect of the magnetic field on the plasma plume of a Hall thruster.

7.3 Studies on oscillations and instabilities

The plasma density, external electric and magnetic fields in a Hall thruster are in inhomogeneous form and are not in the thermodynamically equilibrium state. These deviations act as a source of plasma instabilities. These oscillations and instabilities in the Hall thruster may affect the divergence of the ion beam and electron transport across the magnetic field which control the productivity of the system. Choueiri [11] has qualitatively discussed the nature of oscillations in 1 kHz–60 MHz frequency range that have been observed during operation of Hall thrusters. The typical range of oscillations have been recognized in Hall thrusters, such as 10–20 kHz discharge oscillations, 5–25 kHz rotating spokes (due to ionization process), 20–60 kHz azimuthal modes (due to drift type instability associated with gradient of density and magnetic field), 70–500 kHz transient time (ion residence time in the channel), 0.5–5 MHz azimuthal wave and high frequency oscillations (**Table 1**). The above waves regulate the efficacy of the thruster. The real frequency, growth rate and amplitude of the oscillations depend on geometry, magnetic field profile, mass flow rate and discharge voltage. Ducrocq *et al*. [30] have studied high-frequency electron drift instability and derived three-dimensional dispersion relation. Keidar [31] has modeled plasma dynamics and ionization of the propellant gas within the anode holes. Barral and Makowski [32] have analyzed transit-time instability in Hall thruster. Kapulkin and Guelman [33] have investigated low frequency instability in near anode region of a Hall thruster. Lazurenko *et al*. [34] have reviewed high-frequency instabilities and anomalous electron transport in Hall thrusters. Researchers have investigated resistive instabilities in a Hall thruster and found that the plasma perturbations in the acceleration channel are unstable in the presence of collisions [13, 15, 17, 35–40]. Fernandez

et al. [41] did simulations for the growth of resistive instabilities in $\vec{E} \times \vec{B}$ plasma discharge. The plasma resistivity induces resistive instabilities (electrostatic and electromagnetic) [13, 15, 17] associated with azimuthal and axial directions and it was depicted that these instabilities have the highest level near the thruster exit plane. Smolyakov *et al.* reported that sheath instabilities has a vital role in anomalous transport phenomena in Hall plasma thruster [41]. Plasma sheath plays an important role to control the mobility of electrons inside a plasma channel [42–44].

Range (kHz)	Type	Driving mechanism
10–20	Loop or circuit oscillations	Magnetic field, discharge voltage and electron wall collision frequency [45]
5–25	Rotating spokes	Ionization process [46]
20–60	Drift instability	Gradient of density and magnetic field [47]
70–500	Ion transient time oscillations	Plasma density gradient and low ionization [11, 48]
0.5 to 5 MHz	Azimuthal waves	Drift velocity of plasma [11, 13, 17, 34].

8. Conclusions

The current status of electric propulsion for deep interplanetary missions has been reviewed. The basic working mechanism of electro-thermal, electrostatic and electromagnetic thruster is tabulated. Limitations and shortcomings of Hall thruster system have been discussed. The highlights of potential research are also given.

Acknowledgements

Author details

Sukhmander Singh[1*], Sanjeev Kumar[2], Shravan Kumar Meena[2] and Sujit Kumar Saini[2]

1 Department of Physics, Central University of Rajasthan, Ajmer, Kishangarh, India

2 Department of Physics, Motilal Nehru College University of Delhi, Delhi, India

*Address all correspondence to: sukhmandersingh@curaj.ac.in

IntechOpen

References

[1] Kaufman HR. (2012). Technology of closed-drift thrusters. AIAA J, Vol. 23, No.1, May 2012, 78–86, doi:10.2514/3.8874.

[2] O'Reilly D, Herdrich G, Kavanagh DF. Electric Propulsion Methods for Small Satellites: A Review. Aerospace. 2021; 8:1–30. Doi.org/10.3390/aerospace8010022

[3] Nawaz A, Albertoni R, Auweter-Kurtz M. Thrust efficiency optimization of the pulsed plasma thruster SIMP-LEX. Acta Astronaut. 2010;67:440–448. Doi.org/10.1016/j.actaastro.2010.03.006

[4] Beattie JRXIPS. Keeps Satellites on Track, The Industrial Physicist. Vol. 4. American Institute of Physics; 1998

[5] Potrivitu GC, Sun Y, Rohaizat MW, Cherkun O, Xu L, Huang S, et al. A Review of Low-Power Electric Propulsion Research at the Space Propulsion Centre Singapore. Aerospace. 2020 Jun;7(6):67

[6] Goebel DM, Katz I. Fundamentals of Electric Propulsion: Ion and Hall Thrusters. New York: Wiley; 2008

[7] Oland E, Kristiansen R, Nicklasson PJ. Combined chemical and electric thruster solution for attitude control. In 4th International Conference on Recent Advances in Space Technologies 2009 Jun 11 (pp. 627-631). IEEE.

[8] Jahn RG. Physics of Electric Propulsion. New York: McGraw-Hill; 1968

[9] Martinez-Sanchez M, Pollard J E. Spacecraft electric propulsion: An overview. Journal Propulsion Power. 1998; 14(5), Sept.-Oct, 688–699.

[10] Levchenko I, Xu S, Mazouffre S, Lev D, Pedrini D, Goebel D, et al. Perspectives, frontiers, and new horizons for plasma-based space electric propulsion. Physics of Plasmas. 2020; Feb 3;27(2):020601

[11] Choueiri EY. Plasma oscillations in Hall thrusters. Physics of Plasmas. 2001; 8:1411-1426. DOI: 10.1063/1.1354644

[12] Ahedo E. Plasmas for space propulsion. Plasma Physics and Controlled Fusion. 2011;53(12):124037. DOI: 10.1088/0741-3335/53/12/124037

[13] Singh S, Malik HK, Nishida Y. High frequency electromagnetic resistive instability in a Hall thruster under the effect of ionization. Physics of Plasmas. 2013;102109(1–7):20

[14] Ling WY, Zhang S, Fu H, Huang M, Quansah J, Liu X, et al. A brief review of alternative propellants and requirements for pulsed plasma thrusters in micropropulsion applications. Chinese Journal of Aeronautics. 2020;33:2999-3010

[15] Singh S, Malik HK. Growth of low frequency electrostatic and electromagnetic instabilities in a Hall thruster. IEEE Transactions on Plasma Science. 2011;39:1910-1918

[16] Levchenko I, Xu S, Teel G, Mariotti D, Walker ML, Keidar M. Recent progress and perspectives of space electric propulsion systems based on smart nanomaterials. Nature communications. 2018;9:1-9

[17] Singh S, Malik HK. Resistive instabilities in a Hall thruster under the presence of collisions and thermal motion of electrons. The Open Plasma Physics Journal. 2011;4:16-23

[18] Rovey JL, Lyne CT, Mundahl AJ, Rasmont N, Glascock MS, Wainwright MJ, et al. Review of multimode space propulsion. Progress

in Aerospace Sciences. 2020;**100627**(1–27):118

[19] Brown NP, Walker ML. Review of plasma-induced hall thruster erosion. Applied Sciences. 2020 Jan;10(11):3775 (1–18).

[20] Zhurin VV, Kaufman HR, Robinson RS. Physics of closed drift thrusters. Plasma Sources Science and Technology. 1999;**8**:R1-R20

[21] Garrigues L, Hagelaar GJ, Bareilles J, Boniface C, Boeuf JP. Model study of the influence of the magnetic field configuration on the performance and lifetime of a Hall thruster. Physics of Plasmas. 2003;**10**:4886-4892

[22] Dorf L, Raitses Y, Fisch NJ, Semenov V. Effect of anode dielectric coating on Hall thruster operation. Applied Physics Letters. 2004;**84**: 1070-1072

[23] Barral S, Miedzik J. Numerical investigation of closed-loop control for Hall accelerators. Journal of Applied Physics. 2011;**013302**(1–10):109

[24] Tahara H, Imanaka K, Yuge S. Effects of channel wall material on thrust performance and plasma characteristics of Hall-effect thrusters. Vacuum. 2006;**80**:1216-1222

[25] Ahedo E, Escobar D. Influence of design and operation parameters on Hall thruster performances. Journal of applied physics. 2004;**96**:983-992

[26] Akshabov N, Burgasov MP, Veselovzorov AN. Soviet journal of plasma. physics. 1981;**7**:125

[27] Keidar M, Gallimore AD, Raitses Y, Boyd ID. On the potential distribution in Hall thrusters. Applied Physics Letters. 2004;**85**:2481-2483

[28] Fruchtman A, Cohen-Zur A. Plasma lens and plume divergence in the Hall thruster. Applied physics letters. 2006; 89:111501. Doi.org/10.1063/1.2349827

[29] Keidar M, Boyd ID. Effect of a magnetic field on the plasma plume from Hall thrusters. Journal of Applied Physics. 1999;86:4786–4791. Doi.org/ 10.1063/1.371444

[30] Ducrocq A, Adam JC, Héron A, Laval G. High-frequency electron drift instability in the cross-field configuration of Hall thrusters. Physics of Plasmas. 2006;13:102111(1–8). Doi. org/10.1063/1.2359718

[31] Keidar M. Anodic plasma in Hall thrusters. Journal of Applied Physics. 2008;103:053309(1–5). Doi.org/ 10.1063/1.2844495

[32] Barral S, Makowski K, Peradzyński Z, Dudeck M. Transit-time instability in Hall thrusters. Physics of Plasmas. 2005;**12**:073504 Doi.org/ 10.1063/1.1947796

[33] Kapulkin A, Guelman MM. Low-frequency instability in near-anode region of Hall thruster. IEEE transactions on plasma science. 2008;36: 2082–2087. Doi.org/10.1109/ TPS.2008.2003359

[34] Lazurenko A, Krasnoselskikh V, Bouchoule A. Experimental insights into high-frequency instabilities and related anomalous electron transport in Hall thrusters. IEEE transactions on plasma science. 2008;36:1977–1988. Doi.org/ 10.1109/TPS.2008.2000972

[35] Tyagi J, Singh S, Malik HK, Effect of dust on tilted electrostatic resistive instability in a Hall thruster. Journal of Theoretical and Applied Physics. 2018; 12: 39–43. Doi.org/10.1007/s40094-018-0278-z

[36] Malik HK, Singh S. Resistive instability in a Hall plasma discharge under ionization effect. Physics of Plasmas. 2013;**052115**(1–8):20

[37] Singh S. Evolutions of Growing Waves in Complex Plasma Medium. IntechOpen, London, United Kingdom, Nov: In edited book Engineering Fluid Mechanics; 2020

[38] Singh S. Waves and Instabilities in E X B Dusty Plasma. In: the edited book Thermophysical Properties of Complex Materials. IntechOpen, London, United Kingdom, December 12th. 2019

[39] Singh S. Dynamics of Rayleigh-Taylor Instability in Plasma Fluids. In: the edited book Engineering Fluid Mechanics. IntechOpen, London, United Kingdom, April 15th. 2020

[40] Singh S. Hall Thruster: An Electric Propulsion through Plasmas. In: the edited book Plasma Science IntechOpen, London, United Kingdom, March 2nd. 2020

[41] Fernandez E, Scharfe MK, Thomas CA, Gascon N, Cappelli MA. Growth of resistive instabilities in E$\times$ B plasma discharge simulations. Physics of Plasmas. 2008;15:012102(1–10). Doi. org/10.1063/1.2823033

[42] Alvarez-Laguna A, Magin T, Massot M, Bourdon A, Chabert P. Plasma-sheath transition in multi-fluid models with inertial terms under low pressure conditions: Comparison with the classical and kinetic theory. Plasma Sources Science and Technology. 2020; **29**:025003

[43] Mandal D, Elskens Y, Lemoine N, Doveil F. Cross-field chaotic transport of electrons by E$\times$B electron drift instability in Hall thruster. Physics of Plasmas. 2020;**27**:032301

[44] Smolyakov A, Zintel T, Couedel L, Sydorenko D, Umnov A, Sorokina E, et al. Anomalous electron transport in one-dimensional electron cyclotron drift turbulence. Plasma Physics Reports. 2020;**46**:496-505

[45] Tilinin GN. High-frequency plasma waves in a Hall accelerator with an extended acceleration zone. Soviet Physics Technical Physics. 1977;**22**: 974-978

[46] Chesta E, Lam CM, Meezan NB, Schmidt DP, Cappelli MA. A characterization of plasma fluctuations within a Hall discharge. IEEE transactions on plasma science. 2001;**29**: 582-591

[47] Frias W, Smolyakov AI, Kaganovich ID, Raitses Y. Long wavelength gradient drift instability in Hall plasma devices. I. Fluid theory. Physics of Plasmas. 2012;**19**:072112

[48] Morozov AI, Savelyev VV. Fundamentals of stationary plasma thruster theory. Reviews of plasma physics. 2000:203-391

Chapter 5

Estimation of Cumulative Noise Reduction at Certification Points for Supersonic Civil Aeroplane Using the Programmed Thrust Management at Take-off and Approach

Artur Mirzoyan and Iurii Khaletskii

Abstract

The reduction of the cumulative noise level at certification points applying to the supersonic civil aeroplane is estimated in the paper. The reduction is obtained by using an programmed thrust management with Programmed Lapse Rate based on the variation of engine power setting at take-off and approach. The use of proposed programmed reduced noise thrust management requires a change of the conventional noise certification procedures as well as further implementation as fully automated system (Variable Noise Reduction System) into aircraft/engine control system. The main engine noise sources such as the fan and exhaust jet are taken into account in the estimation. It is shown that the cumulative noise level using proposed programmed thrust management is lower by 10.7–12.2 EPNdB than using the conventional engine thrust control as currently applied to subsonic jet aeroplanes at take-off and approach.

Keywords: supersonic civil aeroplane, take-off and approach, engine thrust (power) setting, throttle ratio, bypass ratio, noise certification reference points

1. Introduction

The crucial issue of development of a new generation of supersonic civil aeroplanes (SCA) is to meet environmental requirements like sonic boom level, community noise level during landing and take-off cycle (LTO) and engine/CO_2 emission levels. According to the requirements of Chapter 12 of the current ICAO noise standard, maximal SCA noise levels at certification reference points (RP) should be satisfied the noise limitations for subsonic jet aeroplane at the same maximum certificated take-off mass (MTOM), i.e. to the current requirements of Chapter 14, Annex 16, Volume I [1].

The SCA design features leads to the generation more intense noise during the LTO cycle vs. the noise of the subsonic jet aeroplane with the same MTOM. The estimations of the noise levels applied to advance SCA shown that it is still

impossible to meet the requirements at the current level of aviation technologies. The CAEP (Committee on Aviation Environmental Protection) has not yet developed the new standard for SCA noise at RP.

The lack of an international standard for SCA noise and the expectation of the implementation of several USA SCA projects in the current decade motivated the USA Federal Aviation Administration (FAA) to develop national standards. In March 2020, FAA published a preliminary version of the national noise standards for a distinct SCA class. The limit line of USA noise standards locates exactly in the middle between the Chapter 4 and Chapter 14 of the ICAO standard for subsonic jet aeroplanes [2]. The SCA class is limited by the MTOM value of 68 000 kg and by the cruise speed corresponding to the Mach number of 1.8.

NASA and other research centers assessments showed that meeting the FAA's published limits on the SCA noise level, and even more so meeting the requirements of Chapter 14, Annex 16, Volume I, may not be satisfied on the current technology level [3, 4].

The FAA rules also suggest the some changes to the existing noise certification reference procedures applied to the subsonic jet aeroplanes. It is specifically stipulated that the SCA noise certification will use of technical equipment (like Variable Noise Reduction System) that will implement new approaches to the SCA community noise reduction. The capability for SCA noise management during LTO cycle using the engine thrust variation providing engine automatic (programmed) thrust/power throttling was considered in the number of publications [3–8]. The aim of the studies was to assess the maximal SCA community noise reduction using the thrust management at LTO cycle.

2. Problem statement

The take-off thrust (power) throttling has a contradictory effect on the noise levels in each take-off RP, i.e. on the lateral and flyover (cutback) noise levels. On the one hand, the lateral noise level is reduced due to a decrease of the engine exhaust jet velocity as well as fan circumferential velocity. On the other hand, the flyover noise level is increased due to the lower thrust settings are associated with the lower climb path, and therefore the distance from the community noise source to the take-off RP is decreased. Thus, a compromise solution on the engine thrust management (TM) during the take-off is required to reduce the take-off (lateral plus flyover) noise level.

In accordance with the noise certification procedure, the approach noise level is measured at approach using the constant flight speed along the path and the fixed glide slope angle θ which is equal to -3° [1].

To provide the flight along such path with the constant flight speed and glide slope angle, it is necessary to maintain a certain level of the engine thrust (power setting). The level of the thrust will be uniquely determined by the values of the specified flight speed and glide slope angle. In other words, if an aeroplane is flying along glide slope at a constant speed, there is a direct relationship between the levels of the required engine thrust and the glide slope angle.

The approach RP is determined by the point on the ground, on the extended center line of the runway at the distance L_{app} = 2000 m from the threshold. Therefore, the approach noise level at varying the glide slope angle θ will mainly depend on the 2 factors: the flight altitude above the approach RP and the change of the engine parameters associated with a change in the required engine thrust (i.e. approach power setting).

Therefore, the variation of the approach power setting leading to a change of the glide angle is considered in the paper as a measure of the reduction of the approach noise level.

The paper presents the results of a computational study of the acoustic efficiency of using the programmed reduced cumulative (sum of the lateral, flyover and approach noise levels) noise thrust management with so-called Programmed Lapse Rate (PLR) during the take-off as well as the approach. The approach provides the reduction of the cumulative community noise taking into account the fan and exhaust jet noise.

It is well known that the current ICAO standard, Chapter 14, imposes more stringent requirements for the subsonic jet aeroplane than the previous Chapters 3 and 4 [1]. The intention of the SCA designers to follow the global trend of reducing the impact of aviation on the environment pushes them to consider the propulsion systems based on the turbofan with higher bypass ratio (BPR).

At the same time, there is a cardinal redistribution of the contributions between engine noise sources as increasing BPR. The dominance of the jet noise for the turbofan with lower BPR (~ 0.5...1.5) is replaced with an approximate equality of the fan and jet contributions for the turbofan with mediate BPR (~ 2.5...3.5) and then with predominant fan noise for the turbofan with higher BPR (~ 4.0...5.0).

The comparison of the effective perceived noise levels in case of use of the reference and the proposed programmed reduced cumulative noise thrust management using PLR (from here on programmed TM) is carried out as applied to a notional twin-engine supersonic business jet (SBJ). The SBJ has the range L = 7400 km, seating capacity n = 8 pax and balanced field length BFL = 2000 m.

The considered SBJ propulsion system is based on the turbofan with BPR = 2.5 ... 5.0. The values of the range L, the seating capacity n and the balanced field length BFL are kept constant under the BPR variation. The take-off thrust loading is defined under provision of the specified balanced field length value.

The turbofan with BPR up to 5.0 is considered to maximize the SBJ noise reduction. At the same time, it is obvious that it is necessary to find a compromise solution, accounting the contradictory factors like nacelle size/drag, which is increased with increasing BPR.

3. Mission performance assessment for the SBJ at fixed flight range and using of turbofan with different BPR

The calculation of mission performance is performed for the SBJ with fixed flight range taking into account the flight segments like take-off, initial climb, climb, supersonic cruise, descent, approach, landing, and NBAA alternate. The engine size (and the corresponding SLS thrust and the take-off thrust loading) is defined from the balanced take-off condition and the given balanced field length BFL = 2000 m. At the definition of balanced field length the minimal one engine inoperative climb gradient at the altitude of 10.7 m is considered as the constraint [5].

Keeping the specified values of the flight range L, the seating capacity n and the balanced field length BFL with an increase of BPR leads to an increase of the maximum certificated take-off mass MTOM. It is primarily happened due to an increase of the required engine take-off thrust FN_{to} and propulsion system mass W_{ps}.

The **Figures 1** and **2** show the changes of MTOM (**Figure 1**), relative take-off thrust FNto_rel and propulsion system mass Wps_rel (**Figure 2**) depending on the BPR.
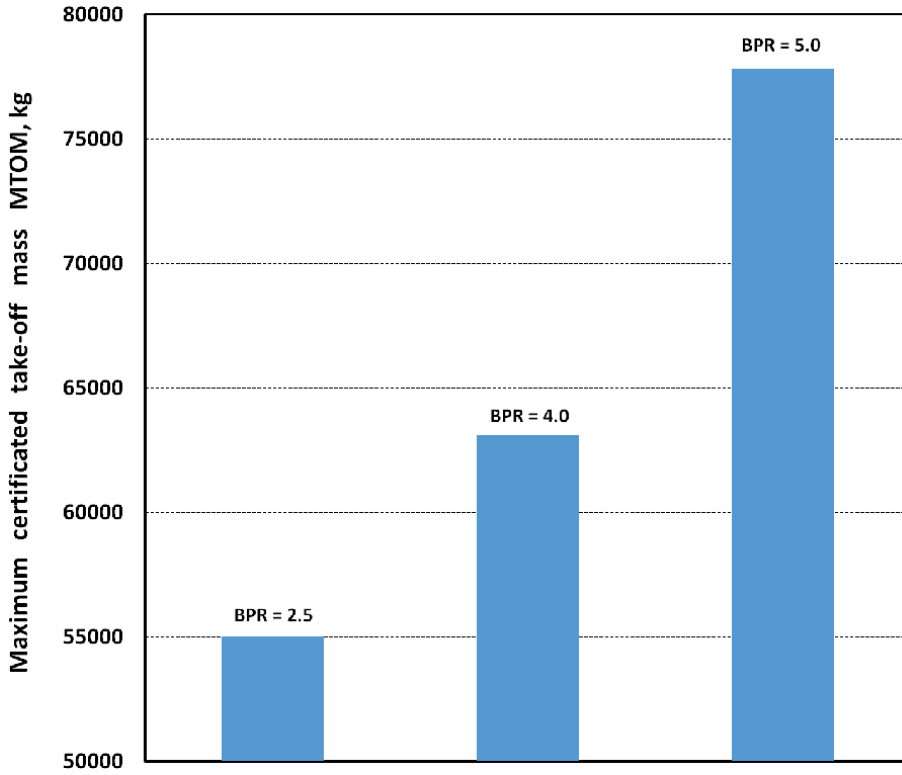
Figure 1.
The change of maximum certificated take-off mass MTOM vs. engine bypass ratio BPR (L = 7400 km, n = 8 pax, BFL = 2000 m).
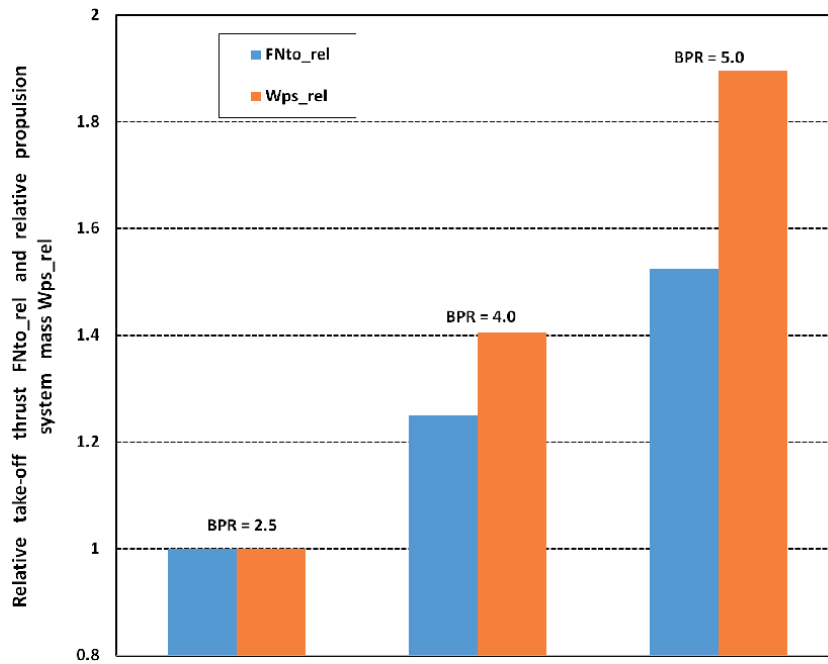
Figure 2.
The changes of FNto_rel and Wps_rel vs. bypass ratio BPR (L = 7400 km, n = 8 pax, BFL = 2000 m).

The relative values of the take-off thrust FNto_rel and the propulsion system mass Wps_rel are equal to:

$$FNto\_rel = FN_{to} / FN_{toBPR=2.5}, Wps\_rel = W_{ps} / W_{psBPR=2.5}. \qquad (1)$$

where FN_{to}, $FN_{to\,BPR\,=\,2.5}$, W_{ps} and $W_{ps\,BPR\,=\,2.5}$ are the take-off thrust and propulsion system mass for the turbofan with current BPR and BPR = 2.5 correspondingly.

It can be seen that as BPR changes from 2.5 to 5.0 with fixed values of L, n and BFL, the take-off thrust FN_{to} and the propulsion system mass W_{ps} increase by 57 and 90%, respectively, while the MTOM increases from 55 000 to 77 000 kg, i.e. on 40%.

A noticeable increase of the MTOM at highest BPR may lead to an increase of the direct operating cost, which could be economically unacceptable. Therefore, the cost efficiency of use of turbofan with the higher BPR should be evaluated in the future activities more detail.

4. The reference and programmed reduced cumulative noise thrust management at take-off and approach

4.1 Take-off

Conventional TM applied to subsonic jet aeroplanes at take-off is considered as reference TM during the take-off. It includes the take-off and cutback power settings.

The proposed programmed TM using the PLR includes 7 flight path segments: take-off power (segment 1), throttling to power setting providing reduced lateral noise (segment 2), power setting providing reduced lateral noise (segment 3), restoring maximum climb power setting (segment 4), maximum climb power setting (segment 5), throttling to power setting providing reduced flyover noise (segment 6) and power setting providing reduced flyover noise (segment 7).

The throttle ratio value TR is equal to TR = thrust/full thrust,

where thrust corresponds to the thrust value for the current power setting;

full thrust corresponds to the thrust value for the maximum power setting at the current flight conditions.

The **Figure 3** shows the changes of the take-off thrust throttle ratio TRto depending on the distance from the brake release point and used take-off TM applied to SCA with MTOM of 55 000 kg and turbofan with BPR = 2.5.

The main purposes of the flight path segments are following:

- reduction of the required balanced field length (segment 1);

- reduction of the lateral noise level (segments 2 and 3);

- increase of the flight altitudes over the flyover RP (segments 4 and 5);

- reduction of the flyover noise level (segments 6 and 7).

The power settings on the segments 3 and 7 correspond to the lower power settings, providing the lateral and flyover noise reduction accounting the airworthiness and noise certification procedure restrictions in term of the minimal climb gradients [6].
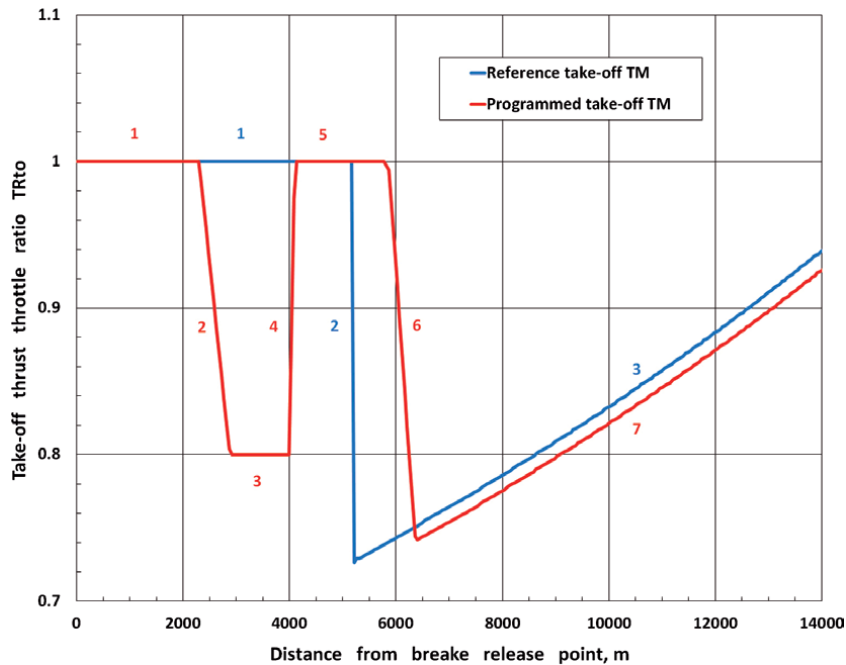
Figure 3.
The change of the take-off thrust throttle ratio TRto depending on the distance from the brake release point for reference and programmed take-off TM.

The proposed programmed TM includes rational choice of the TM parameters like the location of the beginning and end points of the segment 3, the beginning point of the segment 7, the thrust throttle ratio on the segments 3 and 7, the thrust acceleration and throttling rates on the segments 2, 4 and 6 (see **Figure 3**). All parameters are optimized in the paper under the minimum take-off noise criteria.

As seen in the **Figure 3**, the optimal take-off throttle ratio TRto values for the segment 3 and in beginning point of the segment 7 are equal to 0.8 (i.e. the engine power should be reduced by 20% vs. maximum power setting) and 0.74 (i.e. the engine power should be reduced by 26%) accordingly. The optimal distances for location of the beginning and end points of the segment 3 and the beginning point of the segment 7 should be equal to 2300, 4000 and 5800 m respectively. The optimal take-off thrust throttling rates on the segments 2 and 6 should be equal to 15 and 2.5% of thrust per a minute.

The **Figure 4** shows the SBJ flight path for the turbofan with BPR = 2.5 using the reference and programmed take-off TM.

Despite the fact that the use of programmed TM leads to a lower initial climb trajectory (see **Figure 4**), it is possible to recover the altitude above the flyover RP. It is mainly obtained due to the optimal choice of the programmed TM parameters, impacted on the flight above RP.
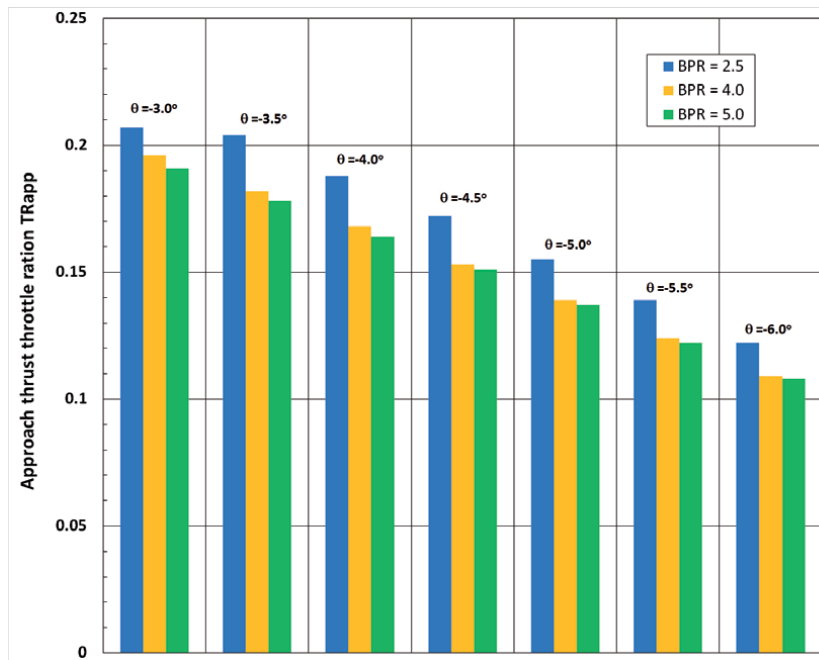
4.2 Approach

The conventional TM applied to the subsonic jet aeroplanes at approach providing the approach flight path with the glide slope angle $\theta = -3°$ is considered as the reference approach TM. It usually includes use of the engine power setting close or equal to the flight idle.

The proposed programmed approach TM includes the use of the engine power setting lower than the flight idle.
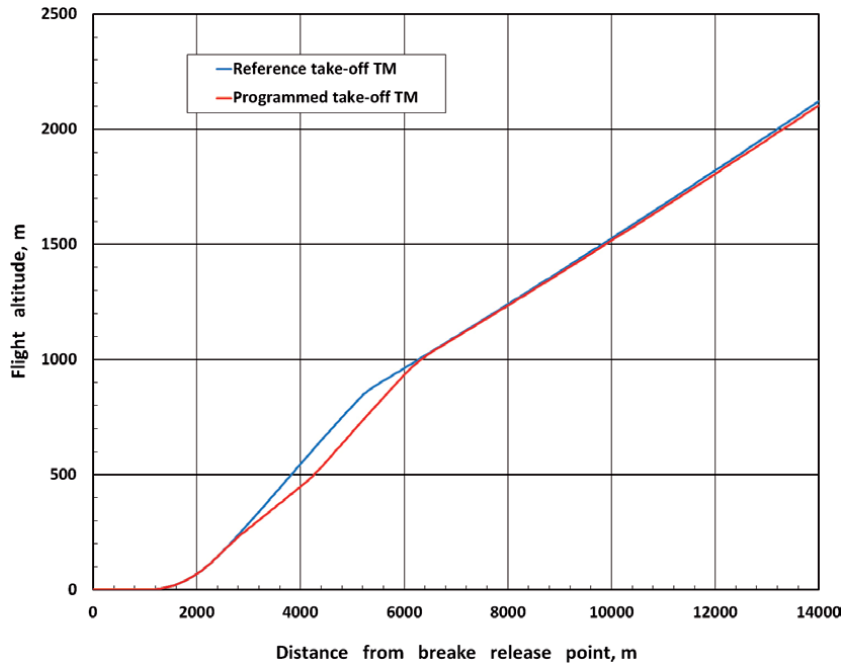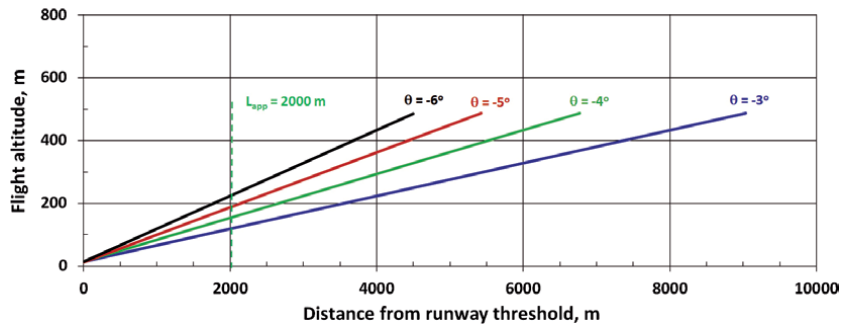
Figure 4.
The SBJ take-off SBJ flight path for turbofan with bypass ratio BPR = 2.5 using reference (green line) and programmed (red line) take-off TM.

Figure 5.
The change of approach thrust throttle ratio TRapp depending on the glide slope angle θ and bypass ratio BPR for the reference (at θ = −3°) and programmed (at θ higher than -3°) approach TM.

Figure 5 shows the change of approach thrust throttle ratio TRapp depending on the glide slope angle θ and engine BPR.

It can be seen that with an increase in the angle θ from −3 to-6°, the approach throttle ratio TRapp decreases from 0.2 to 0.11–0.12. At the same time, a change

Figure 6.
The SBJ approach flight paths with the different glide slope angles θ for and turbofan with bypass ratio BPR = 2.5.

of BPR in the range from 2.5 to 5.0 practically does not affect the change of the engine power setting.

On the **Figure 6** SCA approach paths with different glide slope angle θ are presented for turbofan with BPR = 2.5. Changing the engine power setting and θ leads to an increase of the flight altitudes above the approach RP, located at a distance of 2000 m from the runway threshold.

The flight altitudes above the approach RP does not change with a change of BPR. And at the same time it significantly increases (by about 100 m) with an increase of the angle θ from −3 to -6° (**Figure 6**).

5. Comparison of SCA noise benefit at using reference and programmed TM

The **Figure 7** shows the comparative acoustic efficiency of using the programmed take-off TM vs. reference take-off TM. Changes of the flyover noise in case of replace of reference with programmed take-off TM does not exceed 1 EPNdB that is associated with the same flight conditions above the flyover RP (see **Figure 4**).

The changes of the lateral noise level are equal to 2.6 to 6.1 EPNdB depending on BPR.

The increase of the noise reduction benefit as increasing BPR is connected with increasing the contribution of fan noise to the total engine noise as well as increasing the influence of engine throttling in the fan noise. As a result, the change of the take-off (lateral plus flyover) noise level using programmed take-off TM instead of the reference take-off TM is equal to 2.3...6.0 EPNdB, depending on the BPR.

The **Figure 8** shows the change of SBJ approach noise level deviation from the approach noise in case of using turbofan with BPR = 2.5 and angle θ = −3.0° depending on BPR.

The changes of the approach noise level in case of replace of reference with programmed approach TM may reach up to 8 EPNdB depending on glide slope angle θ.

The assessment shown the potential effectiveness of a programmed approach TM, which reduces the approach noise level due to higher glide slope angle and flight altitudes above the approach RP.

The use of higher glide slope angle may lead to a more complex approach and landing procedures and requires the mandatory use of an instrumental automatic landing system, which is currently applied to many subsonic jet aeroplanes.
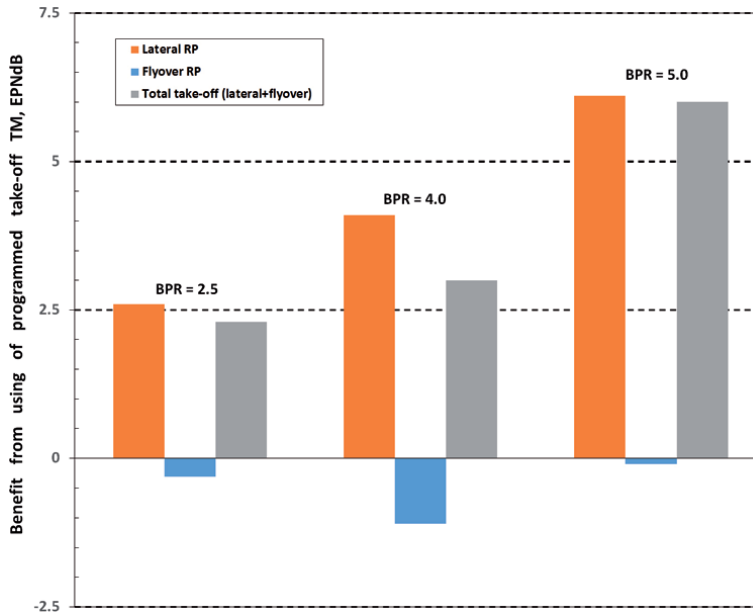
Figure 7.
The benefit of SCA lateral, flyover and total take-off (lateral plus flyover) noise levels from the use of programmed take-off TM depending on the engine bypass ratio BPR.
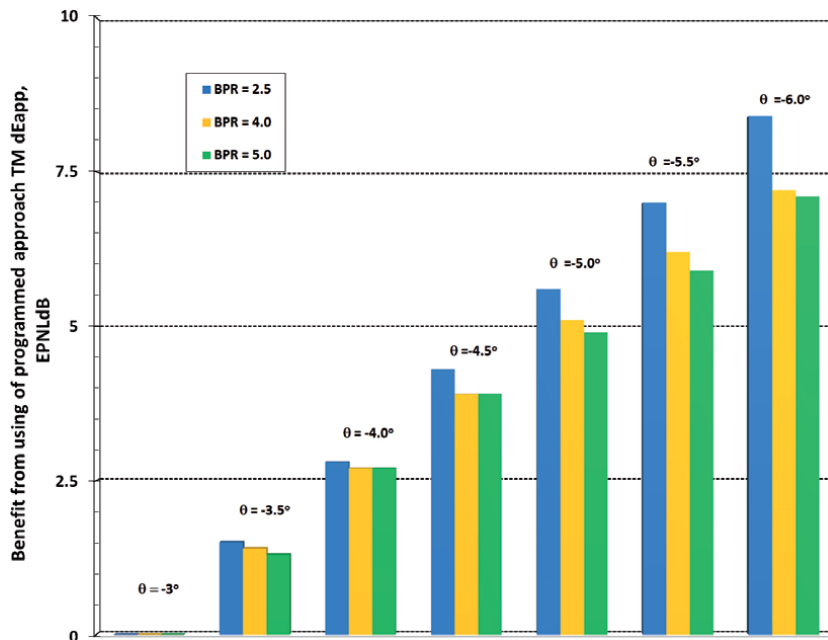
Figure 8.
The benefit of SCA approach noise levels from the use of programmed approach TM depending on the glide slope angle θ and the engine bypass ratio BPR.

6. Conclusions

In connection with the development of a new version of the ICAO international standard for the noise levels of SCA at certification points during the LTO cycle and the

introduction of the USA national standard, it becomes relevant to study new opportunities to reduce the noise for such type of aircraft. The use of programmed thrust management (control) at the LTO cycle is evaluated in the paper as a tool for reducing the SCA noise levels. A comparative assessment of effective perceived noise levels in case of using the reference (conventional for subsonic jet aeroplanes) and programmed thrust management is applied to notional twin-engine supersonic business jet (with seating capacity of 8 pax, a range of 7 400 km, and the balanced field length of 2 000 m).

The following main results are obtained:

- the use of the proposed programmed take-off thrust management during the takeoff and initial climb instead of the reference one, reduces the take-off (lateral and flyover) noise level by 2.3–6.0 EPNdB depending on the bypass ratio BPR. It is mainly achieved by lateral noise reduction while flyover noise level is possible to keep unchanged;

- the use of the proposed programmed approach thrust management during the approach is associated with an increase of the glide slope angle due to additional thrust throttling. It is shown that an increase in the glide slope angle leads to reduction of approach noise. As the glide slope angle is changed from -3° to -6°, the SCA approach noise reduction may reach up to 8.4 EPNdB for turbofan with bypass ratio BPR of 2.5, and up to 6.2 EPNdB for turbofan with BPR of 5.0. It should be noted that increasing the glide slope angle relative to the standard value of -3° may lead to the more complex approach and landing procedures and requires the mandatory use of an instrumental automatic landing system, which is currently used on many subsonic jet aeroplanes;

- the use of the programmed thrust management at LTO cycle instead of reference thrust management (i.e. use of cutback around flyover certification point and approach with the with the glide slope angle of -3°) may reduce cumulative noise level by 10.7–12.2 EPNdB depending on bypass ratio BPR;

- as changing the bypass ratio BPR from 2.5 to 5.0 while maintaining the specified aircraft mission performance such as flight range, seating capacity and runway length the aircraft maximum take-off mass is increased from 55 to 77 tons, the take-off thrust and propulsion system mass are increased by 57% and 90% accordingly; a noticeable increase of the aircraft takeoff mass at highest bypass ratio BPR may lead to an increase of direct operating cost which could be economically unacceptable;

- programmed take-off thrust management using Programmed Lapse Rate should include the optimal location of two flight segments with lower power settings in the area of lateral and flyover reference points, optimal lower power settings, optimal thrust throttling rates as well as flight segment with maximal climb power setting between lateral and flyover reference points;

- the optimal values of the parameters of programmed take-off thrust management are following: thrust ratio in the area of lateral and flyover reference points are equal 0.8 (i.e. power reduction by 20%) and 0.74 (i.e. power reduction by 26%) respectively. The optimal distances for beginning and end of flight segment with power setting providing reduced lateral noise and for beginning of flight segment with power setting providing reduced flyover

noise are equal to 2300, 4000 and 5800 m respectively. The optimal thrust throttling rates for transition on the power settings providing reduced lateral and flyover noise are 15 and 2.5% of thrust per minute respectively.

The study of programmed thrust management should be continued in the direction of taking into account the effect of noise shielding by airframe elements and the application of acoustic liners in the propulsion system.

Acknowledgements

Conflict of interest

The authors declare that there is no conflict of interest regarding the publication of this work.

Nomenclature

Abbreviations

BPR	bypass ratio
EPNdB	Effective Perceived Noise level unit
LTO	Landing/Take-Off cycle
NBAA	National Business Aviation Association
PLR	Programmed Lapse Rate
RP	noise certification Reference Point(s)
SBJ	Supersonic Business Jet
SCA	Supersonic Civil Aeroplane(s)
TM	Thrust Management
VNRS	Variable Noise Reduction System

Symbols

BFL	balanced field length in m
FN	thrust in kN
L	flight range in km
m	meter
M	flight Mach number
MTOM	Maximum certified Take-Off Mass in tons
n	seating capacity
TR	Throttle Ratio
θ	glide slope angle in degree

Scripts

app	approach
ps	propulsion system
rel	relative
to	take-off

Author details

Artur Mirzoyan* and Iurii Khaletskii
Central Institute of Aviation Motors, Moscow, Russia

*Address all correspondence to: mirzoyan@ciam.ru

IntechOpen

References

[1] Annex 16 to the Convention on International Civil Aviation, Vol. I: Aircraft Noise, International Standards, and Recommended Practices-Environmental Protection, 7th ed., International Civil Aviation Organization, Montreal, July 2014.

[2] Noise Certification of Supersonic Airplanes: 14 CFR Parts 21 and 36: [Docket no.: FAA-2020-0316; Notice no. 20-06]: RIN 2120-AL29. Department of Transportation, Federal Aviation Administration. Federal Register. 2020. Vol. 85, no. 71 (April 13). p. 20431-20447.

[3] Berton J., Jones S., Seidel J., Huff D. Mint: Noise Predictions for a Supersonic Business Jet Using Advanced Take-Off Procedures. The Aeronautical Journal. 2018. DOI: 10.1017/aer.2018.6.

[4] Berton J., Jones S., Seidel J., Huff D. Advanced Noise Abatement Procedures for a Supersonic Business Jet . In: Proceedings of 23rd International Symposium on Air Breathing Engines (ISABE 2017): Economy, Efficiency and Environment, 3-8 September 2017, Manchester, UK, 2017, Bedfordshire, UK, ISABE, p. 477-489.

[5] Mirzoyan A. Studies on MDO of Engine Design Parameters with Mission, Noise and Emission Criteria at SSBJ Engine Conceptual Design. In: CD-ROM Proceedings of 26th International Congress of the Aeronautical Sciences (ICAS 2008) including the 8th AIAA Aviation Technology, Integration, and Operations (ATIO) Conference, 14-19 September 2008, Anchorage, Alaska, USA.

[6] Mirzoyan A., Stouflett B. Environmental Problems of the SSBJ Engine in the HISAC Project. Noise and Emission Potentialities of Optimal Takeoff Thrust Management for Twin Engine Low Boom SSBJ. ICAS 2009 Workshop "Aviation and Environment", 28 September 2009, Amsterdam, Netherland. Available from: http://icas.org/media/pdf/Workshops/2009/REF4.%20DASSAULT_HISAC_ICAS2009%20workshop.pdf [Accessed: 2021-01-30].

[7] Mirzoyan A., Khaletskii I. Potentialities of Noise Reduction Using Low Noise Takeoff Thrust Management for Advanced Supersonic Civil Aeroplanes. 22th CEAS-ASC Workshop "Future Aircraft Design and Noise Impact", 6-7 September 2018, Amsterdam, Netherland. Avalable from: https://www.nlr.org/wp-content/uploads/2018/09/CEAS-p11_Mirzoyan-Khaletskii-Potentialities-of-Noise-Reduction-Using-Low-Noise-Takeoff-Thrust-Management-for-Advanced-Supersonic-Civil-Aeroplanes.pdf [Accessed: 2021-01-30].

[8] Mirzoyan A., Khaletskii I. Take-off thrust and noise control for supersonic civil transport engines. AVIATION ENGINES Journal. ISSN 2658-6061. 2020. N2(7) (In Russian).

Chapter 6

Thrust Force Generated by Heaving Motion of a Plate: The Role of Vortex-Induced Force

Kazuo Matsuuchi

Abstract

To understand the force acting on birds, insects, and fish, we take heaving motion as a simple example. This motion might deviate from the real one. However, since the mechanism of force generation is the vortex shedding due to the motion of an object, the heaving motion is important for understanding the force generated by unsteady motion. The vortices released from the object are closely related to the motion characteristics. To understand the force acting on an object, information about momentum change is necessary. However, in vortex systems, it is impossible to estimate the usual momentum. Instead of the momentum, the "virtual momentum," or the impulse, is needed to generate the force. For calculating the virtual momentum, we traced all vortices over a whole period, which was carried out by using the vortex-element method. The force was then calculated based on the information on the vortices. We derived the thrust coefficient as a function of the ratio of the heaving to travelling velocity.

Keywords: heaving motion, virtual momentum, unsteady effect, extended Blasius formula, vortex street

1. Introduction

Motion of insects or birds is inherently unsteady. The creatures utilise the unsteadiness efficiently. For example, a coherent structure called the leading edge vortex (LEV) plays an essential role in the generation of unsteady force. Many authors have published studies on the topic and hilighted its importance, experimentally and numerically. The magnitude of the unsteady force cannot be explained by a steady-state approach. In many cases, the unsteadiness generates greater forces more efficiently than that in the steady state [1, 2]. Experiments have been conducted in three-dimensional space and numerical analyses have been carried out to understand the mechanism of force generation. These studies explained several aspects of unsteady phenomenon, but the role of vortices generated close to the object is still unclear. How does the behaviour of vortices affect the generation of force? In particular, how does momentum change depend on the force? We are not sure how to estimate the momentum of a vortex system, because the usual momentum has no definite value. Our aim is to establish a rule that governs the force generation by the momentum change. Characteristics such as the magnitude, the rotation direction, and the position are key to determining the momentum.

Unless we determine their properties, the evaluation of force cannot be made quantitatively.

When an object of a constant circulation Γ moves with a constant speed dx_0/dt, a fluid force acts perpendicular to the direction of motion. The magnitude is known to be $\rho(dx_0/dt)\Gamma$. It should be noted that the magnitude is the derivative of the virtual momentum $\rho x_0 \Gamma$ with respect to time, see [3], Art.157. Here, ρ is the density of fluid. This is a simplest application of a well-known law that governs the conservation of virtual momentum. In other words, this is a typical example of the second law of motion in the vortex motion. In general, the virtual momentum plays an essential role in the generation of force instead of the normal momentum. As illustrated above, in unsteady flows, the virtual momentum is important for the generation of force. We would like to illustrate the role of the virtual momentum by applying it to a heaving motion of a thin plate.

A lot of attention has been paid to the dependence of parameters characterising the unsteadiness known as the reduced frequency or the Strouhal number of the propulsive motion of insects, fish and humans (for example, [4–6]). Here, we also discuss the dependence of the reduced frequency on the thrust.

The heaving motion of a thin plate is the simplest and most suitable example of the analysis of unsteady phenomena. In addition, the heaving motion is solved in the limit as the heaving amplitude becomes smaller. For investigating the unsteady phenomenon, the vortex motion is a key concept. The analytical tool used here is not specific and can be extended to wider problems.

2. Direct effect of a heaving plate

First, we have a look at the relation between the force acting on a body fixed in a stream and the free vortices flowing behind it. It is known that a drag acts on a still body set in the stream. We can see two vortex rows here, called the Kármán vortex street (see **Figure 1(a)**).

We can also notice another similar vortex street behind the flying birds and the swimming fish. However, the direction of rotation of the vortices is inverse. In the case of the Kármán street, a momentum defect is observed while the momentum seems to increase behind the birds and fish. In the latter case, a thrust acts on the object to move forward due to the increase in momentum. As an example, we show the vortex street appearing in heaving motion (see **Figure 1(b)**). In pitching
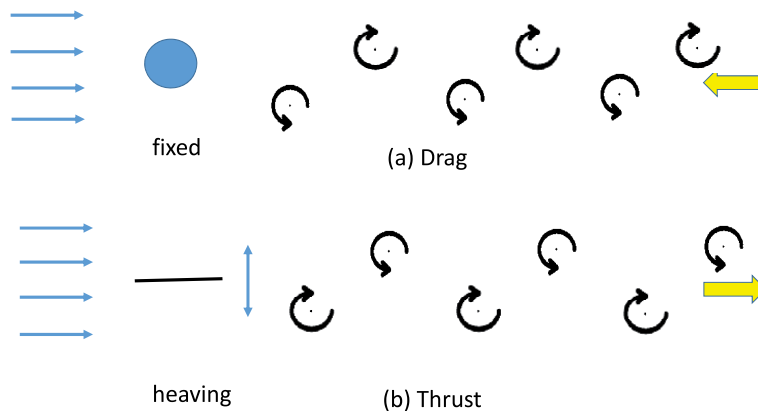
Figure 1.
Vortex street and an object in the stream. (a) an object fixed in the stream; (b) a thin aerofoil heaving vertically. Two thick arrows denote the direction of momentum increase.

motion, a similar street can be observed (see example, [7]). In general, those cases where backward momentum increases generate thrust acting against the flow. In the figure, the thick arrows denote the direction of the increased momentum.

To understand the mechanism of thrust generation we study the heaving motion of a thin plate in a uniform flow. We assume that the plate has a constant circulation Γ. Even in unsteady conditions, we assume that the fluid flows smoothly at the trailing edge according to Kutta's condition. The circulation Γ is determined by this smoothness condition. The velocity around the leading edge would diverge and hence the pressure may not be finite because the edge is a mathematical singular point.

To evaluate the force acting on an object, we usually integrate the pressure on the surface of the object. However, because a simple plate has two singular points at the leading and trailing edges. In particular, the estimation of the pressure at the leading edge is almost impossible when Kutta's condition is applied at the trailing edge. Instead of the integration of pressure, we apply Newton's second law of motion, which states that the force is a result of the momentum change. However, it is known that the estimation of momentum is almost impossible, and hence virtual momentum has to be used instead.

2.1 Effect of bound vortex

The coordinates system is shown in **Figure 2**. A thin aerofoil is located at $z = z_0(t)$ in the complex z-plane or at $z' = 0$. The coordinates z and z' are related by the equation

$$z'(t) = z - \mathrm{i} y_0(t). \tag{1}$$

Consider a uniform flow whose velocity is U in the x-direction and a bound vortex of a constant circulation Γ around the plate and no free vortices. The circulation is positive when the fluid rotates in the anticlockwise direction, while the vorticity is positive for vortices rotating in the clockwise direction. The force $X + \mathrm{i} Y$ acting on the object located at $z_0 (= x_0 + \mathrm{i} y_0)$ is given by:

$$X + \mathrm{i} Y = \mathrm{i} \rho \Gamma (\dot{z}_0 - \mathcal{U}) - 2\pi \rho a^2 \ddot{\bar{z}}_0 + 2\pi \rho a^2 \ddot{z}_0, \tag{2}$$

where the dot denotes the derivative with respect to time t [8]. Here, the length of the plate is $4a$ ($=L$) and located parallel to the uniform flow (see **Figure 2**).
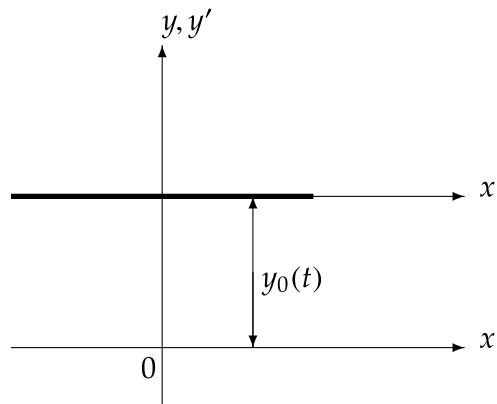
Figure 2.
Coordinates system. The heaving plate is located at $y = y_o$, $-2a \leq x' \leq 2a$.

Confining ourselves to the oscillation only in the y-direction, or $\dot{z}_0 = \mathrm{i}\dot{y}_0(t)$, the force can be:

$$X + \mathrm{i}Y = \mathrm{i}\rho\Gamma\left(\mathrm{i}\dot{y}_0 - \mathcal{U}\right) + 4\pi\mathrm{i}\rho a^2\ddot{y}_0. \tag{3}$$

For cases without any motion, the above equation is written simply as $Y = -\rho U\Gamma$, which corresponds to the lift known as the Kutta-Joukowski theorem.

The second term on the right-hand side indicates the drag defined as

$$m'\frac{\mathrm{d}^2 y_0(t)}{\mathrm{d}t^2}, \tag{4}$$

where m' is called the virtual mass. The direction of this force is parallel to the direction of motion. Accordingly, this force which acts in the y-direction cannot contribute to the propulsion. The virtual mass for this thin plate is expressed as $\pi\rho(L/2)^2(= m')$ (see [9], Art. 9.222, [10–12] for the general discussion). This force acting only in the y-direction is independent of vortex formation and shedding. The force is not related to thrust, and hence we will not discuss this force any more. Finally, from Eq.(3) the force in the x-direction is

$$X = -\rho\dot{y}_0\Gamma. \tag{5}$$

This formula corresponds to the Kutta-Joukowski theorem. When the object with the circulation Γ is located at $z = z_1$, the virtual momentum is expressed as $-\mathrm{i}\rho z_1\Gamma$.

Eq. (5) can be derived easily by considering the virtual momentum. For an object with a constant circulation Γ_1 located at the position z_1, the momentum, or more precisely the virtual momentum, P, of the flow is expressed as $-\mathrm{i}\rho z_1\Gamma_1$. When the vortex moves at the speed $\dot{z}_1$, the force F acts on it as a result of momentum change, i.e.,

$$F = -\frac{\mathrm{d}P}{\mathrm{d}t} = \mathrm{i}\rho\dot{z}_1\Gamma_1. \tag{6}$$

2.2 Effect of free vortex

Next, we proceed to discuss about the effect of free vortices on the force. The general rule for estimating the force, when the viscosity is negligible, is the Blasius formula, see [10]. Since the formula is valid only for steady flow conditions, it has to be extended to include the unsteady effect. The extended formula for the force (X, Y), as seen in, for example, [13], is given as

$$X - \mathrm{i}Y = \frac{\mathrm{i}\rho}{2}\oint_B \left(\frac{\mathrm{d}f}{\mathrm{d}z}\right)^2 \mathrm{d}z + \mathrm{i}\rho\oint_B \frac{\mathrm{d}\bar{f}}{\mathrm{d}t}\,\mathrm{d}\bar{z}, \tag{7}$$

where B denotes the path along the surface of an object in the anticlockwise direction. In the above equation, $f(z)$ is the complex potential defined by $f(z) = \phi(x,y) + \mathrm{i}\psi(x,y)$. Here ϕ and ψ are the velocity potential and the stream function, respectively. The bar denotes the complex conjugate. Thisin **Figure 10** formula expresses two typical types of forces. One is the virtual momentum (VM) component, and the other the direct-interaction (DI) component. VM acts due to the change in momentum and DI is the direct interaction of the vortices with the body, which becomes important when the vortex is near the object. We denote the two forces F_v for VM and F_d for DI to distinguish between them. Before we discuss the general case, we consider a simple one where one free vortex κ_1 exists at $z = z_1$. The forces for VM and DI are expressed as

$$\overline{F}_v = \frac{i\rho}{2} \oint_B \left(\frac{df}{dz}\right)^2 dz, \tag{8}$$

$$= 2\oint_{z_1} \frac{i\kappa_1}{z - z_1} \left[\frac{df}{dz}\right]_c dz, \tag{9}$$

where $[df/dz]_c$ means the convection velocity at $z = z_1$ by the vortex κ_1. On the other hand, the force for DI is estimated from

$$\overline{F}_d = i\rho \oint_B \overline{\frac{\partial f}{\partial t}} dz. \tag{10}$$

First, we consider Eq.(10). This force is dependent on the object form. To integrate it we map a plate in the z-plane to a circle of radius a in the ζ-plane as

$$z = G(\zeta) = \zeta + \frac{a^2}{\zeta}, \tag{11}$$

When a vortex is located at $z = z_1$, the integration can be carried out to give

$$\overline{F}_d = 2\pi i\rho \kappa_1 a^2 \left(\frac{1}{\zeta_1^2 - a^2} \frac{dz_1}{dt} + \frac{1}{\overline{\zeta}_1^{\,2} - a^2} \frac{d\overline{z}_1}{dt}\right), \tag{12}$$

where

$$z_1 = G(\zeta_1), \tag{13}$$

and the convection velocity,

$$\frac{dz_1}{dt} = \left[\frac{df}{dz}\right]_{z_1} = \left(1 - \frac{a^2}{\zeta_1^2}\right)\dot{\zeta}_1. \tag{14}$$

It is easy to see that the right-hand side of Eq.(12) is pure imaginary, because the right-hand side expresses the sum of a complex and its complex conjugate. This means that the force has only a y-component. Therefore, the component F_d is not related to the thrust. Hence, we will not discuss F_d anymore. Only the VM would contribute to the thrust force.

From Eq.(10), we have

$$\overline{F}_v = X_v - iY_v = 2\pi i\rho \kappa_1 \dot{\overline{z}}_1, \tag{15}$$

where $\dot{z}_1$ is the covection velocity of vortex κ_1. The above equation is to Eq.(6), because $2\pi\kappa_1 = -\Gamma_1$. To determine the convection velocity $\dot{z}_1$, we apply the conformal mapping Eq.(13) and trace the vortex in the ζ-plane and then calculate the velocity in the z-plane. The moving speed of vortex κ_1 in the z-plane is already given by Eq.(13). Hence, we have

$$\overline{F}_v = 2\pi i\rho \kappa_1 \left(1 - \frac{a^2}{\overline{\zeta}_1^{\,2}}\right)\dot{\overline{\zeta}}_1 \tag{16}$$

Formulas (5) and (15) are the main targets for the calculation of thrust.

2.3 Determination of positions and velocities of a vortex

Now, we discuss how to generate a vortex under our boundary condition. What determines the vorticity and its position? Consider a flat plate set parallel to the flow (see **Figure 2**). Even in unsteady motion, the flow is subject to the condition that the fluid flows smoothly at the trailing edge. In other words, Kutta's condition at the edge must be satisfied at all times. We consider the heaving motion whose velocity, perpendicular to the plate is expressed as

$$w_h(t) = W_T e^{i\nu t}. \tag{17}$$

In the above equation, ν is the radian frequency of the heaving motion, and W_T is the amplitude. Denoting the period of the oscillation as T, $T = 2\pi/\nu$.

Because the plate has a velocity in the y-direction at $t = 0$, Kutta's condition is not satisfied. To satisfy the condition we set a new vortex at $x = 2a + \Delta x$, and we determine the vorticity κ_1 of the vortex so as to satisfy the condition. As for setting the initial position, [14] serves as a useful reference. The condition for the flow leaving the trailing edge smoothly determines κ_1 uniquely. Later at $t = \Delta t$ the vortex κ_1 moves away and hence the flow does not satisfy Kutta's condition again. To avoid the undesirable flow, we set a new vortex κ_2 at the same position as the initial position of κ_1, i.e., at $x = 2a + \Delta x$. Kutta's condition fixes the value κ_2 uniquely. Similarly, the subsequent process determines sequentially $\kappa_i (i = 1, 2, \dots)$.

We proceed to the next step to discuss the problem of movement of vortices. A vortex moves by the other free vortices including the bound vortex and the uniform velocity. The induced velocity $w = u - iv$ at z by the vortex κ_c located at $z = z_c$ is written as:

$$u - iv = \frac{i\kappa_c}{z - z_c}.$$

Actual calculations were done in the ζ-plane with respect to all the vortices including those of the mirror image. The calculation step was carried out at every time for the step Δt. See [14] for the suitable relation between Δx and Δt.

2.4 Calculation results

In the calculations, we determine the physical variables by choosing $a = 1$, $\rho = 1$ and $U = 1$. In **Figure 3**, we show their positions and the direction of rotation for the case when $\nu = 0.5$ and $W_T = 0.5$ at $t = 19.8$. The symbol + denotes the vortices of the clockwise rotation and those of the triangle (in red) the anticlockwise one, respectively. It is seen that the vortices rotating in clockwise direction gather at some places in the negative y-plane, while those rotating in anticlockwise direction gather in the positive y-plane. **Figure 4** shows the positions at t=39.8. We can find three clusters of vortices of clockwise rotation at about x =7.5, 20, and 33, and three clusters of anticlockwise rotation at x =13, 27, and 37. The clusters of positive or negative vortices occur by the interaction of each vortex. At those positions, the vorticities concentrate and have a structure in a large scale. Nonlinearity is seen even for such low W_T (=0.5). Three clusters of vortices rotating in the clockwise direction are in the area for $y < 0$, while three clusters rotating in the anticlockwise direction are in the area for $y > 0$. This array of two vortex streets would generate the downward flow, which suggests that the momentum is generated in the positive x-direction. Momentum generation in the positive x-direction means the generation of thrust force, as will be explained later. The deviation of arrays from the ordered
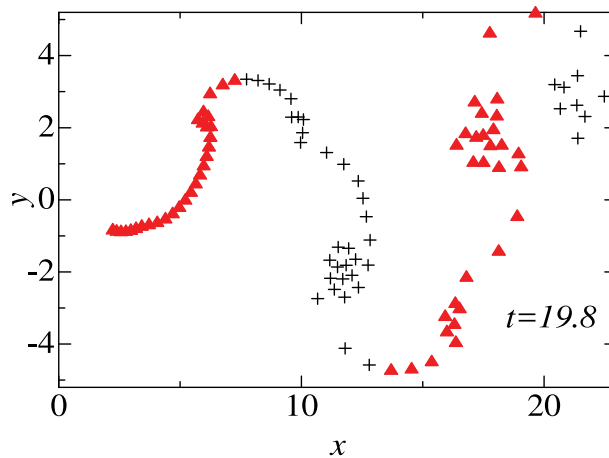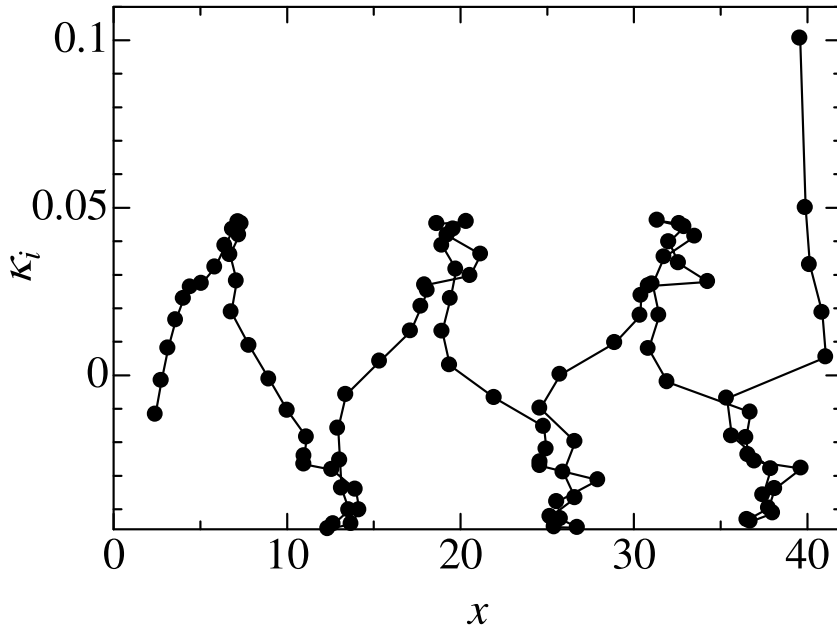
Figure 3.
Positions and the direction of rotation of vortices at t = 19.8 for the case of $W_T = 0.5$ and $\nu = 0.5$. Vortices of the positive sign generated in the initial stage gather near x = 12 and those of the negative sign near x=17.5. The symbol + stands for vortices rotating in the clockwise direction, while the triangle in red indicates vortices rotating in the anticlockwise direction.
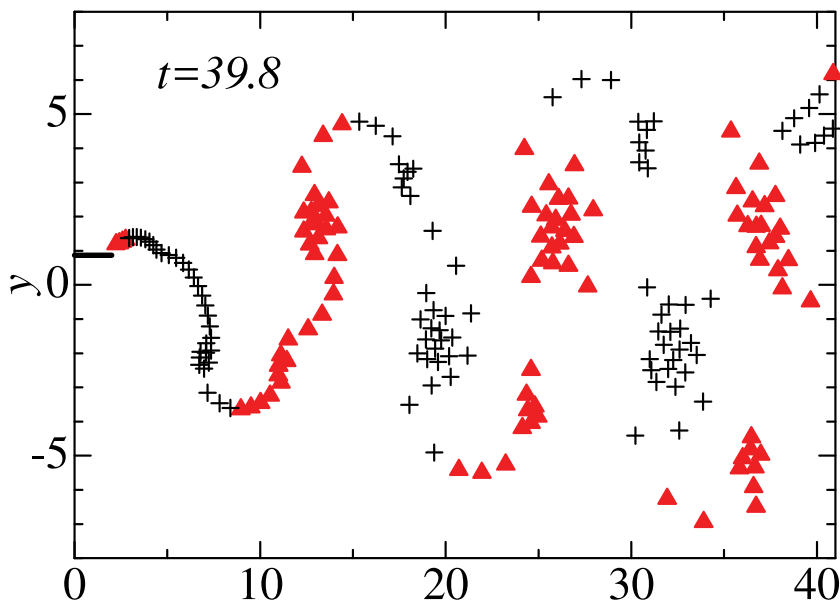
Figure 4.
Positions and the direction of rotation of vortices at t = 39.8 for $W_T = 0.5$ and $\nu = 0.5$. Some clusters of vortices rotating in the clockwise direction and those rotating in the anticlockwise direction appear.

ones is the result of nonlinearity. **Figure 4** also shows the deviation of sinusoidal distribution of vortices. Next, we consider the positions of vortices at initial stages near t=0. Those vortices generated initially, which are distributed near $x = 40$, fluctuate violently and move to the positive y-direction.

In **Figure 5**, the distribution of vortices κ_i determined in the manner explained earlier is depicted. This plot shows the complex distribution of vortices based on the interactions among many vortices. This may explain the reason why the clusters are generated.

Figure 5.
Distribution of the vorticity at t =39.8 when $W_T = 0.5$ and $\nu = 0.5$.

3. Calculation of force

In the following section, we describe calculations carried out when $U=\rho=a=1$ unless specified otherwise.

### 3.1 Direct force by movement of a plate with a circulation

According to Eq.(5), the movement in the y-direction of the plate with a circulation Γ_1 gives rise to the force X_b normal to it,

$$X_b = -\rho\Gamma_1\dot{y}_0. \tag{18}$$

We investigate the thrust generation due to the movement of a thin flat plate in more detail. When the motion is subjected to Eq.(17), we consider the force in the y-direction at the initial stage $t \approx 0$. Vortices rotating in the positive direction appear under the lower place near the trailing edge. Similarly, in the ζ-plane, the mirror images of the vortices rotating in the anticlockwise appear in a circle with radius a. In these, circumstances the circulation Γ around the circle is positive. In this case the force acts in the negative x-direction, because the sign of X_b is negative from Eq.(18).

The case where two free vortices are outside the circle is shown in **Figure 6**. For more than a vortex in the flow field there must be mirror images whose sign is opposite to the free vortices. In general, at time t, many vortices of the same number of free vortices exist inside the circle.

When n vortices are released, the intensity of the vortices is expressed as a sum $\sum_{i=1}^{n}\kappa_i$. At the same time, the sum of vortices within the circle of the radius a determines the circulation Γ of the bound vortex. The circulation of the bound vortex is expressed as
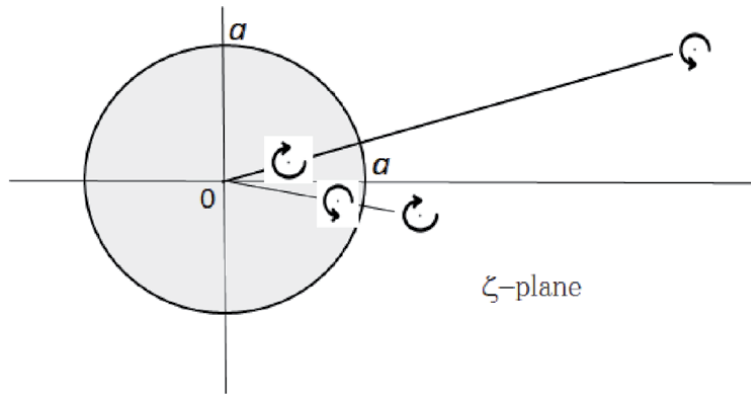
Figure 6.
A simple case where two free vortices κ_1 and κ_2 are released is illustrated in the ζ-plane. Two vortices of the opposite signs exist in the circle in the ζ-plane. The circulation Γ around the circle is the sum of two vorticities, $2\pi(\kappa_1+\kappa_2)$.

$$\Gamma = \sum_{i=1}^{n} 2\pi\kappa_i. \tag{19}$$

Using this circulation, we try to evaluate the force generated by the heaving motion. In Eq.(18) by changing Γ_1 by Γ, we have the force,

$$X_b(t) = -\rho\Gamma\frac{dy_0}{dt}, \tag{20}$$

The variation of X_b calculated by using the above equation is shown in **Figure 7** as a function of nondimensional time $\tau = t/(2a/U)$. The variation of the heaving velocity $w_h(\tau)$ of the plate (Eq.(17) is also plotted there). Let us consider the initial stage when the plate moves upward. Vortices generated by the upward movement are rotating in the clockwise direction, as shown in **Figures 4** or **5**. At the initial stage, mirror images inside the circle of the radius a rotate in the anticlockwise direction. In other words, the plate has a positive circulation. Because the velocity w_h is initially positive, the force X_b is negative from Eq.(20). The force acts against the main flow, i.e., the plate is pulled by the fluid in the negative x-direction. Usually, the upward motion connects with positive circulation, and hence the force becomes almost negative. On the contrary, negative circulation occurs when the motion is downwards. As a result, the sign of X_b has a negative value in the mean. The average value $X_{b(av)}$ is -0.240. The index (av) stands for the mean over two periods of oscillation. It should be noted that when the absolute velocity of the plate $|w_h|$ is the maximum, the force becomes maximum. This means that during the generation of strong vortices, the pressure at the edge becomes large. Strictly speaking, slight time delay is also observed. This may be because of the effect of the convection due to other free vortices.

The right-hand side of Eq.(20) expresses the differentiation of the virtual momentum $\rho\Gamma y_0$ with respect to time, if the circulation could be independent of time. It might be the incorrect estimation of the force. The right-hand side of Eq. (19) expresses the summation of all vortices and each vorticity is independent of time. However, because the number of vortices changes with time, the circulation Γ should be considered to be time-dependent. The dependence of time on the
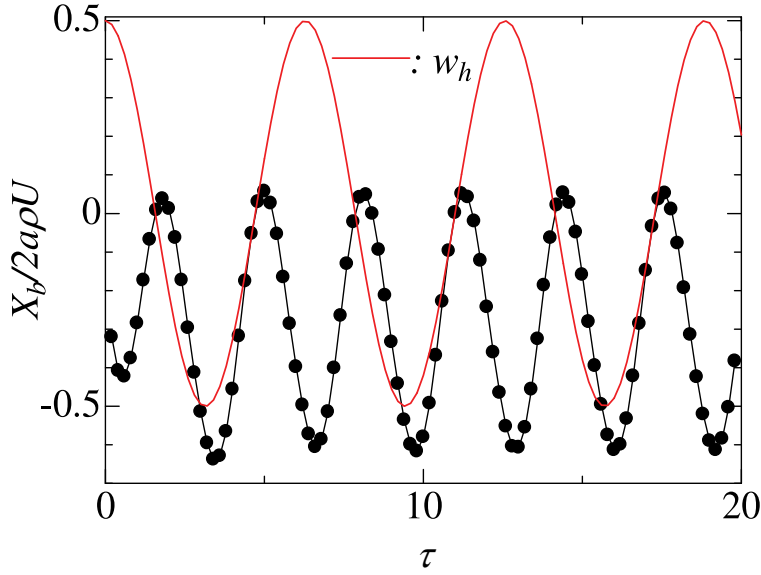
Figure 7.
The variation of force by the movement of the plate with circulation Γ. Denoting the force as X_b, the variation divided by $2a\rho U$ is plotted as a function of $\tau(= t/2a/U)$.

circulation must be taken into account. From this point of view, there is a room for reconsidering the results.

As seen in **Figure 7**, the force X_b varies with a period $\pi/\nu(= T/2)$ and has a negative value on an average. However, we did not take into account the variation of Γ. The circulation Γ around the plate changes with the same period π/ν. In Eq. (20) we took into account the differentiation of the vitual momentum partly, and it could not give the correct force induced by virtual momentum. The x-component of the real virtual momentum, $\rho\Gamma(t)y_0(t)$, has two time-dependent variables, Γ and y_0. To estimate the correct force X_b, we should take into account the variation of the virtual momentum. The correct expression for the force:

$$X_b = -\frac{\mathrm{d}}{\mathrm{d}t}\big(\rho\Gamma(t)y_0(t)\big). \tag{21}$$

In the present situation, Γ and y_0 are both periodic function of time whose period is $2\pi/\nu(= T)$. The product of two periodic functions with the same period is also a periodic function. The differentiation with respect to t is also a periodic function whose average is zero. Finally, we conclude that the force X_b gives no net force, or $X_{b(av)}=0$. Here the subscript (av) stands for the average over two periods of time, $2T$.

3.2 Effect of moving vortices

In this subsection, we discuss the force resulting from the movement of free vortices. First, we show the result of the force in the y-direction. This problem was first discussed and the solution was analytically given by Kármán-Sears in the linear limit [15]. Their solution corresponds to the sum of the forces Y_v and Y_d. The force Y_v has already been given in Eq.(15) only when one free vortex exists. For the present aim, however, the formula should be extended to include all the vortices. In the following, according to [15] the variation of force divided by $2a\rho U$ is shown.

When W_T=0.5 and ν=0.5 the variations are given in **Figure 8**. The variation of Y_v in the VM, and that of the sum of Y_v and Y_d in the DI. The change of the sum Y_v+Y_d agrees well with the analytical result of [15]. In particular, the agreement becomes better for a lower W_T. It is seen that the two components Y_v and Y_d have an importance of the same degree on the generation of force. At an initial stage, $\tau \approx 0$, the sum has a negative value, and the minimum value of the force occurs at the stage where the velocity in the y-direction becomes maximum, which corresponds to the initial instant $\tau = 0$. The force acts as a drag in this heaving motion. It is interesting to investigate the y-component of the force with respect to the virtual momentum. Because such a force in the y-direction is not related directly to the thrust force, hereafter we will not discuss it further.

At the initial stage, it is seen from **Figures 4** and **5** that vortices of positive vorticity appear. These vortices travel to the position near $x = 40$ at $\tau \approx 20$.

Next we consider the thrust component of the force generated by the change of virtual momentum. From Eq.(15) the force component is expressed for a vortex κ_1 as

$$X_v = 2\pi\rho\kappa_1\dot{y}_1. \tag{22}$$

Taking into account all the vortices existing in the flow field, we can get a complete set of the component for the present problem. The variation is shown in **Figure 9**. It seems to oscillate sinusoidally except for the initial stage and has a positive value in the mean. For this example, the mean value $X_{v(av)}$ is calculated to be 0.148. This means that the force acts in the positive x-direction or the fluid pushes the plate to the direction of the flow. Similarly, the plate is adding the force to the flow as a reaction. In this sense, we may regard the positive $X_{v(av)}$ as a thrust. Whether this force acts as a thrust or a drag depends on the combination of the sign of κ_1 and that of the velocity $\dot{y}_0$. Possible combinations are listed in **Table 1**.

Behind the heaving plate there appear two vortex streets, as shown in **Figures 3** and **4**. The upper street consists of vortices rotating in the positive direction, and the lower one consists of vortices rotating in the negative one. By inspecting the distributions of vortices at two different times $t = 19.8$ and $t = 39.8$, it is found that
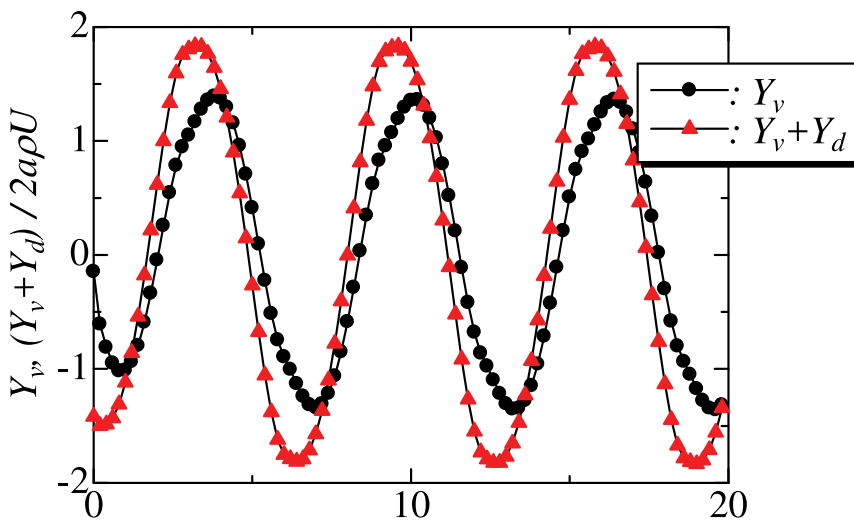
Figure 8.
The variation of the force in the y-direction Y_v due to the change of the virtual momentum. The variation of the sum of Y_v and Y_d of the DI is also plotted.
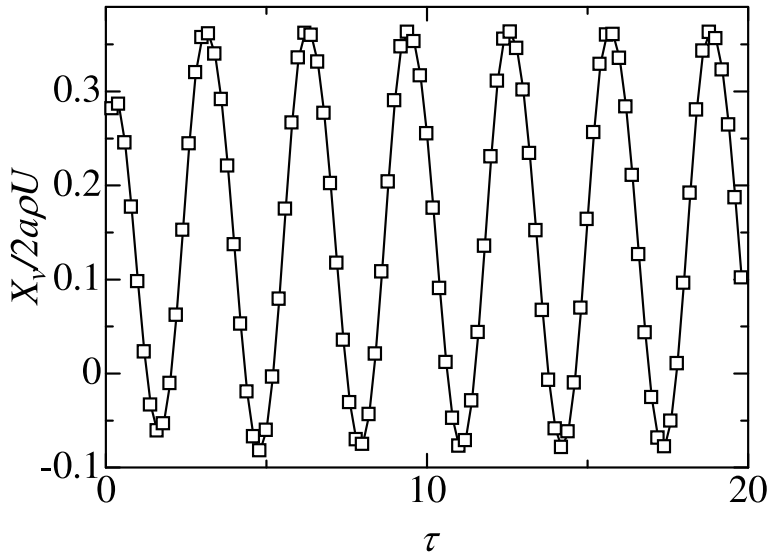
Figure 9.
The force generated from the variation of the virtual momentum is $X_v + \mathrm{i}Y_v$. The variation of the x-component, $X_v/2a\rho U$, is plotted as a function of the dimensionless time τ when $W_T=0.5$ and $\nu=0.5$.

	$\kappa_1{}^a$ (Direction of rotation)	$\dot{y}_1$ (Heaving velocity)	$X_v{}^b$ (Direction of force)	Thrust or drag
I	+	+	+	thrust
II	+	−	−	drag
III	−	+	−	drag
IV	−	−	+	thrust

^{a}*Vorticity.*
^{b}*Force in the x-direction.*

Table 1.
Signs of κ_1, velocity and force. The combination of the sign of κ_1 and $\dot{y}_1$ determine whether X_v acts as a thrust or a drag.

the vortices rotating in the positive direction move upward and those rotating in the negative direction moves downward. This tendency is pronounced for the vortices existing near the trailing edge. It is noted that the force has its peak when the heaving velocity w_h is at the maximum or the minimum. The period of the force oscillation is $T/2$. When the plate passes through $y = 0$, the vortex with a strong intensity is generated. At this instant, the force reaches the maximum.

Table 1 suggests that the sign of the force X_v is positive. In fact, it is seen from **Figure 9** that the average of the force X_v is calculated to be positive.

By comparing **Figures 7** and **9** it is clear that the force component X_v is small compared to X_b. The heaving motion has an influence more effectively on the generation of force in the y-direction As far as the thrust force is concerned, however, the force X_b produced directly by the heaving motion has no effect. Therefore, the force we should take into account is the force X_v only as a thrust.

3.3 Effect of heaving amplitude on the force

It seems that the thrust force is generated due to the motion of the plate against the fluid. To understand the role of the heaving amplitude W_T, we plotted $X_{v(av)}$ as
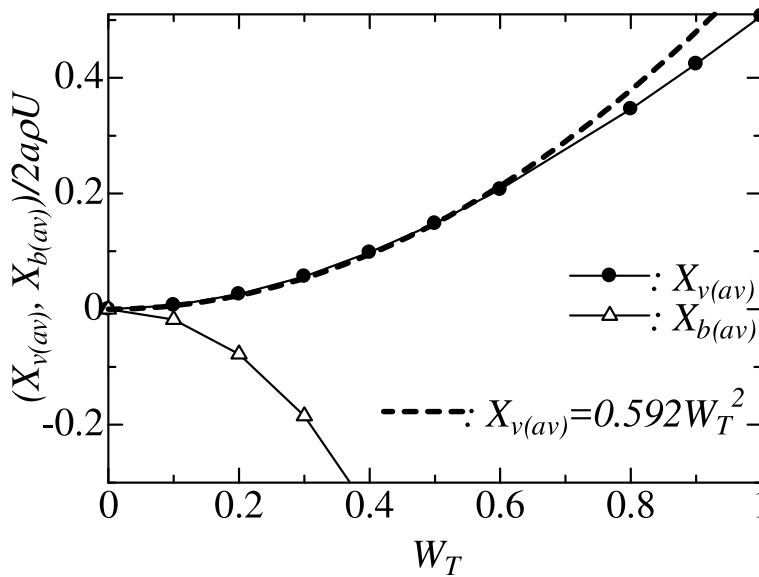
Figure 10.
Thrust variation as a function of W_T when $U=1$ and $\nu=0.5$. Thrust increases proportional to W_T^2.

a function of W_T in **Figure 10**. As mentioned earlier, the subscript (av) means the average over two periods. It is easy to see that the thrust is proportional to W_T^2 except when the W_T value is lage. In this case, the proportional constant is estimated to be 0.592. In addition to $X_{v(av)}$, the variation of $X_{b(av)}$ is also plotted for comparison.

Next, we show the variation of the thrust $X_{v(av)}/2a\rho U$ as a function of U in **Figure 11**. The curve seems to be inversely proportional to U except for large values of U. This means that the thrust X_v does not depend on the velocity U. When $W_T=0.5$, the constant of proportionality is estimated as 0.148.

3.4 Effect of heaving frequency on the force

From the previous subsection, it can be seen that X_v is proportional to W_T^2 and does not depend on U. To confirm it, we have plotted the nondimensional variable $X_{v(av)}/(L/2)/\rho U^2$ as a function of $(W_T/U)^2$ in **Figure 12** for three different W_T's, i.e., 0.3, 0.5 and 0.7. The coefficient $X_{v(av)}/2a\rho U^2$ is called the thrust coefficient denoted as C_L. The coefficient has almost linear relation to the velocity ratio W_T/U. The constant of proportionality must be nondimensional. In such unsteady locomotions, the most important dimensionless parameter is the reduced frequency $k(=2a\rho\nu/U)$ or the Froude number. However, **Figure 12** gives no defined dependence of the reduced frequency on the coefficient C_T. The plotted data include various values of k between $0.2 \leq k \leq 2.5$. We can draw our conclusion that the reduced frequency k does not affect the thrust coefficient in this heaving motion.
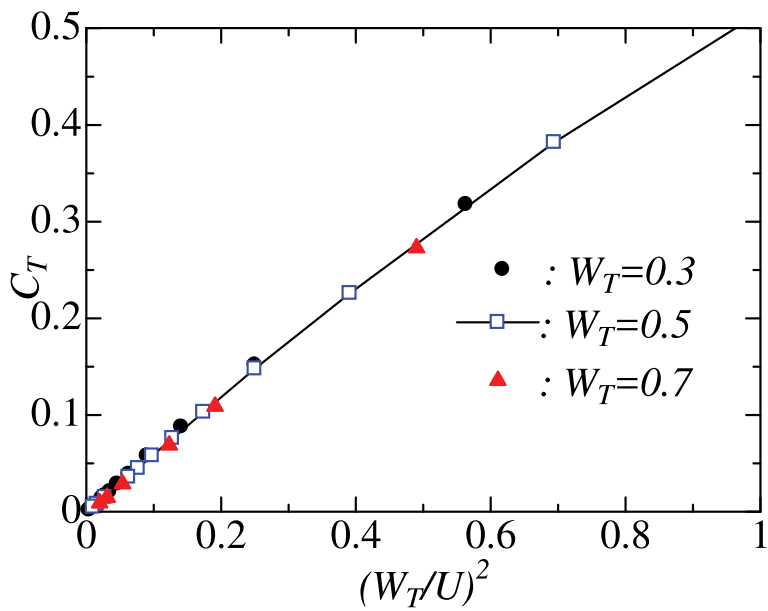
We summarise the thrust coefficient in the nondimensional form,

$$C_T = \frac{X_{v(av)}}{L\frac{1}{2}\rho \mathcal{U}^2} \propto \left(\frac{W_T}{\mathcal{U}}\right)^2, \tag{23}$$

where L is the chord length being equal to $4a$.
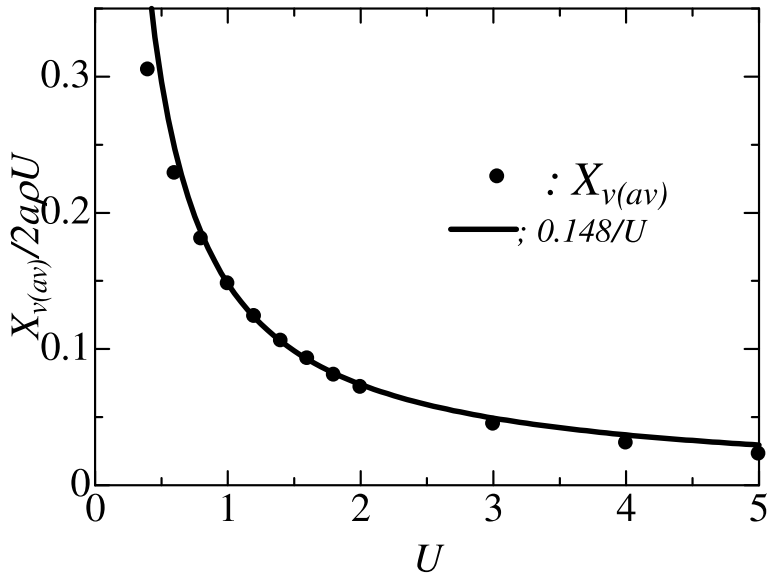
Figure 11.
Thrust variation as a function of U for $W_T = 0.5$. The thrust is inversely proportional to U. The proportional constant is estimated as 0.148.

Figure 12.
Thrust coefficient C_T as a function of $(W_T/U)^2$. For three different W_T the data are almost decomposed into a unique line.

4. Concluding remarks

Thrust force can be generated by a simple heaving motion of a plate. The force is perpendicular to the direction of oscillation. A pair of rows of vortices plays an important role in the generation of the force. The two vortex streets give rise to an increase in momentum in the direction normal to the direction of oscillation. The

word "momentum" here does not mean the usual momentum but the virtual one, because the usual momentum cannot be determined in such a vortex system. The direct integration of the pressure around the surface of a body is not a correct way to know the thrust generation. Application of the virtual momentum to the generation of force made the estimation of the force possible.

In general, the most important parameter characterising the unsteady flow is the reduced frequency k or Froude number. How the parameter plays a part in the generation of force has been a main concern of many people. Many researchers have tried to address this problem experimentally. However, the task was difficult to address, and only few researchers have answered analytically.

Our result is for the coefficient of thrust C_T,

$$C_T \propto \left(\frac{W_T}{U}\right)^2. \tag{24}$$

The proportional constant is nondimensional and does not depend on the parameter k expressing the unsteadiness of flow. The thrust force $X_{v(av)}$ is independent of uniform velocity U, and therefore the coefficient C_T is proportional to $(W_T/U)^2$.

Although our analysis is confined to the heaving motion of a thin plate, we summarise that the force due to the vortex movement can be expressed as a function of nondimensional quantity in a simple form. It is expected that our analysis could apply to more complex movement of an aerofoil.

Acknowledgements

Conflict of interest

The author declares no conflict of interest.

Nomenclature

a	Radius of circle in mapped plane
C_T	Thrust coefficient
$k\ (=2a\rho\nu/U)$	Reduced frequency
L	Chord length ($=4a$)
$T = 2\pi/\nu$	Period of oscillation
U	Uniform velocity
W_T	Amplitude of heaving velocity
$X + iY$	Complex force
$x + iy$	Coordinates in complex plane
$w = u - iv$	Complex velocity
ν	Radian frequency of heaving
Γ	Circulation along the curve in the anticlockwise direction
κ	Vorticity (positive for clockwise, negative for anticlockwise)
ρ	Density of fluid
ζ	Plane mapped from real z-plane
VM	Virtual momentum component
DI	Direct interaction component

Subscript

v   Virtual component
d   Direct interaction component
b   Bound vortex
av.   Average

Abbreviations

LEV   Leading edge vortex

Author details

Kazuo Matsuuchi
University of Tsukuba, Tsukuba City, Japan

*Address all correspondence to: matsuuch@kz.tsukuba.ac.jp

IntechOpen

References

[1] Dickinson, M.. Solving the mystery of insects use a combination of aerodynamic effects to remain aloft. *Scientific American* June, 2001:35–41.

[2] Trianthafyllou, M.S. & Trianthafyllou, G.S.. An efficient swimming machine. *Scientific American* March, 1995:64–70.

[3] Lamb, H.. *Hydrodynamics*, sixth edn. 1932; Cambrige Univ.

[4] Trianthafyllou, M.S., Trianthafyllou, G.S. & Gopalkrishnab, R.. Wake mechanics for thrust generation in oscillating foils. Phys. Fluids A 1991: **3**:2835–2837.

[5] Trianthafyllou, M.S., Techet, A.H. & Hover, F.S.. Review of experimental work in biomemetic foils. IEEE Journal of Ocean Engineering 2004: **29**:585–594.

[6] von Loebbecke, A., Mittal, R., Fish, F. E. & Mark, R.. A comparison of the kinematics of the dolphin kick in humans and cetaceans. Human Movement Science 2009: **28**:99–112.

[7] Alben, S.. Simulating the dynamics of flexible bodies and vortex streets. J. Comp. Phys. 2009: **228**:2587–2603.

[8] Imai, I.. *Fluid Dynamics* [in Japanese], 1st edn. 1973; Shokabo.

[9] Milne-Thomson, L. M.. *Theoretical Hydrodynmics*, 5th edn. 1968; Dover Pub.

[10] Batchelor, G. K.. *An Introduction to Fluid Dynamics*, 1st edn. 1967; Cambrige Univ.

[11] Munk, M. M.. Fluid mechanics, part II. In *Aerodynamic Theory,* vol. I (ed. W. F. Durand), pp. 224–259. 1976; Peter Smith Pub.

[12] Saffman, P. G.. *Vortex Dynamics*, 1st edn. 1995; Cambrige Univ.

[13] Minotti, F. O.. Unsteady two-dimensional theory of a flapping wing. *Physical Review E* 2002: **66** (051907).

[14] Anderson, J. M., Streitlien, K., Barret, D. S. & Triantafyllou, M. S.. Oscillating foils of high propulsive efficiency. J. Fluid Mech. 1998: **360**: 41–72.

[15] von Kármán, Th. & Sears, W. R. M.. Airfoil theory for non-uniform motion. J. Aero. Sciences 1938: **5–10**:379–390.

Edited by Kazuo Matsuuchi
and Hiroaki Hasegawa

Almost all animals move around frequently in space. Their aim is to walk and fly in search of food or to propagate their species. Thus, changing positions is important for creatures' survival and maintaining the environment. As such, this book examines movement with a focus on force and propulsion. Chapters cover topics including rocket engines, electric propulsion, mechanisms of force, and more.

IntechOpen